HZDR-093

OPTIMAL BEAM LOADING IN A NANOCOULOMB-CLASS LASER WAKEFIELD ACCELERATOR

Jurjen Pieter Couperus

Wissenschaftlich-Technische Berichte
HZDR-093 · ISSN 2191-8708

WISSENSCHAFTLICH-
TECHNISCHE BERICHTE

HZDR
HELMHOLTZ
ZENTRUM DRESDEN
ROSSENDORF

Wissenschaftlich-Technische Berichte
HZDR-093

Jurjen Pieter Couperus

OPTIMAL BEAM LOADING IN A NANOCOULOMB-CLASS LASER WAKEFIELD ACCELERATOR

HZDR

HELMHOLTZ
ZENTRUM DRESDEN
ROSSENDORF

Druckausgabe: ISSN 2191-8708

Elektronische Ausgabe: ISSN 2191-8716

https://www.hzdr.de/publications/Publ-28080

urn:nbn:de:bsz:d120-qucosa2-319537

DOI: 10.5281/zenodo.1463710 (Dissertation)

Die vorliegende Arbeit wurde sowohl als Dissertation an der Fakultät Mathematik und Naturwissenschaften der Technischen Universität Dresden sowie als Wissenschaftlich-Technischer Bericht des Helmholtz-Zentrum Dresden – Rossendorf mit der Berichtsnummer **HZDR-093** veröffentlicht.

2018

Herausgegeben vom

Helmholtz-Zentrum Dresden - Rossendorf

Bautzner Landstraße 400

01328 Dresden

Germany

TECHNISCHE UNIVERSITÄT DRESDEN

HZDR
HELMHOLTZ ZENTRUM DRESDEN ROSSENDORF

Faculty of Science
Department of Physics

Institute for Radiation Physics
Laser Particle Acceleration Division

OPTIMAL BEAM LOADING IN A NANOCOULOMB-CLASS LASER WAKEFIELD ACCELERATOR

Jurjen Pieter Couperus, MSc
Born on: 8th September 1985 in Smallingerland

DISSERTATION

to achieve the academic degree

DOCTOR RERUM NATURALIUM (DR. RER. NAT.)

Supervisor
Dr. Arie Irman

Assessors
Prof. Dr. Ulrich Schramm
Prof. Dr. Klaus-J. Boller
Prof. Dr. Thomas E. Cowan

DRESDEN concept
Exzellenz aus Wissenschaft und Kultur

Submitted:
8th March 2018
Public defence:
7th September 2018

Version 1.01
13th September 2018
DOI: 10.5281/zenodo.1463710

ABSTRACT

Laser plasma wakefield accelerators have seen tremendous progress in the last years, now capable of producing electron beams in the GeV energy range. The inherent few-femtoseconds short bunch duration of these accelerators leads to ultra-high peak-currents. Reducing the energy spread found in these accelerators, while scaling their output to hundreds of kiloampere peak current would stimulate the next generation of radiation sources covering high-field THz, high-brightness X-ray and γ-ray sources, compact free-electron lasers and laboratory-size beam-driven plasma accelerators. At such high currents, an accelerator operates in the beam loaded regime where the accelerating field is strongly modified by the self-fields of the injected bunch, potentially deteriorating key beam parameters. However, if appropriately controlled, the beam loading effect can be employed to improve the accelerator's performance, specifically to reduce the energy spread.

In this thesis the beam-loading effect is systematically studied at a quasi-monoenergetic nanocoulomb-class laser wakefield accelerator. For this purpose, a tailored scheme of the self-truncated ionisation injection process is introduced for the non-linear bubble regime. This scheme facilitates stable and tunable injection of high-charge electron bunches within a short and limited time-frame, ensuring low energy spread right after injection. Employing a three millimetres gas-jet acceleration medium and a moderate 150 TW short pulse laser system as driver, unprecedented charges of up to 0.5 nC within a quasi-monoenergetic peak and energies of $\sim$0.5 GeV are achieved. Studying the beam loading mechanism, it is demonstrated that at the optimal loading condition, i.e. at a specific amount of injected charge, performance of the accelerator is optimised with a minimisation of the energy spread. At a relative energy spread of only 15%, the associated peak current is around 10 kA, while scaling this scheme to operate with a petawatt driver laser promises peak-currents up to 100 kA.

Dedicated in loving memory
to my parents.

PUBLICATIONS BY THE AUTHOR

- A. Irman, J.P. Couperus, A. Debus, A. Köhler, J.M. Krämer, R. Pausch, O. Zarini & U. Schramm.

  "Improved performance of laser wakefield acceleration by tailored self-truncated ionization injection". In: *Plasma Physics and Controlled Fusion*, 60, 044015 (2018).

  DOI: 10.1088/1361-6587/aaaef1

  In this work referenced to as:[1]

- J.M. Krämer, A. Jochmann, M. Budde, M. Bussmann, J.P. Couperus, T.E. Cowan, A. Debus, A. Köhler, M. Kuntzsch, A. Laso Garcia, U. Lehnert, P. Michel, R. Pausch, O. Zarini, U. Schramm & A. Irman.

  "Making spectral shape measurements in inverse Compton scattering a tool for advanced diagnostic applications". In: *Scientific Reports*, 8, 1 (2018).

  DOI: 10.1038/s41598-018-19546-0

  In this work referenced to as:[2]

- J.P. Couperus, R. Pausch, A. Köhler, O. Zarini, J.M. Krämer, M. Garten, A. Huebl, R. Gebhardt, U. Helbig, S. Bock, K. Zeil, A. Debus, M. Bussmann, U. Schramm & A. Irman.

  "Demonstration of a beam loaded nanocoulomb-class laser wakefield accelerator". In: *Nature Communications*, 8, 487 (2017).

  DOI: 10.1038/s41467-017-00592-7

  In this work referenced to as:[3]

- U. Schramm, M. Bussmann, A. Irman, M. Siebold, K. Zeil, D. Albach, C. Bernert, S. Bock, F. Brack, J. Branco, J.P. Couperus, T.E. Cowan, A. Debus, C. Eisenmann, M. Garten, R. Gebhardt, S. Grams, U. Helbig, A. Huebl, T. Kluge, A. Köhler, J.M. Krämer, S. Kraft, F. Kroll, M. Kuntzsch, U. Lehnert, M. Loeser, J. Metzkes, P. Michel, L. Obst, R. Pausch, M. Rehwald, R. Sauerbrey, H.P. Schlenvoigt, K. Steiniger & O. Zarini.

  "First results with the novel petawatt laser acceleration facility in Dresden." In: *Journal of Physics: Conference Series*, 874, 12028 (2017).

  DOI: 10.1088/1742-6596/874/1/012028

  In this work referenced to as:[4]

- T. Heinemann, B. Hidding, R.W. Assmann, A. Martinez de la Ossa, A. Knetsch, O. Kononenko, J.P. Couperus, A. Irman, A. Köhler, T. Kurz, U. Schramm & O. Zarini.

  "Investigating the Key Parameters of a Staged Laser- and Particle Driven Plasma Wakefield Accelerator Experiment." In: *Proceedings of International Particle Accelerator Conference (IPAC'17)*, TUPIK010, 1703–1706 (2017).

  DOI: 10.18429/JACoW-IPAC2017-TUPIK010

  In this work referenced to as:[5]

- J.P. Couperus, A. Köhler, T.A.W. Wolterink, A. Jochmann, O. Zarini, H.M.J. Bastiaens, K.J. Boller, A. Irman & U. Schramm.

  "Tomographic characterisation of gas-jet targets for laser wakefield acceleration." In: *Nuclear Instruments and Methods in Physics Research Section A: Accelerators, Spectrometers, Detectors and Associated Equipment*, 830, 504–509 (2016).

  DOI: 10.1016/j.nima.2016.02.099

  In this work referenced to as:[6]

- A. Köhler, J.P. Couperus, O. Zarini, A. Jochmann, A. Irman, & U. Schramm.

  "Single-shot betatron source size measurement from a laser-wakefield accelerator." In: *Nuclear Instruments and Methods in Physics Research Section A: Accelerators, Spectrometers, Detectors and Associated Equipment*, 829, 265–269 (2016).

  DOI: 10.1016/j.nima.2016.02.031

  In this work referenced to as:[7]

- J.M. Krämer, J.P. Couperus, A. Irman, A. Köhler, M. Kuntzsch, U. Lehnert, P. Michel, U. Schramm & O.Zarini.

  "Bunch Arrival-Time Monitoring for Laser Particle Accelerators and Thomson Scattering X-Ray Sources." In: *Proceedings of the 5th International Beam Instrumentation Conference (IBIC2016)*, TUPG53, 468–470 (2016).

  DOI: 10.18429/JACoW-IBIC2016-TUPG53

- U. Schramm, M. Bussmann, J.P. Couperus, T. Cowan, A.D. Debus, A., Irman, A. Jochmann, R. Pausch, R. Sauerbrey & K. Steiniger.

  "Bright X-ray Pulse Generation by Laser Thomson-Backscattering and Traveling Wave Optical Undulators." In: *Frontiers in Optics 2014*, FTu4G.2 (2014).

  DOI: 10.1364/FIO.2014.FTu4G.2

  In this work referenced to as:[8]

- R. Pausch, H. Burau, M. Bussmann, J.P. Couperus, T. Cowan, A. Debus, A. Huebl, A. Irman, A. Köhler, U. Schramm, K. Steiniger & R. Widera.

  "Computing angularly-resolved far-field emission spectra in particle-in-cell codes using GPUs." In: *Proceedings of the 5th International Particle Accelerator Conference (IPAC 2014)*, MOPRI069 (2014).

- A. Jochmann, A. Irman, M. Bussmann, J. P. Couperus, T. E. Cowan, A. D. Debus, M. Kuntzsch, K. W. D. Ledingham, U. Lehnert, R. Sauerbrey, H. P. Schlenvoigt, D. Seipt, Th. Stöhlker, D. B. Thorn, S. Trotsenko, A. Wagner & U. Schramm.

  "High Resolution Energy-Angle Correlation Measurement of Hard X Rays from Laser-Thomson Backscattering." In: *Physical Review Letters*, 111, 114803 (2013).

  DOI: 10.1103/PhysRevLett.111.114803

  In this work referenced to as:[9]

- A. Jochmann, A. Irman, U. Lehnert, J.P. Couperus, M. Kuntzsch, S. Trotsenko, A. Wagner, A.D. Debus, H.P. Schlenvoigt, U.Helbig, S.Bock, K.W.D. Ledingham, T.E. Cowan, R. Sauerbrey & U. Schramm.

  "Operation of a picosecond narrow-bandwidth Laser–Thomson-backscattering X-ray source." In: *Nuclear Instruments and Methods in Physics Research Section B: Beam Interactions with Materials and Atoms*, 309, 214–217 (2013).

  In this work referenced to as:[10]

  DOI: 10.1016/j.nimb.2013.01.065

- T. Kurz, J.P. Couperus, J.M. Krämer, H. Ding, S. Kuschel, A. Köhler, O. Zarini, D. Hollatz, D. Schinkel, R. D´Arcy, J.P. Schwinkendorf, J. Osterhoff, A. Irman, U. Schramm & S. Karsch.

  "Calibration and cross-laboratory implementation of scintillating screens for electron bunch charge determination." *Review of scientific instruments*, in press (2018).

  In this work referenced to as:[11]

  DOI: 10.1063/1.5041755

NOTE

Some of the work presented in this thesis has been previously published in above-mentioned publications. As such, some overlap exists.
Specifically: Part of the work on operation of a nanocoulomb-class LPA discussed in chapter 4 and on the beam loading study treated in chapter 5 has been published in ref.[3] and ref.[1]. Some specifics on the electron spectrometer design and accuracy discussed in section 3.5 and some results of the nanocoulomb-class LPA have been published in ref.[4]. A large part of the work on gas target characterisation in section 3.4 has been published in ref.[6]. Part of the work on scintillating screen calibration presented in section 3.5.5 will also be published in ref.[11].

CONTENTS

1. MOTIVATION & INTRODUCTION

Particle accelerators are one of the most important tools in modern society with applications in many fields, among them medicine, industry, security and fundamental research. Although the first particle accelerator was demonstrated not even a hundred years ago in the early 1930's by Cockcroft and Walton[12], since then they have been rapidly developed to the point that they are now widespread and routinely operated machines. Worldwide there are tens of thousands accelerators of varying size, from small metre-scale accelerators for electron beam material irradiation to the largest and most well-known accelerator the Large Hadron Collider (LHC) at CERN, which does not only impress with its ability to accelerate particle beams up to energies of 6.5 TeV, but also by its sheer size with a 27 km circumference.

And although accelerator technology has seen tremendous and still ongoing development, conventional accelerators are reaching their fundamental limit. At the vacuum breakdown limit, local fields reach strengths such that solid surface electrons are emitted into the vacuum. A cascade of effects results in the collapse of the accelerating field, effectively restricting accelerating gradients to about 100 MV/m[13,14]. Therefore increasing the maximum beam energy can only be achieved by up-sizing current technology. In effect, machines that are aiming at breaching new scientific frontiers by reaching previously inaccessible regimes tend to grow larger and more expensive to build and to operate. The LHC mentioned above is one example, which is an accelerator unique in its kind. Another example are modern light-source synchrotrons, which enable us to study processes occurring on the nanometre scale. More widespread with several dozens of such machines worldwide, they are typically still several hundred metres in diameter.

X-ray Free Electron Lasers (XFELs) are the newest generation of light sources, which are able to generate high-brightness ultra-short X-ray pulses enabling cutting-edge research in material science, biology and chemistry on femtosecond-timescale processes which cannot be resolved by synchrotrons. These machines use a conventional accelerator to create high energy electron beams followed by a long magnetic undulator. For example, the European XFEL accelerates electrons up to 17.5 GeV over a length of 1.7 kilometres followed by undulators over a length of up to 175 metres, creating X-ray bunches with a wavelength of only 0.05 to 4.7 nm and sub-100 fs pulse duration. But, with its total length of 3.4 kilometres, a construction cost of 1.22 billion euros and

an annual estimated budget of 117 million euros, machines of this kind can only be constructed and operated by large consortia or by large countries. There are only few of such facilities worldwide, besides European XFEL in Germany: SACLA in Japan, LCLS in the USA, PAL-XFEL in Korea and SwissFEL in Switzerland.

With high demand, the limited number of synchrotrons and XFELs effectively limits accessibility to these bright (short-pulse) x-ray sources. In highly competitive programs, only part of research and industry proposals attain access, with the largest part of proposed research not investigated.

There is a large need for the implementation of a new particle acceleration technique which is not limited by the fundamental vacuum breakdown limit.

Such an alternative is required for the next generation accelerator to reach record beam energies for fundamental research, currently held by the LHC at 6.5 TeV. Reaching even higher energies with conventional accelerators is technically possible, but this option exceeds the financial support limit of society.

Downsizing current accelerator based light-sources, reducing construction and running costs, would highly improve accessibility. Potentially this can open the possibility of cutting edge research which can now only be performed at a handful of facilities worldwide, to be implemented even at company research departments or at the university research level.

1.1. PLASMA BASED ACCELERATION

Plasma based acceleration is a technique able to reach extremely high accelerating gradients, not limited by the vacuum breakdown limit, which has the potential to complement conventional acceleration techniques where down-sizing is required. This relatively young field of research, introduced in 1979 by Tajima and Dawson[15], is based on harvesting high accelerating field gradients induced by collective plasma oscillations. These oscillations, occurring on the few-tens of micrometres scale, are created by propagating either a laser or high charge particle beam through an optically transparent plasma.

For the laser driven case, know as laser wakefield acceleration (LWFA), an intense laser driver propagates through the plasma, expelling electrons from its path by ponderomotive force. This creates a positive net charge region located directly behind the laser pulse. The charge separation induces strong Coulomb forces and after the laser has passed, in an effort to restore the charge balance, expelled electrons return to the laser's pathway on the time-scale of the plasma frequency. Overshooting their equilibrium position a plasma wakefield is formed behind the laser pulse, much like a boat creates a wakefield in water. These plasma wakefields can act as accelerating cavities, co-propagating with the laser at near to speed of light velocity, capable to accelerate charged particles.

This mechanism could not be studied until the introduction of the chirped pulse amplification (CPA) technique[16,17] in the mid- to late-80's. CPA pushed laser technology to the multi-terawatt peak power, powerful enough to drive plasma wakefields. The first demonstration of laser electron acceleration up to a few tens of MeVs followed shortly after with beat wave acceleration in 1993 by Clayton et al.[18,19] and with LWFA in 1994

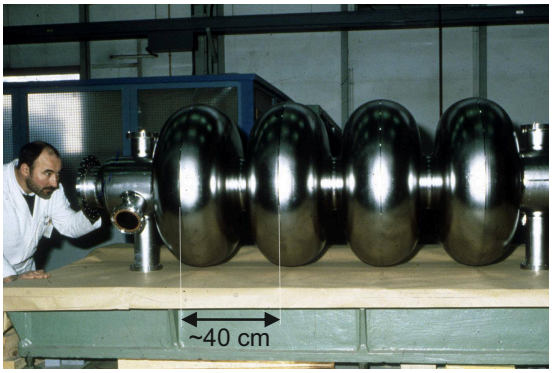

(a) Conventional rf cavity

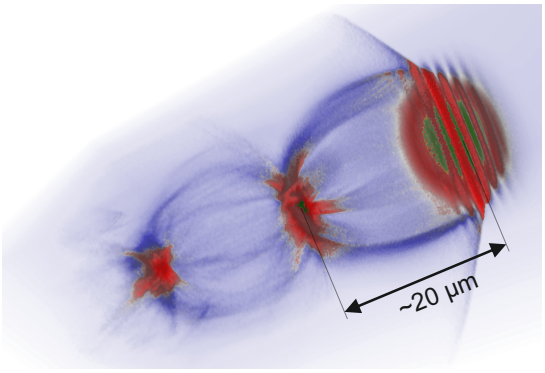

(b) Laser driven plasma cavity, PIConGPU render

Figure 1.1.: **Comparison between a conventional accelerator and a laser wakefield accelerator.** *(a)* shows a conventional superconducting radio-frequency cavity (Image: CERN). The cavity size of conventional accelerators is macroscopic and accelerating gradients are limited to below 100 MV/m. *(b)* shows a laser driven accelerator cavity in a underdense plasma. The cavity is co-propagating with the laser driver (towards the right) and is microscopic in size, supporting accelerating gradients of over 100 GV/m.

by Nakajima at al.[20].

After its first demonstration the field developed quickly[21], with the largest step being reached with access to the bubble (or blowout) regime. This highly non-linear regime was identified in 2002 by Pukhov and Meyer-ter-Vehn[22]. It requires all electrons to be completely expelled from the laser path, leaving behind an ion cavity region surrounded by a high density sheath of electrons forming a bubble shaped wakefield. The first demonstrations of this scheme was reported in a collection of three papers published in a 2004 Nature issue[23–25], appearing on the cover page as the *'Dream beam'*. At this point the potential of this scheme was demonstrated, for the first time producing high energy and quasi-monoenergetic electron bunches produced in only a fraction of acceleration length as is otherwhise needed in conventional accelerators. Nowadays most laser wakefield accelerators operate in the bubble regime and energies of over 4 GeV have been reached within a sub-decimetre acceleration length[26–28].

These high energies attained over such a short acceleration distance can be reached due to the enormous fields that can be sustained in these bubble-shaped cavities, easily reaching accelerating gradients of several hundreds GV/m. A visual comparison to conventional accelerators as shown in figure 1.1 illustrates the difference between both schemes very clearly. Conventional accelerators generally have macroscopic cavities of up to several decimetres in length, while a laser plasma accelerator (LPA) cavities are scaled down by roughly four orders of magnitude to a few tens of micrometres, while the sustainable electric field increases by three to four orders of magnitude.

Until recently, the main focus in laser wakefield acceleration has been on increasing the attainable energy. This is a natural step, exploiting the high accelerating gradient of this scheme, but also offers grand challenges. When collider relevant energies are to be reached, the dephasing limitation has to be overcome. The fact that a laser pulse in a medium propagates slightly below the speed of light, causes a relativistic particle bunch to eventually dephase out of the accelerating field. To defeat this limit, one either

has to rely on staging[29,30], a traveling-wave focussing geometry[31] or on particle beam driven schemes[32–34], which do not know this limitation.

Meanwhile, there are many applications in closer reach where laser plasma accelerators can be ideal drivers, focussing not only on their high acceleration gradient, but exploiting the inherent short bunches produced by these accelerators. The bunches injected in the microscopic cavities are generally in the order of only a few femtoseconds of duration[35,36] while the bubble shaped cavities allows for acceleration of large quantities of charge[37,38]. In effect, Laser plasma accelerators (LPAs) can achieve impressive peak currents. Where conventional accelerators can produce only a few-kiloampere peak current, LPAs have now been demonstrated to produces a few tens of kiloampere[3,36,39] with the possibility to scale to even higher currents. These high peak-currents make laser plasma accelerators ideal drivers for the next-generation compact light sources covering high-field THz[40,41], high-brightness X-ray[9,42] and γ-ray[43,44] sources, compact FELs[45–49] and laboratory-size beam-driven plasma accelerators[5,50,51].

However, accelerators that are generating such high currents are subject to the beam loading effect. This effect, where the injected bunch self-field superimposes on the accelerator cavity field, causes a local deformation of the accelerating field. This effect becomes stronger with higher bunch charge and can potentially deteriorate key beam parameters if not properly controlled. The main challenge in plasma based acceleration is to properly handle an accelerator such that the charge output can be increased without degrading the beam quality.

This thesis reports on the ongoing efforts to improve charge output, and thus peak current, and beam quality at the Helmholtz-Zentrum Dresden-Rossendorf. The commissioning of a new LWFA experimental area following a facility upgrade and the first experiments after this upgrade are presented in this thesis. A new approach of operation in the bubble regime is introduced which is able to inject an unprecedented amount of charge into the wakefield with a quasi-monoenergetic energy distribution. The amount of injected charge can be precisely controlled and charges of over 500 pC have been injected, reaching peak currents of up to 20 kA. The accelerator stability and the controllability achieved in this work enabled to gain further insight into the accelerator dynamics and allowed for a systematic study of the beam loading effect. Following original predictions[52–54], the work in this thesis shows how this effect influences the energy spread. It is demonstrated that in order to minimise energy spread, a specific amount of charge has to be loaded into the wakefield, the so-called optimal loading condition. The energy spread being a vital beam property, how to minimise this is an important finding. Any under-dense plasma based accelerator, be it laser- or beam-driven, should be operated taking beam loading into account.

1.2. THESIS OUTLINE

The topics covered in this thesis have been divided into several chapters, guiding the reader step-by-step or enabling to study specific topics individually.

First, chapter 2 offers the theoretical background required to understand the operation of a LPA in the nonlinear bubble regime, the principles of beam loading and how beam loading can be employed to improve beam quality.

Chapter 3 covers the accelerator setup and all relevant technical details involved. The infrastructure required to operate the LPA, covering the experimental area and the short-pulse high intensity DRACO laser system, is treated here. The target providing the accelerator medium is discussed in detail in this chapter, as is the spectrometer which was developed for charge and energy diagnosis. Any theoretical background required for these topics is given directly where appropriate.

The main topics of this thesis, operation of the LPA and the beam loading effect, are subsequently divided in two separate chapters.

Performance of the accelerator is presented in chapter 4, detailing operation in a tailored self-truncated ionisation injection scheme. This chapter covers how stable operation of the accelerator is reached such that high-charge quasi-monoenergetic beams can be routinely produced. This chapter also gives a detailed insight into the accelerator dynamics using particle-in-cell simulations.

A systematic study of the beam loading effect is presented in chapter 5. Here it is shown how the amount of charge injected into the accelerator can be precisely tuned, enabling this study. The work in this chapter verifies theory previously developed by Tzoufras et al.[54,55] and shows that in order to generate high charge beams with a small energy spread, laser-plasma accelerators have to be operated at the optimal loading condition.

Finally, chapter 6 concludes this work, giving an outlook of the field and introducing some first steps on application of the LPA as a secondary wakefield driver.

On the difference between LPA & LWFA:

The use of these two abbreviation can be confusing as they are closely related to each-other, yet subtlety different. Laser Plasma Accelerator (LPA) refers to an accelerator, while Laser Wakefield Acceleration (LWFA) refers to the specific underlying acceleration mechanism on which the accelerator presented in this thesis is based. The term LPA can also refer to different types of accelerators which rely on a different laser-plasma interaction mechanisms and is not limited to electron accelerators only.

In this thesis LPA is used to abbreviate Laser Plasma Accelerator, always referring to an accelerator based on the Laser Wakefield Acceleration (LWFA) mechanism.

2. THEORY

This chapter gives the theoretical background on laser wakefield acceleration in the bubble regime and the self-truncated ionisation injection (STII) method. Goal is to present the reader a comprehensive overview of the knowledge required to understand results presented in this thesis. Specifically on driving a nanocoulomb-class LPA with the STII method in chapter 4 and on subsequent energy spread minimisation by utilising the beam loaded effect presented in chapter 5. As such, this chapter does not cover the entire field of LWFA, which would be to extensive to detail here. Neither is every aspect explained starting at the basics. Instead, references which offer a more in-depth treatment of the matter are given at points where new aspects or formulas are introduced.

Section 2.1 briefly describes the ionisation mechanism of electrons from their parent atoms, which stands at the basis of LWFA. This mechanism does not only enable the formation of the accelerator's medium, it also plays a crucial role in ionisation injection schemes. Next, in section 2.2, the principles of electron motion in the presence of electromagnetic fields is discussed. In the presence of a high-intensity laser pulse electron motion is responsible for the formation of a self-guiding plasma channel, enabling the accelerator to operate over many times the Rayleigh length, which is detailled in section 2.3. The motion of electrons also stand at the basis of plasma wakefield formation and acceleration, which principles are introduced in section 2.4. Section 2.5 specifically treats the non-linear bubble regime in which the accelerator is operated. Section 2.6 gives an overview of available injection mechanisms for LPA, with subsection 2.6.1 focussed on the ionisation injection mechanism. Finally, the principles and theory of beam loading is given in section 2.7.

2.1. IONISATION

The plasma medium in which LWFA takes place is created by the ionisation of a gas medium. As will be discussed in section 3.4, the main target providers in LWFA are discharge capillaries, gas cells and gas-jets. Apart from discharge capillaries, where the gas is ionised by a high-voltage discharge prior to the arrival of the laser pulse, an indirect method is used where a gas-jet or cell creates a well-defined gas medium which is subsequently ionised by the field of a high intensity laser pulse to create the accelerator

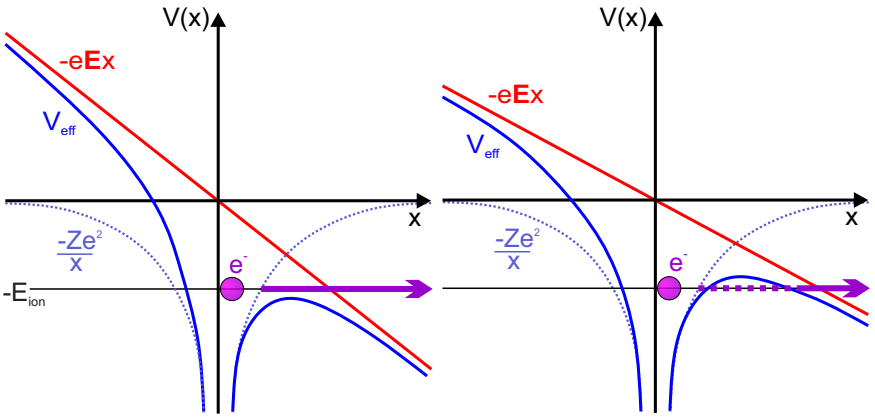

(a) Barrier suppression ionisation (b) Tunnel ionisation

Figure 2.1.: **Ionisation mechanisms.** An external field (red line) suppresses the atomic Coulomb field (blue line, the unsuppressed coulomb field is shown by the dotted line), freeing the electron. *(a)* shows barrier suppression ionisation, where the external field is strong enough to completely suppress the barrier. *(b)* shows tunnel ionisation where the external field is not strong enough to completely suppress the barrier, but where the electron has a non-zero probability to be freed from its bound state by tunnelling through the reduced barrier.

plasma medium. The ionising laser pulse can either be a dedicated laser pulse or the same laser pulse that drives the acceleration mechanism itself.

Two ionisation processes can play a role, Barrier Suppression Ionization (BSI) and Tunnelling Ionization (TI). Both processes depend on an external electric field, e.g. the laser electric field, being strong enough to distort the atomic Coulomb potential according to[56]

$$V_{\text{eff}}(x) = -\frac{Ze^2}{x} - eEx, \tag{2.1}$$

The right term represents a suppression of the potential by the external (laser) electric field E. Z is the charge state of the atom or ion.

In the case of BSI the distortion caused by the laser electric field is large enough to completely suppress the Coulomb potential below the electron binding potential, as illustrated in figure 2.1(a), freeing the electron with a probability of one. In order to suppress the atom's Coulomb field far enough to reach BSI a sufficiently strong field is required. The laser intensity to reach this threshold is given by[56]

$$I_{\text{BSI}}\left[\frac{\text{W}}{\text{cm}^2}\right] = 4.00 \times 10^9 \frac{E_{\text{ion}}^4[\text{eV}]}{Z^2}, \tag{2.2}$$

where E_{ion} is the ionisation energy characteristic for a bound electron.

The required energy to remove electrons differs per atom and electrons closer to the nucleus, i.e. in a lower shell, generally require more energy to be removed. Table 2.1 shows the ionisation energies for several ions relevant for LWFA together with the I_{BSI} according to equation (2.2). Once this threshold is reached for all bound electrons of a specific gas, complete ionisation occurs. An atom becomes only partially ionised if I_{BSI} is sufficiently high to free outer electrons, but not high enough to free electrons that are bound stronger to the nucleus.

Table 2.1.: **Ionisation energy** (values from ref.[57]) with corresponding intensity according to equation (2.2) required to reach barrier suppression ionization. a_0 is the corresponding normalised laser potential according to equation (2.8) for a central laser wavelength of 800 nm.

Ion	E_{ion} [eV]	I_{BSI} [W cm^{-2}]	a_0 λ_0 = 800 nm
H^{1+}	13.60	1.37×10^{14}	8.0×10^{-3}
He^{1+}	24.59	1.42×10^{15}	2.6×10^{-2}
He^{2+}	54.42	8.77×10^{15}	6.4×10^{-2}
N^{1+}	14.53	1.78×10^{14}	9.2×10^{-3}
N^{2+}	29.60	7.68×10^{14}	1.9×10^{-2}
N^{3+}	47.45	2.25×10^{15}	3.3×10^{-2}
N^{4+}	77.47	9.00×10^{15}	6.5×10^{-2}
N^{5+}	97.89	1.47×10^{16}	8.3×10^{-2}
N^{6+}	552.1	1.03×10^{19}	2.21
N^{7+}	667.0	1.61×10^{19}	2.77

The BSI process described above gives an ionisation probability of one once the threshold is reached. However, before this threshold is reached tunnel ionisation (TI) can already occur. This is a quantum mechanical phenomenon in which, even when the Coulomb field is not sufficiently suppressed to completely remove the potential barrier, there is nonetheless a non-zero chance for a bound electron to escape by tunnelling through the reduced barrier. This process is shown schematically in figure 2.1(b). The TI mechanism is not analytically solvable, but several numerical models exist. Well known models are the Keldysh model[58] and the ADK model[59,60], specifically for implementation in simulation codes. The tunnelling ionisation mechanism has to be considered as a relevant factor if a gas is used that is close to the BSI threshold for the chosen experimental parameters. It can have a relevant effect in ionisation injection, as the injection volume can differ compared to the purely classical approximation.

Generally, LWFA experiments are conducted using low-Z gasses, such as hydrogen or helium, for their relatively low ionisation thresholds. These are sufficiently low that in a high intensity laser pulse, e.g. $I_{peak} \sim 10^{19}$ W cm^{-2}, full ionisation of these gases will occur in the laser pedestal, a few picoseconds before the laser peak intensity is reached. This ensures a pure laser-plasma interaction at the high intensity region of the laser which drives the wakefield. This enables relativistic self-focussing (see section 2.3) and prevents ionisation defocussing of the high-intensity part of the laser pulse. Hydrogen has the lowest ionisation threshold and would be the logical gas medium choice were it not for its high reactivity, which poses a substantial explosion hazard if handled incorrectly. Therefore hydrogen is only used for specific applications where an as low as possible ionisation threshold is required, e.g. in discharge capillaries or e-beam driven ionisation. For ionisation by high-intensity lasers the ionisation level of helium is sufficiently low and therefore preferred as an inert and safe alternative.

If partial ionisation is desired, higher-Z atoms like nitrogen are used, either replacing or as a dopant in a low-Z gas. When the laser reaches I_{BSI} for certain electrons, other

electrons with a higher E_{ion} remain unionised. Only when and if the laser field becomes large enough these inner shell electrons become ionised. The ionisation injection scheme, as will be discussed later in section 2.6.1, uses this principle. In the work presented in this thesis a mixture of helium and nitrogen gas is used. From table 2.1, the helium and nitrogen L-shell (N^{1+} - N^{5+}) electrons are ionised by the laser pedestal at laser intensities between 1.4×10^{14} and 1.5×10^{16} W cm^{-2}, whereas nitrogen K-shell (N^{6+} & N^{7+}) electrons are only ionised close to the laser peak intensity at 1.0×10^{19} and 1.6×10^{19} W cm^{-2} respectively.

2.2. ELECTRON MOTION IN AN ELECTROMAGNETIC FIELD

In this section the motion of electrons in an electromagnetic field, e.g. a laser field, is discussed. This knowledge is necessary to understand how a wakefield is formed (section 2.4). It is also the foundation for understanding how a laser beam is able to stay self-focused over a long distance (i.e. beyond the Rayleigh length), as will be discussed in the section 2.3.

ELECTRON MOTION IN AN ELECTROMAGNETIC FIELD

For the description in the following section certain assumptions are made. We assume a fully ionised plasma, which is the case if the laser intensity is higher than I_{BSI} from equation (2.2). The ionised plasma is assumed to be cold after ionisation. Furthermore, in experiments treated in this thesis, the gas density of the target is low enough to assume an under-dense collision-less plasma. Although strong enough to achieve BSI and to rapidly accelerate free electrons, the external laser field is weak enough to assume immobile ions on the time-scale of interest, which will be shown in more detail in section 2.2.1. Taken these assumptions, the motion of free plasma electrons with charge e and rest mass m_e in an electromagnetic field is described by the Lorentz equation:

$$\frac{d(\vec{p})}{dt} = -e\left(\vec{E} + \vec{v} \times \vec{B}\right), \tag{2.3}$$

where $\vec{E}$ is the electrical field and $\vec{B}$ the magnetic field. $\vec{p} = \gamma m_e \vec{v}$ is the momentum of an electron and $\gamma = 1/\sqrt{1 - v^2/c^2}$ its relativistic Lorentz factor with c the speed of light in vacuum.

2.2.1. PONDEROMOTIVE FORCE

Ponderomotive force is a net force that drives electrons away from high-intensity regions to lower intensity regions of a spatially-varying electromagnetic field and stands at the basis of wakefield formation in LWFA. Figure 2.2 shows a schematic of the ponderomotive force in a Gaussian laser intensity profile.

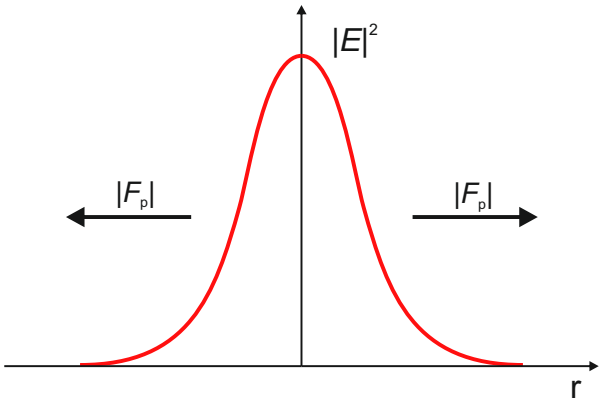

Figure 2.2.: **Schematic of the ponderomotive force** for a Gaussian intensity profile $|\vec{E}(r)|^2$ according to equation 2.6.

The concept of ponderomotive force will be first discussed for the case where $v \ll c$, the so-called non-relativistic regime. As $|\vec{B}| = |\vec{E}|c^{-1}$, the effect from the magnetic term $(\vec{v} \times \vec{B})$ in equation 2.3 can be neglected in this case. Equation 2.3 then reduces to

$$\frac{d(\vec{v})}{dt} = -\frac{e}{m_e}\left(\vec{E}\right). \tag{2.4}$$

From this equation the ponderomotive force perceived by an electron in a laser field E and frequency ω_0 can be derived[56]

$$\vec{F_p} \equiv \overline{m_e \frac{d(\vec{v})}{dt}} = -\frac{e^2}{4m_e\omega_0}\nabla\vec{E}^2. \tag{2.5}$$

For laser beams with a Gaussian profile, its electric field magnitude at a distance r from the center axis of the beam follows

$$\vec{E}(r) \sim E_0 \exp\left[\frac{-r^2}{w^2(z)}\right], \tag{2.6}$$

where $w(z)$ is the beam radius at a certain position z along the direction of propagation.

On the short time scale, plasma electrons will follow the rapid oscillations of the laser field. This motion following the laser frequency ω_0 is called the quiver motion and the associated quiver momentum is give by:

$$\vec{p} \approx \frac{e\vec{A}}{c}, \tag{2.7}$$

where $\vec{A}$ is the vector potential that describes the laser electromagnetic field.

On the longer time-scale, as follows from equation 2.6 and equation 2.5, an electron on average will perceive a ponderomotive force from the field envelope gradient. This force is pointing away from the high intensity centre region of the laser beam as illustrated in figure 2.2 and is proportional to the gradient of the intensity as $I \propto E^2$.

RELATIVISTIC REGIME

In the case above, with $v \ll c$, contributions by the magnetic laser field were neglected. Once $v \rightarrow c$, the magnetic term of the laser field can no longer be ignored. When this is the case, one says to be operating in the relativistic regime. A good measure to determine whether relativistic effects should be considered is the laser normalised vector potential[61]

$$a_0 = \sqrt{\frac{2e^2\lambda_0^2 I}{\pi m_e^2 c^5}} \simeq 0.86 \times 10^{-9} \lambda_0[\mu\text{m}] \sqrt{I[\text{W cm}^{-2}]}, \tag{2.8}$$

with λ_0 the central laser wavelength and I the laser intensity.

As can be seen from equation (2.8), a_0 grows with increasing laser intensity and follows a square root dependency. Once a_0 equals unity, the kinetic energy gained by an electron in half a wave-cycle is roughly the same as its rest energy $E_{\text{rest}} = m_{e,0}c^2$. Relativistic effects become relevant in the relativistic regime when $a_0 \gtrsim 1$. At this point the $\vec{v} \times \vec{B}$ term in equation 2.3 has to be included, giving rise to electron motion along the z-propagation axis. The minimum intensity to reach the relativistic regime ($a_0 = 1$) is called the threshold relativistic intensity I_0:

$$I_0\lambda^2 = 1.37 \times 10^{18}\ \text{W}\ \mu\text{m}^2\ \text{cm}^{-2}. \tag{2.9}$$

The expression for the ponderomotive force given in equation (2.5) is only valid for the non-relativistic case. The derivation for the relativistic case, taking magnetic fields and relativistic momentum and mass into account, is more complex and is treated in ref.[62] and ref.[63]. As in the non-relativistic case, the relativistic ponderomotive force in radial direction is proportional to the electric field gradient squared.

ION MOVEMENT IN AN ELECTROMAGNETIC FIELD

As ions are also charged particles, they will also interact with the laser electromagnetic field and any potential wakefields formed by the laser-plasma interaction. Due to the large mass and corresponding momentum of ions compared to electrons, a much higher threshold intensity is required to enter the relativistic regime:

$$I_p\lambda^2 = \left(\frac{m_p}{m_e}\right)^2 I_0\lambda^2 \approx 5 \times 10^{24}\ \text{W}\ \mu\text{m}^2\ \text{cm}^{-2}, \tag{2.10}$$

where m_p is the proton mass. This intensity is around six orders of magnitude higher compared to the intensity required for electrons and five orders of magnitude higher than intensities typically reached during LWFA experiments. The low momentum reached by ions is such that they can be considered immobile on the time scale at which LWFA takes place.

2.3. GUIDING OF HIGH-INTENSITY ULTRA-SHORT LASER PULSES

In LWFA, a high intensity laser pulse is required to form a large amplitude plasma wakefield suitable to accelerate electrons. Specifically in the blow-out regime, the ponderomotive force of the laser has to be large enough to completely expel all electrons from the laser's propagation path. In order to reach the intensities required to achieve this, the laser pulse has to be tightly focussed, typically in the order of tens of micrometers. A focussed laser pulse in vacuum diverges quickly after its focus and therefore the peak intensity will reach the required value only over a small distance unless a guiding mechanism is present. The characteristic distance in which a laser stays focussed is called the Rayleigh length and is defined as the length before and after the focus where the intensity is still half that of the intensity:

$$z_R = \frac{\pi w_0^2}{\lambda_0}. \tag{2.11}$$

After a Rayleigh length z_R the beam waist[1] w has increased by a factor $\sqrt{2}$ compared to the beam waist w_0 at the focus. λ_0 is the laser central wavelength.

To illustrate; a laser pulse with a central wavelength of 800 nm focussed down to a typical beam waist of 17 µm has a Rayleigh length of only 0.8 mm. In contrast, in LWFA a long interaction length of several millimetres up to centimetres is desired in order to be able to accelerate electrons to high energies. A high laser intensity being required over the entire interaction region, the laser beam has to be confined to a small spot size over several times the Rayleigh length.

One method to achieve this is by providing the laser with an external density gradient guiding structure created by a discharge capillary[64]. However, as will be discussed in section 3.4, among other disadvantages, operation of such a discharge capillary is challenging. Instead one can rely on the non-linear self-focussing effect[65] to prevent defocussing, leading to non-linear self-guiding of the laser beam over large distances up to many time the Rayleigh length. Self-guiding is achieved when a laser pulse locally influences the refractive index of the plasma medium such that a guiding structure is formed capable to guide the pulse due a radial refractive index change, similar as in an optical guiding fibre.

The refractive index in a plasma can be expanded as:[38,61]

$$\eta(r) = \frac{ck}{\omega} \simeq 1 - \frac{\omega_{p,0}^2}{2\omega^2}\left(1 + \underbrace{\frac{\Delta n_c}{n_{p,0}}\frac{r^2}{w_0^2}}_{\text{external}} + \underbrace{\frac{\Delta n(r)}{n_{p,0}}}_{\text{density depletion}} - \underbrace{\frac{a_0^2}{4}}_{\text{relativistic effect}}\right). \tag{2.12}$$

Here $n_{p,0}$ is the unperturbed plasma density and ω is the laser frequency. The plasma frequency ω_p is dependent on the plasma density:

[1] $1/e^2$ radius

$$\omega_p = \sqrt{\frac{n_p e^2}{\epsilon_0 \gamma m_e}}, \tag{2.13}$$

with e the elementary charge and ϵ_0 the permittivity of free space.

In equation (2.12), the first labelled term represents an external pre-formed density channel if present. To optically guide a Gaussian laser pulse with spot size w_0, a channel depth of $\Delta n_c = 1/\left(\pi r_e w_0^2\right)$ is required[61]. Where $r_e = e^2/\left(mc^2\right)$ represents the classical electron radius. The second term describes the local change in plasma density Δn due to the ponderomotive force. The third term relates to relativistic self-guiding. Here electrons are accelerated to relativistic speeds in the strong laser field, gaining mass by the relativistic factor γ. This creates a self-guiding channel if $a_0^2/8 \gtrsim 4/\left(k_p w_0\right)$ or $P > P_c$. Here P_c is the critical laser power for relativistic self-guiding[61,65]:

$$P_c[\mathrm{GW}] \simeq 17\left(\lambda_p/\lambda\right)^2. \tag{2.14}$$

However, a self-guiding channel does not form instaneous. Due to the electrons inertia, the channel will form roughly c/ω_p behind the laser pulse's leading edge[66] leaving the front of the laser pulse unguided. Nonetheless, an ultrashort laser pulse can still be guided as the front of the pulse experiences local pump depletion, i.e. the transfer of part of the photons' energy to the wakefield leading to a localised frequency down-shift. The remaining part of the pulse being unaffected, group velocity dispersion causes down-shifted photons to slip backwards in the frame of the pulse with an etch velocity given by:

$$v_{etch} = \frac{c\omega_p^2}{\omega^2}. \tag{2.15}$$

Down-shifted photons slip back into the wake where the density gradient is sufficient for guiding[66].

2.4. PLASMA BASED ACCELERATION

As a laser pulse propagates through a plasma, electrons are displaced from the laser path by its ponderomotive force. Ions are immobile on the short time-scale and a charge separation occurs. Displaced electrons will be attracted back towards their original position by a strong Coulomb force on a time-scale related to the plasma frequency given by equation (2.13). Electrons returning to the laser propagation axis have gained momentum and overshoot their original position, resulting plasma oscillations forming behind the laser-pulse co-propagating with the laser group velocity v_g and a spatial period roughly equal to the plasma wavelength $\lambda_p = 2\pi c/\omega_p$ as illustrated in figure 2.3.

The strong electromagnetic fields generated by such a wakefield can be several order of magnitude larger than found in conventional RF accelerator cavities. As the wakefield travels almost with the speed of light, electrons injected within the right phase and with a sufficient initial momentum can be accelerated to high energies within a single plasma cavity.

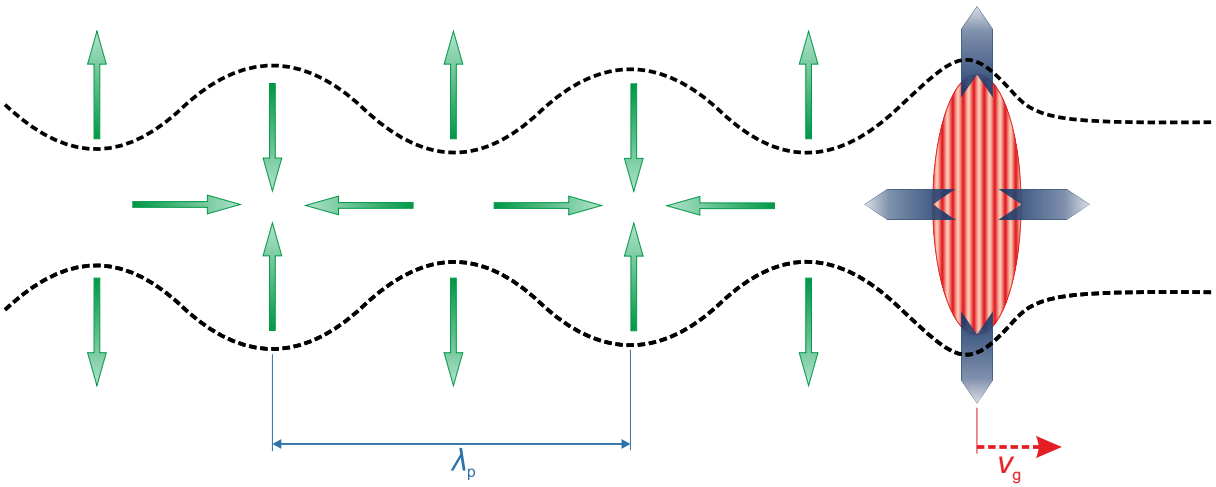

Figure 2.3.: **Schematic representation of ponderomotive wakefield excitation.** The laser pulse (red) is moving with the laser group velocity v_g towards the right. The ponderomotive force (blue arrows) pushes electrons out of the laser's path, after which a co-travelling wakefield is formed behind the laser pulse. The dashed curves are example electron trajectories. The separation of charge induces strong electrostatic forces (green arrows).

In a weakly non-linear wake the strength of the wakefield is in the order of the non-relativistic wave-breaking field E_0[67]

$$E_0\,[\mathrm{V/m}] = \frac{m_e c \omega_p}{e} \simeq 96\sqrt{n_{p,0}\,[\mathrm{cm^{-3}}]}. \tag{2.16}$$

For a typical electron density of 10^{18} cm^{-3} this yields a field strength of $E_0 \simeq 100$ GV/m. Compared to a typical value for conventional superconducting accelerators of 10 MV/m the gradient in a linear plasma wakefield is larger by three orders of magnitude.

DEPHASING

Once an injected electron reaches relativistic energies it will approach the speed of light and will slowly move forward with respect to the wake. Eventually it will reach the decelerating phase of the wakefield. This limits the maximum acceleration length, and thus maximum achievable electron energy. The maximum interaction distance over which an electron remains in the accelerating phase is known in as the dephasing length L_d.

As the front of the laser pulse etches backward with velocity v_{etch} (equation (2.15)), the phase velocity of a laser-driven wake can be expressed by $v_\phi \simeq v_g - v_{etch}$. The linear group velocity v_g of a laser in an underdense plasma is given by[68]

$$v_g = c\sqrt{1 - \omega_p^2/\omega_0^2}. \tag{2.17}$$

From equation (2.17) and (2.15):

$$v_\phi \simeq v_g - v_{etch} \simeq c\left[1 - \frac{2}{3}\frac{\omega_p^2}{\omega_0^2}\right]. \tag{2.18}$$

From this follows that the distance travelled by a relativistic electron, injected at the back of a plasma cavity, until it enters the decelerating gradient of a wakefield is given by

$$L_d \simeq \frac{c}{c - v_\phi}\lambda_p \simeq \frac{2}{3}\frac{\omega_0^2}{\omega_p^2}\lambda_p. \tag{2.19}$$

1-D DESCRIPTION OF A WAKEFIELD

A quantitative description of the excitation of a laser driven wakefield can be given using an one-dimensional model where the motion of electrons is only considered along the longitudinal coordinate z. In the linear regime, i.e. $a_0 \ll 1$ and $E \ll E_0$, the plasma wake has a simple sinusoidal shape. However once the laser intensity becomes larger ($a_0 \geq 1$), the plasma response becomes highly non-linear. In the following model it is assumed that the driver laser is non-evolving, i.e. does not evolve over time and is only a function in the co-moving frame $\xi = z - v_\phi t$. This enables application of the quasi-static approximation[69,70], which requires that the laser pulse envelope evolution is much slower than the plasma response. The wakefield phase velocity v_ϕ is assumed to be equal to the laser group velocity v_g (equation (2.17)) in this case.

For a Gaussian shaped laser pulse propagating longitudinally along z and linearly polarised in x-direction, the normalised vector potential is given by

$$\vec{a} = \hat{a}(z, t)\cos(k_0 z - \omega_0 t)\vec{e}_x \tag{2.20}$$

The shape envelope function $\hat{a}$ represents the Gaussian longitudinal evolution of the pulse given by

$$\hat{a}(\xi) = a_0 \exp\left(-\xi^2/L_0^2\right), \tag{2.21}$$

with a_0 the normalised laser vector potential according to equation (2.8) and L_0 the laser pulse length. The plasma wakefield can be described by its normalised electrostatic potential $\psi = e\Phi/m_e c^2$ which can be found by solving[67]

$$\frac{\delta^2\psi}{\delta\xi^2} = k_p^2\gamma_p^2\left[\beta_p\left(1 - \frac{1 + a^2}{\gamma_p^2(1 + \psi)^2}\right)^{-1/2} - 1\right], \tag{2.22}$$

with $\beta_p = v_\phi/c$ and $\gamma_p = \left(1 - \beta_p^2\right)^{-1/2}$ the Lorentz factor of the plasma wave phase velocity. The plasma wavenumber is given by $k_p = \omega_\phi/v_\phi$.

Equation 2.22 is the one-dimensional non-linear equation which is also valid for $a_0 > 1$. This differential equation cannot be solved analytically and has to be solved numerically instead. Once solved, other relevant wakefield parameters can be derived. The axial accelerating electric field of the wake normalised to E_0 is given by

$$\frac{E_z}{E_0} = \frac{c}{\omega_p}\frac{\delta\psi}{\delta\xi}. \tag{2.23}$$

And the plasma density perturbation is given by

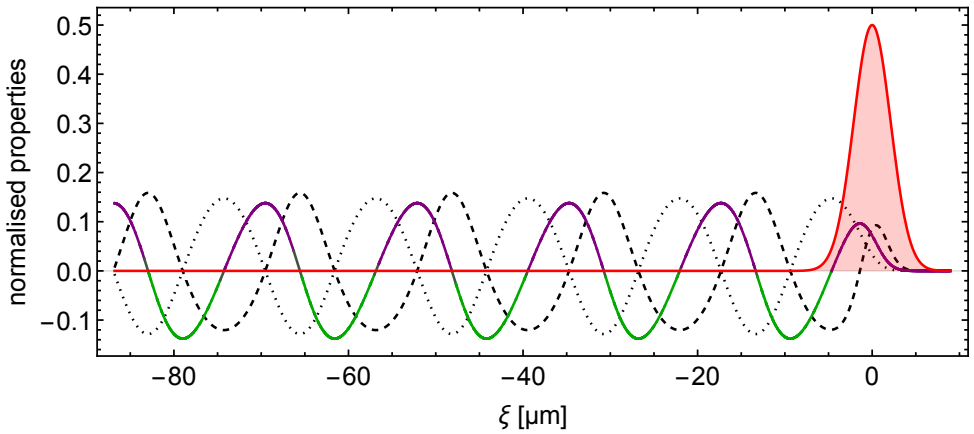

(a) $a_0 = 0.5$

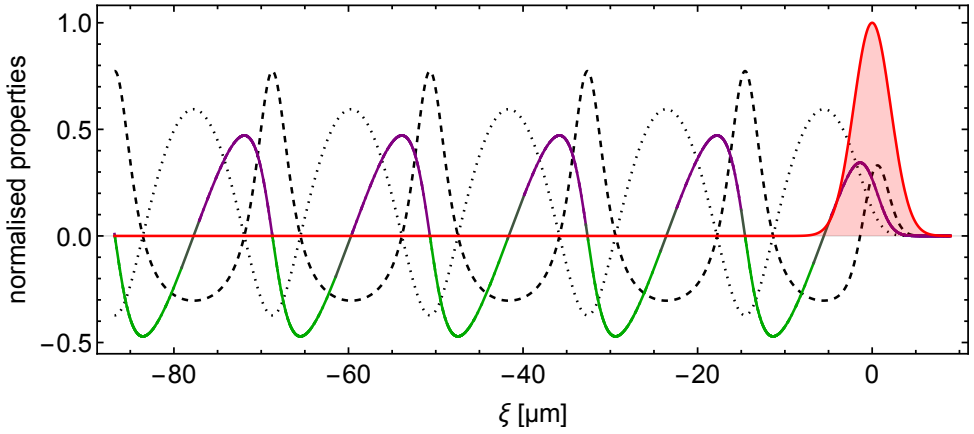

(b) $a_0 = 1.0$

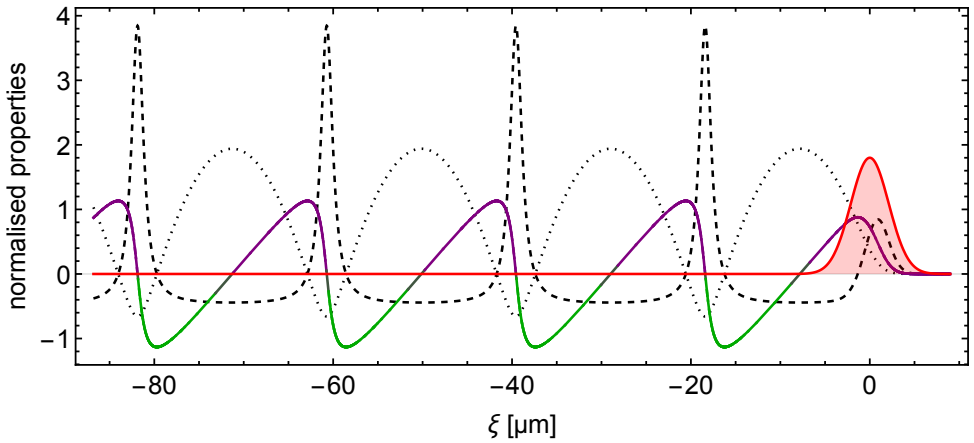

(c) $a_0 = 1.8$

Figure 2.4.: **One-dimensional wakefields in the quasi-static approximation.** The wakefields are driven by a ten fs laser pulse (*red line*) for different a_0 at a plasma density of $3.7 \times 10^{18}\,\mathrm{cm}^{-3}$. The *dotted line* represents the wakefield normalised potential ψ, which is found by numerically solving equation (2.22). The *dashed line* represents the plasma density according to equation (2.24). The accelerating electric field normalised to E_0 according to equation (2.23) is represented by the *purple/green line*, with green the accelerating gradient and purple the decelerating gradient.

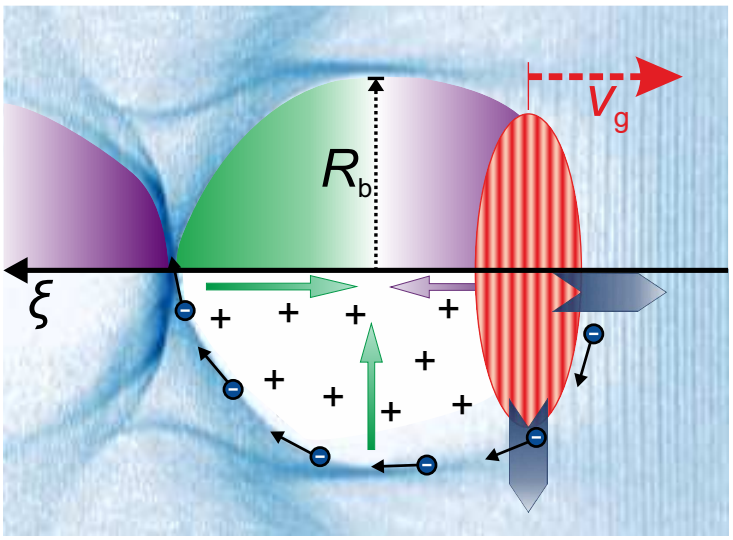

Figure 2.5.: **Schematic representation of the bubble regime.** The laser pulse (red) is moving with the laser group velocity v_g towards the right. The electron density is shown in blue. No electron bunch is injected into the wakefield yet in this scenario. *The bottom half* shows how the ponderomotive force (blue arrows) pushes electrons out of the laser's path. Sketched is the path of electrons following the innermost path. A negatively charged electron sheath is formed, around the positively charged inner region which is void from electrons. The separation of charge induces strong electrostatic forces (green and purple arrows). *The top half* shows the longitudinally for electrons accelerating (green) and decelerating (purple) field.

$$\frac{n_{p,1}}{n_{p,0}} = \gamma_p^2 \beta_p \left[\left(1 - \frac{1 + a^2}{\gamma_p^2 (1 + \psi)^2} \right)^{-1/2} - \beta_p \right]. \tag{2.24}$$

Figure 2.4 shows the solution to equations (2.22)-(2.24) for various a_0. In the linear case, as shown in subfigure 2.4(a), the plasma shows a mostly sinusoidal response. As the laser intensity increases, the plasma response becomes more non-linear. At $a_0 = 1$ the plasma density distribution becomes more peaked with an increase of the wakefield period length. This results in a slightly skewed electric field with an increased amplitude. In the non-linear regime these effects become even more pronounced as can be seen in subfigure 2.4(c) for $a_0 = 1.8$. At this point the wakefield length increases further while the plasma density distribution becomes even stronger peaked. The accelerating gradients grow further in amplitude and become almost linear between the plasma density peaks.

2.5. BUBBLE REGIME

In this work, laser wakefield acceleration occurs is the so-called bubble or blowout regime. Investigated for electron beam drivers before[71], this highly relativistic regime was identified for laser drivers by Pukhov and Meyer-ter-Vehn[22]. It constitutes a special case where all electrons on the laser path are fully expelled by the ponderomotive force, leaving behind a three-dimensional bubble shaped cavity which is completely void of electrons behind the laser driver as illustrated in figure 2.5. This regime occurs for high

laser intensities where the laser normalised vector potential a_0 is higher than two and the laser pulse length is short compared to the plasma wavelength, i.e. $c\tau \lesssim \lambda_p$.

In order to generate an ideal spherically shaped wake with a radius R_b, the spot size of the driver is required to be matched to this radius, i.e. $w_0 \simeq R_b$. Through simulations by Lu et al. it was found that the spot size required for this condition is given by[38,66,72]

$$k_p w_0 \simeq k_p R_b = 2\sqrt{a_0}. \tag{2.25}$$

In this case a matched spot size condition can be formulated as

$$w_0 \simeq R_b = \frac{2c\sqrt{a_0}}{\omega_p}. \tag{2.26}$$

From this we find that the bubble radius scales with the square root of a_0 and inversely with the plasma frequency. Although for a perfect bubble wakefield an a_0 of at least four is required, blowout also occurs where $2 \lesssim a_0 \lesssim 4$ with a cavity deviating slightly from the ideal spherical shape[38].

If the matching condition is not met and a too small laser spot size is chosen ($w_0 < \lambda_p$), electrons are not expelled far enough from the laser path to form a bubble. Instead, electrons can move back into the laser pulse envelope, leading to beam breakup, as is shown by Thomas et al.[73]. In the same work it is also shown that if the spot does not match precisely, a (slightly) larger spot will converge to and oscillate around the matched spot size for the remainder of the interaction. Once a bubble wakefield is formed, it can be sustained over many time the Rayleigh length as long as the laser power is above the critical power for self-guiding given by equation (2.14)[66,73].

One advantage of the bubble regime is the higher achievable acceleration gradient compared to a linear wake. The maximum accelerating field occurs at the back of the bubble and is given by[67,72]

$$E_{max} = \frac{R_b k_p}{2}\frac{m_e c\omega_p}{e} \simeq \sqrt{a_0}\frac{m_e c\omega_p}{e} = \sqrt{a_0}E_0, \tag{2.27}$$

assuming that the matched spot size condition is fulfilled. We find that the maximum accelerating field in the bubble regime is considerable higher than found in the non-linear regime, by a factor of and scaling with the square root of a_0.

Besides the large longitudinal field, a bubble wakefield also contains a very strong transversal focussing field that enables charges to be contained within the wakefield. In a co-moving frame $\xi = ct - z$ where the driver laser is moving towards positive z and assuming a spherical bubble centred at $r = 0$ and $\xi = 0$ the position dependent field in longitudinal direction is given by[67,72,74]

$$E_z \simeq \frac{k_p \xi}{2}E_0, \tag{2.28}$$

the radial electric field is given by

$$E_r \simeq \frac{k_p r}{4}E_0, \tag{2.29}$$

and the azimuthal magnetic field is given by

$$B_\theta \simeq -\frac{k_p r}{4} E_0. \tag{2.30}$$

Note that equation (2.27) is a special case of equation (2.28) where $\xi \simeq R_b$. The transverse wakefield forces have an electromagnetic nature such that a relativistic electron moving off-axis experiences a focussing force $F_r = E_r - B_\theta = (k_p r/2)E_0$. Because the focusing forces are linear, the normalised emittance of an electron bunch will be preserved during acceleration.

From equation (2.28) we can see that the acceleration gradient experienced by an electron does not depend on its radial position. Therefore in the bubble regime no extra energy spread is induced for an electron bunch with a radial finite size. For the radial field we find from equations (2.29) & (2.30) that there is no dependency on ξ. Thus the focussing force is independent of the transversal position within the bunch. This case for the bubble regime, $\delta E_z/\delta r = \delta F_r/\delta \xi = 0$, is a special case of the Panofsky-Wenzel theorem $\nabla_r F_z = F_r/\delta\xi$[75,76]. This is not only the case for an unloaded bubble, but also applies up to a certain radius around the centre if a bubble is significantly loaded with a high charge electron bunch[55]. This is shown for δF_r in section 4.5.1, specifically figure 4.11.

From the considerations discussed before, it now becomes clear why, ever since this regime became accessible with the rise of high-power laser systems, the bubble regime has become the preferred regime to operate an LPA at, even for its highly nonlinear behaviour. Compared to conventional accelerators, due to the small dimensions of LPAs, a relatively large fraction of the cavity is filled. Where in the (quasi non-)linear regime the longitudinal field depends on the transversal position of the bunch, this is not the case for the bubble regime, avoiding related energy spread.

Due to the strong fields, the bubble-shaped cavities can contain and accelerate large quantities of charge. Furthermore, the linear focussing forces inherently present in the bubble regime enables emittance conservation during the acceleration process[77]. Even high bunch charges can be confined over long interaction distances without degrading the beam quality, whereas in the (quasi non-)linear regime the with charge increasingly non-linear focussing fields will inevitably lead to emittance growth.

Finally, the required conditions to enter the bubble regime match the conditions required for nonlinear guiding of the driver laser pulse discussed in section 2.3. Thus, as long as the laser power is above the critical laser power for self-guiding, this regime is able to confine and accelerate high charge beams while sustaining this process over long interaction length without the need of an external beam and laser confinement.

2.5.1. SCALING LAWS AND LIMITATIONS

No comprehensive theory exists which is able to fully describe LWFA in the bubble regime. Fully analytical theories are limited to linear fluid theory[78] or one-dimensional non-linear fluid theory[79–81], which are not sufficient to describe the complex wakes and their electromagnetic fields in the bubble regime where relativistic mass effects are important and trajectory crossing occurs. This complex regime with bubble shaped three-dimensional wakefields cannot be fully analytically described. Instead, theoretical

descriptions generally largely rely on input data from numerical particle-in-cell (PIC) simulation studies in order to create analytical approximate models[72,82].

Using this approach, scaling theories have been developed which are able to predict under which experimental conditions the blowout regime can successfully be operated together with key parameters of generated electron bunches. The most prominent scaling theories are developed by Gordienko and Pukhov[37] and by Lu et al.[38]. Both scalings offer a similar approach, but have some key differences. Gordienko and Pukhov take a similarity theory approach with scalings based on simulations performed at very high laser intensities with an a_0 between twenty and eighty and relative high plasma densities. Lu et al. used a more phenomenological approach and base their scaling on more realistic laser parameters starting with an a_0 of two.

In this section the scaling laws from Lu et al.[38] will be presented to give an overview of important considerations in operating a LWFA accelerator in the blowout regime. For these scaling laws it is assumed that the laser spot size is matched to the bubble radius according to equation (2.26). The bunch charge and its effect on the acceleration process will not be treated here, but later in section 2.7.

DEPLETION LENGTH

In order to enter and maintain the blowout regime, a sufficiently high laser intensity is required such that $a_0 \gtrsim 2$. To maintain this condition over a long interaction length we rely on relativistic self-guiding as discussed in section 2.3. As long as the laser field is strong enough ($a_0 > 2$), it is able to sustain the bubble shaped wakefield necessary to accelerate electrons.

However, as the laser propagates through the plasma and drives the wake, energy of the laser field is transferred to the wakefield. Once the power of the laser is depleted below the critical power P_c as given by equation (2.14), self-focussing is no longer sustained. The laser beam will diverge and the plasma bubble will collapse shortly after. The distance a short laser pulse can travel in an underdense plasma before it can no longer sustain self-focussing is related to the etching velocity v_{etch} as given in equation (2.15) and is known as the pump depletion length:

$$L_{pd} \simeq \frac{c}{v_{etch}} c\tau \simeq \frac{\omega_0^2}{\omega_p^2} c\tau. \tag{2.31}$$

Ideally, experimental parameters should be chosen such that the pump depletion length L_{pd} is at least as long as the desired interaction length.

DEPHASING LENGTH

As in the case of a linear wakefield discussed in section 2.4, relativistic electrons in the bubble will move forward in respect to the wakefield and will ultimately leave the accelerating region of the wakefield (green region in figure 2.5) and reach a decelerating phase (purple region), which is known as dephasing.

Analogue to the linear case, related to the laser pulse etching velocity according to equation (2.15), the distance that electrons travel until they enter the decelerating gradient of the bubble is given by

$$L_{\mathrm{d,bubble}} \simeq \frac{c}{c - v_\phi} R_\mathrm{b} \simeq \frac{2}{3}\frac{\omega_0^2}{\omega_\mathrm{p}^2} R_\mathrm{b}, \tag{2.32}$$

with R_b the radius of the bubble. Although the interaction length can be shorter, to fully exploit the wakefield and reach the highest achievable energy the interaction length after injection should be matched to the dephasing length.

ELECTRON ENERGY

The maximum reachable energy is achieved when electrons are accelerated from the back of the wakefield, where the accelerating gradient is maximum, till the point where dephasing occurs and the accelerating gradient becomes zero, i.e. for an accelerating length equal to the dephasing length according to equation (2.32). The maximum accelerating gradient is given given by equation (2.27). For this non-linear wake, the wakefield longitudinal accelerating gradient decreases roughly linear to zero at the transition point from accelerating to decelerating phase, similar to the one-dimensional non-linear case shown in figure 2.4(c). Thus, the average useful wakefield is given by

$$E_\mathrm{avg,d} \simeq \frac{E_\mathrm{max}}{2} \simeq \frac{m_\mathrm{e} c \omega_\mathrm{p}}{2e}\sqrt{a_0} \tag{2.33}$$

Combining equations (2.26), (2.32) and (2.33) we can write the approximate equation for the maximum energy gain:

$$\Delta E \simeq \frac{2}{3} m_\mathrm{e} c^2 \frac{\omega_0^2}{\omega_\mathrm{p}^2} a_0 \simeq m_\mathrm{e} c^2 \left(\frac{P}{m_\mathrm{e}^2 c^5/e^2}\right)^{1/3} \left(\frac{n_\mathrm{c}}{n_\mathrm{p}}\right)^{2/3} \tag{2.34}$$

$$\Delta E[\mathrm{GeV}] \simeq 1.7 \left(\frac{P[\mathrm{TW}]}{100}\right)^{1/3} \left(\frac{10^{18}}{n_\mathrm{p}[\mathrm{cm}^{-3}]}\right)^{2/3} \left(\frac{0.8}{\lambda_0[\mu\mathrm{m}]}\right)^{4/3} \tag{2.35}$$

with n_c the critical plasma density. From equation (2.34) follows that higher electron energies can be achieved by lowering the plasma density. This can be counter-intuitive as the accelerating field decreases for decreasing plasma densities with $E_\mathrm{max} \sim \sqrt{n_\mathrm{p}}$ from equation (2.27). However, lower plasma densities result in a larger bubble radius, resulting in a longer dephasing length as shown in equation (2.32). As the dephasing length has a stronger dependency on the plasma density ($L_\mathrm{d,bubble} \sim 1/n_\mathrm{p}$), lower plasma densities have the potential for higher electron energies. This only holds true as long as the acceleration process takes place till the depletion length is reached. If the acceleration process is interrupted before $L_\mathrm{d,bubble}$ is reached, higher plasma densities achieve a higher electron energy for equal acceleration length.

The achievable electron energy only has a weak dependency on laser power. However, if the LPA is operated at a lower plasma density, a larger laser power is required to ensure self-guiding as follows from equation (2.14).

2.6. INJECTION SCHEMES

Controlling the injection mechanism is vital for laser plasma acceleration as final beam parameters such as charge, energy spread and emittance are determined by the injection

process and in the best case conserved during the acceleration process. Controlled injection of electrons into the accelerating bubble structure is one of the biggest challenge in laser plasma acceleration.

In conventional accelerators electrons are injected from an external source. There the main challenge is to time injection such that electrons enter the accelerator in the correct accelerating phase. With accelerator cavities generally in the centimetres to several decimetres in size with equally long accelerating field wavelengths, the weak spatial variation in acceleration gradient makes injection timing requirements relatively relaxed. In contrast, for LPAs the accelerating structures are co-moving with the driver laser at nearly the speed of light and have a size in the order of several tens of micrometres. Ultra-short ($\tau_{bunch} < \lambda_p/c$) bunches with a certain initial momentum are required which have to be injected into the LPA with micrometre positioning and sub-femtosecond timing precision. Any injection timing mismatch or positioning error will cause electrons to be placed in the incorrect phase of the wakefield leading to ejection of the bunch from the wakefield or degradation of the final beam parameters.

Abovementioned requirements are very challenging to reach for conventional electron beam technology such as radio-frequency (RF) photo-injectors. Although external injection of electrons in laser wakerfield acceleration has been demonstrated[83–85], these experiments have not been able to provide high-quality mono-energetic beams and instead exhibit a broadband energy distribution. An alternative scheme where a few MeV electrons from an RF-injector are injected into a plasma in front of the driver laser pulse has been proposed[86–91]. Although this scheme predicts electron beams with a few pC charge and an energy spread at the percent level, it has not been experimentally demonstrated. Instead, the technical difficulties of coupling an RF-injector and an LPA are generally avoided by using alternative injection schemes where electrons are not injected externally, but from the background electrons present in the accelerating medium itself. This eases the technological challenges, but can have the disadvantage that acceleration and injection becomes coupled, reducing the tunability of the accelerator, as will be discussed in more detail for the individual injection schemes further below.

The accelerating gradients found in the bubble regime can reach several hundreds of GV/m, thus electrons can quickly reach considerable high energies within a short time. To illustrate, at a moderate acceleration gradient of 100 GV/m electrons reach 10 MeV within 100 fs, or 30 µm acceleration length. Electrons injected at different times can therefore achieve a substantial difference in energy gain. Therefore it is generally required to limit the injection time to restrain the energy spread gained from the injection process. At the same time, in order to maximise the current output of the accelerator, a large amount of charge must be injected. Depending on the laser power, several hundreds of pico-coulombs are required to reach the optimal loading condition as will be discussed in section 2.7 and demonstrated in chapter 5.

There are several schemes available for the injection of plasma background electrons into the bubble cavity, with each scheme having its own advantages and disadvantages.

The wave-breaking injection scheme[74,92] was the first widely used technique in the bubble regime due to its technical simple implementation. In this mechanism the wakefield is strongly driven and electrons are injected at the moment that the electric field amplitude reaches the limit where a non-linear wake structure can no longer be sustained. The name wave-breaking is borrowed from the analogy of surface water

	Implementation	Reproducibility	Energy spread	Charge
Wave-breaking	+	-	+ 5-20%	± 1-200 pC
Down-ramp	±	+	+ ∼10%	± 10-200 pC
Colliding pulse	-	+	+ ∼5%	- 5-50 pC
Ionisation	+	±	- 25-100%	++ <1000 pC
STII	+	+	+ ∼10%	± ∼100 pC
Tailored STII	+	+	+ ∼10-15%	+ ∼500 pC

Table 2.2.: **Tabular overview of injection methods' advantages and disadvantages.** Given number are typical values. A graphical overview can be found in ref.[1].

waves in fluid dynamics, where waves increase in amplitude, e.g. at the coast where the depth becomes smaller than the wavelength, and the crest becomes unstable (wave breaking), resulting in turbulent white-water overtaking and spilling down the face of the wave (injection). This effect is also seen in plasma waves when the maximum longitudinal velocity of plasma electrons become larger than the phase velocity of the wake.In the one-dimensional approximation the maximum sustainable field before wave breaking occurs in a cold plasma is given by[80,92]

$$E_{1D,max} = \sqrt{2(\gamma_\phi - 1)}\frac{m_e c \omega_p}{e} = \sqrt{2(\gamma_\phi - 1)}E_0, \tag{2.36}$$

with $\gamma_\phi \equiv (1-\beta_\phi^2)^{-1/2} \approx \omega/\omega_p$ and $\beta_\phi \equiv v_\phi/c$. In the three-dimensional case an estimated laser intensity corresponding to at least $a_0 = 4.3$ is required for self-injection to occur[93].

Although this technically simple mechanism is able to load several hundreds of picocoulomb charge in mono-energetic bunches[25,94], its non-linear nature results in large shot-to-shot fluctuations. Furthermore, the injection conditions are directly coupled to the wakefield operational parameters. Thus it is not possible to control the injection separately from the acceleration process itself.

The down-ramp or shockwave injection mechanism[92,95–100] offers better possibilities to decouple the injection parameters. This mechanism requires more technical effort, as a gas target with a well defined, and preferable adjustable, density step is required. Injection occurs at this sudden density step, reshaping the wakefield due to its dependency on the plasma density ($R_b \sim n_p^{-1/2}$). As the bubble quickly elongates at a density down-step, it encases and traps sheath electrons at the end of the bubble. This scheme is known for its reliable operation and offers better tunability compared to the wave-breaking scheme. The density step leads to a spatially and thus temporal limited injection, resulting to accelerated bunches with small energy spread. The amount of available electrons for injection is limited to available electrons in the sheath during the down-ramp, effectively limiting the maximum injected charge. Charges reported using this method are significant, but generally do not exceed 200 pC.

The colliding pulse scheme[36,101–103] uses a separate injection laser pulse to heat up and inject background electrons into the pump laser pulse driven wakefield. This technically challenging technique decouples electron injection from wakefield generation, allowing better tunability in energy gain, energy spread and injected charge than any other injection scheme. The injection volume is determined by the overlap of the driver and injection laser pulses, which can be easily adjusted. Electrons can be precisely injected at a specific point allowing to tune the acceleration length of injected electrons and thus their energy gain. The limited injection volume results in very low energy

spread. However, due to this very localised injection, this scheme is able to inject only several tens of pico-Coulomb of charge[102].

In contrast, ionisation injection[104–106] is able to inject a large amount of charge using an easy to implement technique. Here, the acceleration medium is doped with a small fraction of high-Z gas, e.g. nitrogen, whose K-shell electrons will be ionised and subsequently trapped only near the intensity peak of the laser as detailed in section 2.1. However, injection typically occurs over a long injection distance, thus resulting in large energy spread[104,107,108].

The Self-Truncated Ionisation Injection (STII) process, first identified in theory by Zeng et al.[109] in 2014, first demonstrated by Mirzaie et al.[110] in 2015 and discussed in more detail in section 2.6.1 below, is a modified ionisation injection scheme which aims to solve the large energy spread problem. Here a small mismatch in laser spot size with the plasma cavity radius is introduced, which, if appropriately chosen, causes the laser and wakefield to evolve such that the duration of electron injection into the wakefield becomes restricted. Although injection and acceleration are still coupled, this scheme offers some tunability, as the available electrons for injection can be easily tuned with the high-Z gas doping concentration. This scheme is able to load reasonably high charge (up to $\pm 100\,\mathrm{pC}$[110,111]) with low energy spread into a wakefield. Compared to wave-breaking, the main advantage of this scheme is its stability, able to reliably produce electron beams with stable parameters on a shot-to-shot basis.

In this PhD project, the STII process has been tailored using a combination of geometric and relativistic self-focussing to scale into the nanocoulomb-class. This tailored process will be discussed in detail in chapter 4.

A tabular overview of the advantages and disadvantages together with some typical values of discussed injection schemes is giving in table 2.2

In order to investigate beam-loading in laser wakefield acceleration as presented in chapter 5, several hundreds picocoulomb of charge are required to be loaded into the wakefield (see section 2.7). The only injection mechanisms available that can offer such high charges are the wave-breaking, ionisation & tailored STII techniques.

Although the wave-breaking injection mechanism is capable of delivering the required charge in a mono-energetic energy peak, the inherent shot-to-shot instability and lack of tunability makes this mechanism unsuitable for a systematic study. Classical ionisation injection does offer the required stability and tunability, but is not able to deliver mono-energetic electron beams. Although some beam-loading effects can be studied[112] in this regime, effects are coupled due to the long injection time and energy spread. The only feasible technique to unambiguous study beam loading effects with peaked mono-energetic beams up to and beyond the optimal loading condition is therefore the tailored STII scheme.

2.6.1. IONISATION INJECTION

For an electron which is ionised close to the laser peak intensity to become trapped into the wakefield, two conditions have to be met.

The first is the longitudinal trapping condition, which requires that an electron gains enough momentum between the point of ionisation and a trapping point within the

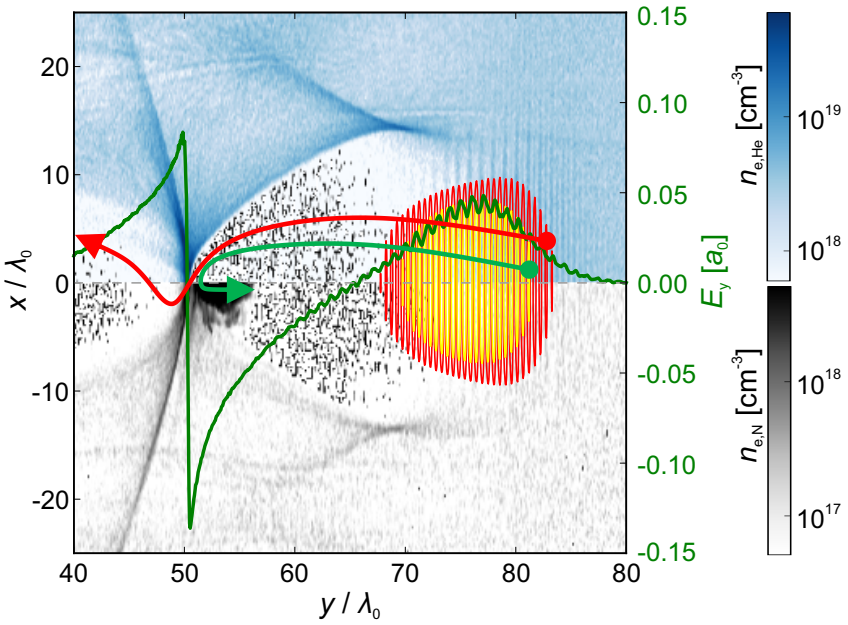

Figure 2.6.: **Schematic representation of ionisation injection in the bubble regime.** The laser pulse is propagating to the right, forming a bubble shaped wakefield. *The top half* of the figure shows the density distribution of electrons originating from helium. *The bottom half* shows the density distribution of electrons originating from the nitrogen K-shell. *The red region* indicates where the laser field is strong enough ionise N^{6+}. *The yellow region* shows where the laser field is strong enough to ionise N^{7+}. Two example trajectories of ionised nitrogen K-shell electrons are shown. *The red trajectory* shows a trajectory where the trapping conditions are not fulfilled; the electron is ionised, but not trapped. *The green trajectory* shows the trajectory of an electron born at a position where the trapping conditions are fulfilled; the electron is ionised and subsequently trapped. The longitudinal E-field is shown by the *green line graph*.

bubble such that the longitudinal electron velocity $v_{z,\mathrm{e}}$ reaches at least the wake phase velocity v_ϕ. The longitudinal trapping condition can be studied by considering the wake potential Φ, which is related to the wakefield according to equation 2.23[2]. With the potential change over time small compared to its variation over ξ, the quasi-static approximation can be applied. Furthermore, the initial velocity of an electron directly after ionisation is much smaller compared to the velocity gained during acceleration in the strong fields such that electrons can be assumed to initially be at rest. For an electron born at a position with an initial wake potential Φ_i the momentum gained while traversing to a position with a wake potential Φ is evaluated by:[113]

$$\gamma - \frac{v_\phi P_z}{m_\mathrm{e} c^2} - \frac{e}{m_\mathrm{e} c^2}\Phi = 1 - \frac{e}{m_\mathrm{e} c^2}\Phi_\mathrm{i}, \tag{2.37}$$

with γ the electron's Lorentz factor and $P_z = \gamma m_\mathrm{e} v_z$ the longitudinal momentum of the trapped electron with a charge $q = -e$.

Applying the minimal condition for trapping $v_z = v_\phi$ allows us to define the trapping condition from equation 2.37:

[2] Ψ is the wake potential Φ normalised to $\frac{e}{m_\mathrm{e} c^2}$

$$\gamma - \frac{\gamma v_\phi^2}{c^2} - \frac{e}{m_e c^2}\Phi_f = 1 - \frac{e}{m_e c^2}\Phi_i, \tag{2.38}$$

where Φ_f is the wakefield potential at the point where the electron becomes trapped. Normalising the wake potential, the longitudinal trapping condition can be written as

$$\Delta\Psi + 1 \leq \frac{\gamma}{\gamma_\phi^2} = \frac{1}{\gamma_\phi}, \tag{2.39}$$

with $\Delta\Psi = \frac{e}{m_e c^2}(\Phi_f - \Phi_i)$ and $\gamma_\phi = \left(1 - \frac{v_\phi^2}{c^2}\right)^{-1/2}$.

The second trapping condition is related to the region in the wakefield where the focussing force exerted on electrons overlaps with the wakefield's accelerating phase. Without the focussing field or in the presence of a defocussing field, an electron will be transversally omitted from the wakefield, either by remainder transversal momentum at the moment of injection or by Coulombic repulsion exerted from the injected bunch or the wakefield's electron sheath.

Therefore an electron needs to catch up with the wakefield, i.e. fulfil the longitudinal trapping condition, in the focussing region of the wakefield to fulfil the transversal trapping condition. The focussing field which transversally confines an electron is governed by the electric and magnetic field present in the bubble according to the Lorentz equation given by equation (2.3). Especially in the loaded case the B-fields play a crucial role in the focussing force, as will be shown in section 4.5.1 & figure 4.11. The minimum longitudinal potential of the wakefield can be situated outside the focussing region of the bubble and is therefore not intrinsically the value that has to be taken into account when evaluating whether the trapping condition is fulfilled, i.e. $\Phi_{min} \neq \Phi_f$ in equation 2.39. The process of ionisation injection is conceptionally shown in figure 2.6.

This section described the conditions for ionisation induced injection. In chapter 4 the tailored STII scheme will be discussed in more detail.

2.7. BEAM LOADING

Acceleration of several hundreds picocoulomb of charge has been demonstrated in LWFA[1,3]. Combined with the typical few-femtosecond bunch durations[26,28,35,36] such an accelerator can provide several tens of kilo-ampere peak currents[3,39]. LPAs generating such high currents contain enough charge such that the self-field of the bunch will superimpose the wakefield. Consequently, the wakefield structure will be reshaped and the effective accelerating field along the bunch will be modified affecting the beam dynamics and final beam parameters, i.e., transverse dynamics, emittance, final energy and energy spread. This phenomenon is generally known as beam loading.

The wakefield deformation caused by beam loading is generally seen as a negative effect due to its potential to degrade the final beam quality. However, if properly controlled, beam loading can be employed to increase the accelerator's performance.

Figure 2.7 illustrates the beam loading effect on the longitudinal field in an one-dimensional wakefield. Figure 2.7(a) shows the first period of an unloaded non-linear

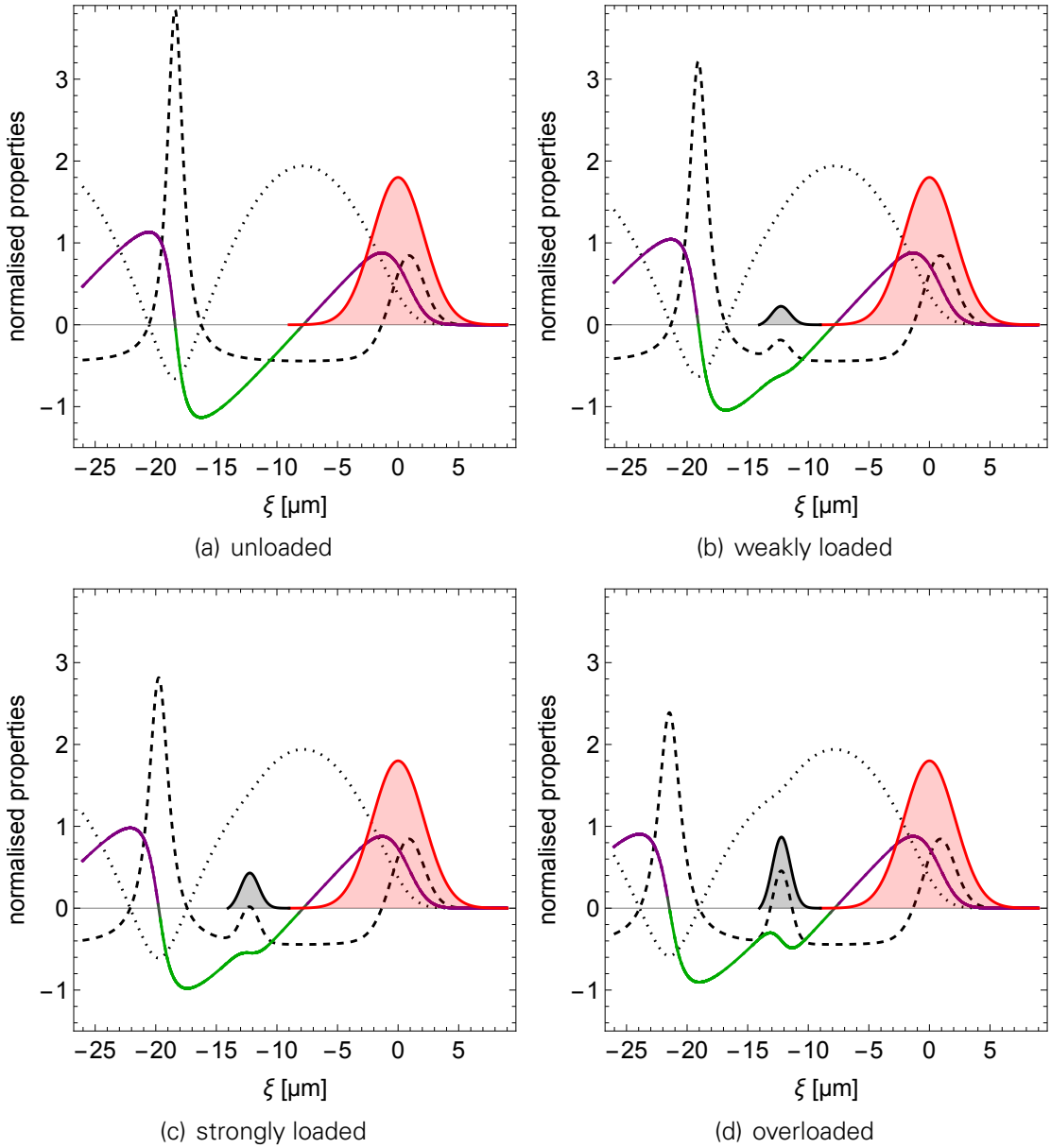

Figure 2.7.: **Beam loading effect.** Shown are one-dimensional wakefields in the quasi-static approximation. The wakefields are driven by a ten fs laser pulse (*red line*) for a $a_0 = 1.8$ at a plasma density of $3.7 \times 10^{18}\,\mathrm{cm}^{-3}$, equal to the case as in figure 2.4(c). Within the laser-driven wakefield different electron bunch loads (*solid black line*) are placed to illustrate their effect on the wakefield. The *dotted line* represents the wakefield normalised potential Ψ. The *dashed line* represents the plasma density. The accelerating electric field normalised to E_0 is represented by the *purple/green line*, with green the accelerating gradient and purple the decelerating gradient.

wakefield as previously shown in figure 2.4(c) where no charge is injected into the wakefield. Figure 2.7(b)-2.7(d) show the effect of increasingly high loads injected into the wakefield. Visible is that an injected charge deforms the wakefield and decreases the accelerating field magnitude, while the wake period becomes elongated due to the presence of a load.

Important to note is that the beam loading effect is most strongly visible locally within the co-moving frame at the position of the injected bunch. Therefore the bunch directly influences the accelerating field experienced by itself. Firstly, the reduction of the accelerating gradient will reduce the overall achievable electron energy for a certain acceleration length. Secondly, a local flattening of the wakefield occurs due to the beam loading, changing the accelerating gradient distribution along the bunch. This effect can be employed to minimise the energy spread of an injected electron bunch. As a bunch always has a certain finite length, the accelerating gradient experienced by an individual electron depends on its position within the bunch. In the weakly loaded case as illustrated in figure 2.7(b), electrons at the front of the bunch experience a significant lower accelerating gradient compared to electrons at the back of the bunch. In this case, the energy spread within the bunch will grow during acceleration.

In figure 2.7(c) this effect is counteracted with an increase of injected bunch charge, leading to further flattening of the wakefield along the bunch. Although the achievable maximum and mean electron energy will be lower due to the overall decrease of the wakefield amplitude, the energy spread added during the acceleration process is minimised in this case.

Figure 2.7(d) show the so-called overloaded case, where the strong load overcompensates the wakefield gradient along the bunch. An even stronger reduction in accelerating field occurs and the high self-fields of the bunch strongly deform the wakefield such that the accelerating gradient again becomes variable along the bunch. In contrast to the weakly loaded case, trailing electrons now experience a lower accelerating field compared to leading electrons. This situation is generally unfavourable, except for the case where a previously chirped beam, e.g. by acceleration in the weakly loaded case, requires de-chirping.

Generally it is desirable to operate an accelerator with a specific load such that accelerating field becomes constant along the bunch, this is the so-called optimal loading condition. When fulfilled, a bunch can be accelerated for long acceleration distances without the addition of energy spread. In section 2.7.1 the theory of beam loading in the linear case will be discussed in more detail. Section 2.7.2 treats beam loading specifically in the non-linear bubble regime, showing how an accelerator in this regime can be optimised by operating under the optimal loading condition.

2.7.1. LINEAR THEORY

The first theory for beam loading in laser plasma accelerators was developed by Katsouleas et al.[53]. In this idealised one-dimensional model it was found that there is an upper limit to the maximum amount of electrons which can be accelerated in a linear wake. As this number is reached, all the wakefield energy is absorbed by the bunch, giving a 100% beam-loading efficiency. For the case of an infinitesimally short,

unshaped bunch the maximum number of electrons is given by:

$$N_{\max} \cong 5 \times 10^5 \left(\frac{n_{p,1}}{n_{p,0}} \right) \sqrt{n_{p,0}} A, \tag{2.40}$$

where $n_{p,1}$ is the perturbed plasma density associated with the wave in cm^{-3}, which in linear theory does not deviate too strongly from the unperturbed plasma density ($n_{p,1}/n_{p,0} \ll 1$). The cross-sectional area of the wake A is given in cm^2.

Thus a linear wave with a 5 μm radius bunch in a plasma density of $10^{18} cm^{-3}$ and $n_1/n_0 \cong 0.2$ can accelerate up to 8×10^9 electrons, corresponding to 1.3 nC of charge. It should be noted that this model assumes rather idealised and physically unrealistic beams, which are ultra-short ($\ll c/\omega_p$), but gives a good insight in beam loading nonetheless. The maximum load given by equation (2.40), where all the energy from the wake is absorbed into the bunch, can only be achieved at the expense of 100% energy spread of the accelerated beam. This is due to the bunch front-running electron experiencing an unperturbed accelerating wakefield E_0, while in contrast, the trailing electron experience the superimposed field $E_f = E_0 + E_{beam}$. As the reduction of the accelerating field experienced by the trailing electron is linear to the number of particles in the loaded beam N, the fractional energy spread is given by

$$\frac{\Delta\gamma_{\max} - \Delta\gamma_{\min}}{\Delta\gamma_{\max}} = \frac{E_0 - E_f}{E_0} = \frac{N}{N_{\max}}, \tag{2.41}$$

where $\Delta\gamma_{\max}$ and $\Delta\gamma_{\min}$ refer to the maximum and minimum energy gain of a particle in the bunch. Equation 2.41 illustrates the trade-off between accelerated charge and energy spread of an accelerated bunch, with an increase in charge leading to an increase of energy spread due to the acceleration process.

In the case of an infinitesimally short bunch described above, the energy spread cannot be reduced without sacrificing the accelerated charge. However, in a scheme originally suggested by S. van der Meer in 1985[52], shaped beams with a finite length can be used to reduce the energy spread without greatly sacrificing the maximum bunch load. By choosing a triangular shaped bunch, with the peak density at the head of the bunch (ξ_0), the superposition of the laser wakefield and the bunch self-field becomes constant along the length of the bunch. In this case the peak bunch density, maximum bunch length, accelerating field and number of particles are[53]

$$\rho_b(\xi_0) = \rho_{b,\max} = -en_{p,1} \sin k_p\xi_0, \tag{2.42a}$$

$$l_{\max} = \left(\tan k_p\xi_0\right) k_p^{-1}, \tag{2.42b}$$

$$E_s = E_0 \cos k_p\xi_0, \tag{2.42c}$$

$$N = N_{\max} \frac{\sin^2 k_p\xi_0}{2 \cos k_p\xi_0}. \tag{2.42d}$$

Introducing a constant accelerating field E_s along the bunch, such triangular shaped bunches do not gain energy spread during their acceleration. However, as can be seen from equations (2.42c) & (2.42d) there is a trade-off between number of accelerated electrons and the acceleration gradient, with higher charges leading to a lower acceleration gradient and thus lower energy gain of the bunch. For example, a triangular bunch placed at $\xi_0 = \pi/3k_p$, with $N = 3N_{\max}/4$ particles over a length of $\sqrt{3}/k_p$, leads

to an accelerating gradient along the bunch with half of the peak wakefield amplitude ($E_s = E_0/2$).[53].

2.7.2. THREE-DIMENSIONAL NON-LINEAR CASE

In the non-linear case is becomes more difficult to describe beam-loading analytically. The first estimations as to how many electrons can be loaded into a three-dimensional non-linear bubble were part of the scaling theories presented in section 2.5.1. Lu et al.[38] estimated the number of particles N that can be loaded into a three-dimensional nonlinear wake to scale with the normalized volume of the plasma bubble or the square root of the laser power. The same scaling was also found by Gordienko and Pukhov[37] with a different coefficient:

From Lu et al.[38]:

$$N \simeq \frac{1.8}{k_0 r_e}\sqrt{\frac{P}{m_e c^3/r_e}}. \tag{2.43}$$

From Gordienko and Pukhov[37]

$$N \simeq \frac{8/15}{k_0 r_e}\sqrt{\frac{P}{m_e c^3/r_e}}. \tag{2.44}$$

Where $r_e = e^2/(m_e c^2)$ is the classical electron radius.

Although the coefficients in equation 2.43 & 2.44 differ from each other by over a factor three, they are not contradictory. Not taking bunch shape and energy spread into account one can choose to accelerate a relative small amount of electrons to high energies or a large charge to lower energies. Both these approaches do not specifically look for an optimal loaded wakefield such that the accelerating field in flattened and energy spread becomes minimised.

Optimal loading of the wakefield with shaped bunches in the bubble regime has recently been investigated in detail by Tzoufras et al.[54,55,114], continueing from the phenomenological theory presented in ref.[38]. Similar to in linear theory, an optimum trapezoidal bunch shape was found that efficiently converts energy available in the wake into kinetic energy of injected electrons while, in this ideal case, the accelerating field of the wakefield E_z becomes constant (E_s) along the bunch. The charge required to achieve this scales with[54]

$$Q_s\,[\mathrm{nC}]\,\frac{eE_s}{m_e c\omega_p} \simeq 0.047\sqrt{\frac{10^{16}}{n_p\,[\mathrm{cm}^{-3}]}}(k_p R_b)^4, \tag{2.45}$$

where c is the speed of light, Q_s is the total loaded charge, n_p and $\omega_p \sim \sqrt{n_p}$ are the density and frequency of the plasma with the plasma wavenumber k_p. From equations (2.25) and (2.26), a matched laser condition $k_p R_b$ amounts to approximately $2\sqrt{a_0}$.

Equation (2.45) represents the optimal loaded case where there is a balance between the amount of loaded charge and the accelerating field and is illustrated in figure 2.8. The self-field of the bunch balances with the wakefield such that the resulting field

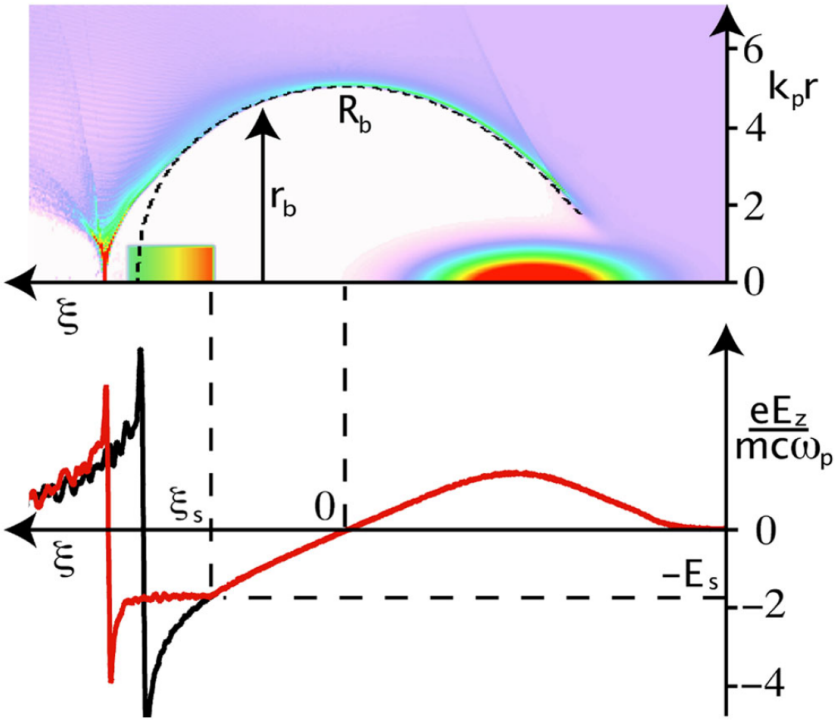

Figure 2.8.: **Optimum loading in the non-linear bubble regime.** The top half of the figure shows the electron density obtained from a PIC simulation. In this case the wakefield is driven by an electron driver and a second bunch is loaded in the wake under the optimal loading condition according to equation (2.45). The bubble in this loaded case is elongated compared to bubble boundary in the unloaded case indicated by the dashed black line. The bottom of the figure shows how the wakefield E_z becomes flat in the optimal loaded case (red line) compared to the unloaded case (black line). Figure from Tzoufras et al.[54].

becomes constant (E_s) along the length of the bunch. Thus, all electrons in the bunch experience an identical accelerating field strength and no energy spread is gained during the acceleration process.

In praxis, a complicated bunch shaping injection scheme is required in order to inject trapezoidal flat-top bunches for which equation (2.45) is valid. However, PIC simulations[55] confirm that this theory also approximately holds true for Gaussian shaped bunches thus enabling this theory to be tested experimentally without bunch shaping required.

Equation (2.45) shows the dependency on plasma density and bubble radius. The matched spot size condition however depends on the normalised laser parameter. Thus the injected charge required to reach the optimal loading condition depends on the driver laser power.

Taken that the wakefield is driven in the nonlinear bubble or blow-out regime under matched spot size conditions the following holds true from equation (2.25) and (2.26):

$$k_p R_b \simeq 2\sqrt{a_0}. \tag{2.46}$$

and from ref.[38]

$$a_0 \simeq 2\left(P/P_c\right)^{(1/3)}, \tag{2.47}$$

where P_c is the critical power for relativistic self-guiding according to equation (2.14).

Choosing $E_s = E_{max}$, equation (2.27) can be rewritten to

$$\frac{eE_s}{m_e c \omega_p} = \frac{k_p R_b}{2} \simeq \sqrt{a_0}. \tag{2.48}$$

From equation 2.48, 2.47 and $\omega_p \propto \sqrt{n_p}$ follows $E_s \propto n_p^{2/3}$.

By inserting equations (2.48), (2.47) and $P_c = \left(\omega/\omega_p\right)^2$ from (2.14) into equation 2.45 follows:[3]

$$Q_s[\mathrm{nC}] \simeq 1.504 \frac{1}{\omega_0} \sqrt{\frac{2 \cdot 10^{22} e^2}{17 m_e \epsilon}} \sqrt{P[\mathrm{GW}]} \tag{2.49}$$

Equation (2.49) gives a direct measure as to how much charge must be injected into a laser-plasma accelerator operating in the non-linear bubble regime in order for it to operate in the optimal loading condition. It also shows that the optimal loaded charge depends on the laser peak power P as $Q_s \propto \sqrt{P}$ but is independent from the plasma density. However, the accelerating field E_s and thus the achievable electron energy follows a $n_p^{2/3}$ dependency.

[3] A step by step derivation can be found in appendix C

3. SETUP & TECHNICAL DETAILS

This chapter covers the technical details related to the implementation of the LPA and related experiments presented in this thesis. A short introduction of the experimental target area at the ELBE centre for High-Power Radiation Sources and the design of the experimental chamber is given in section 3.1. Next, the experimental LPA setup is presented in section 3.2. This section gives a general overview of the LPA, with individual aspects of this setup covered in more detail in following sections. Section 3.3 gives a comprehensive description of the DRACO laser system, which is providing the driver laser pulse. The gas medium, which is provided by a gas target, is discussed in detail in section 3.4. Finally, in section 3.5 the electron spectrometer is presented.

3.1. EXPERIMENTAL TARGET AREA

The experimental target area for the work presented in this thesis was commissioned as part of the PhD project. It is located within the ELBE centre for High-Power Radiation Sources which consists of the conventional electron accelerator based radiation source ELBE (**E**lectron **L**inac for beams with high **B**rilliance and low **E**mittance[115]) and two high-power laser systems: the two beam 150 terawatt / 1 petawatt Ti:Sapphire laser DRACO (Dresden laser acceleration source, see section 3.3) and the diode-pumped petawatt laser PEnELOPE (**P**etawatt, **En**ergy-**E**fficient **L**aser for **O**ptical **P**lasma **E**xperiments[116]).

The target area, commissioned in 2013 following an upgrade of the ELBE centre, has the unique aspect of being located such that all above-mentioned radiation sources can be combined in this area as can be seen in figure 3.1. In this PhD project, a dual-use target vacuum chamber has been set up that enables operation of both the ELBE conventional electron source, the DRACO 150 terawatt laser beam or a combination of both. The infrastructure for the petawatt DRACO arm has been prepared fur future implementation. The target chamber has been designed to host two separate scientific setups to be developed in parallel. It hosts both the laser plasma electron accelerator presented in this thesis and associated diagnostic and secondary sources, as well as the previously developed PHOENIX (**Ph**oton **E**lectron collider for **N**arrow bandwidth **I**ntense **X**-rays[9,10,117]) light source, which is based on Thomson backscattering of the the DRACO laser pulse from ELBE relativistic electrons. The PHOENIX source has been

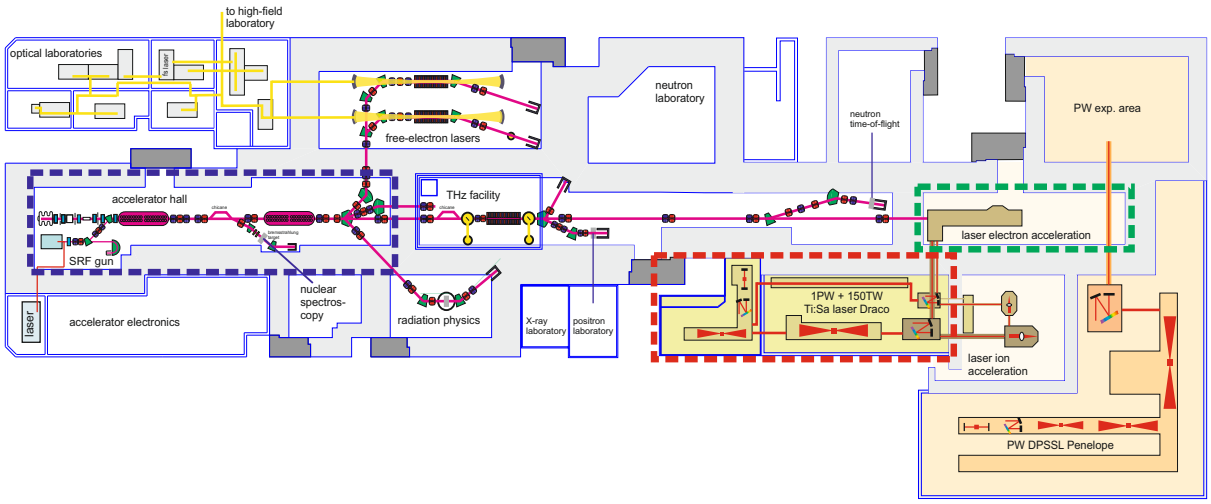

Figure 3.1.: **Layout of the ELBE center for High-Power Radiation Sources.** The target area is indicated by the dashed green box. The DRACO laser system is indicated by the dashed red box and the conventional electron accelerator by the dashed blue box.

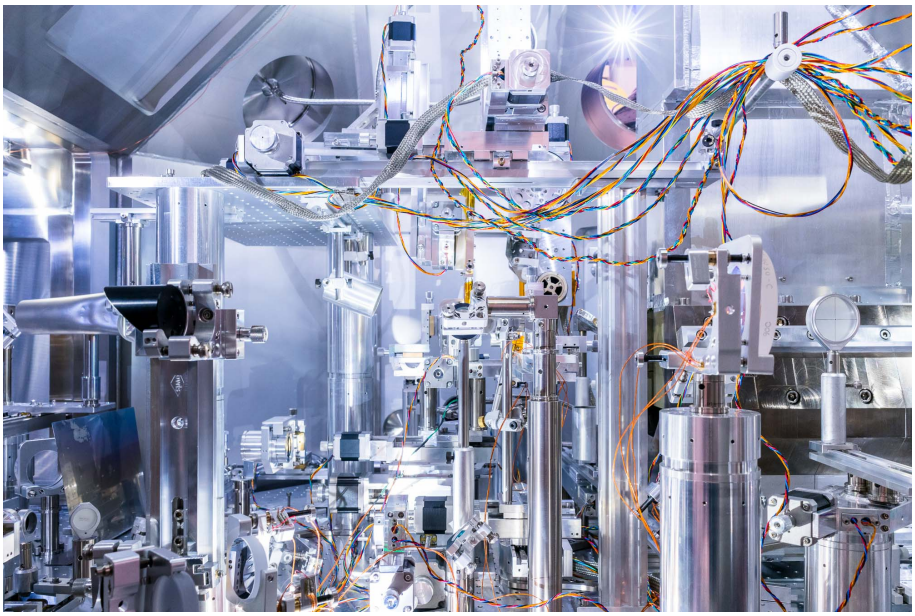

Figure 3.2.: **Target area inside the experimental vacuum chamber.** The shown field of view in the setup is indicated in figure 3.3. The LPA gas jet is situated roughly in the centre, hidden from view by other components. The laser propagates from the left side. Generated electrons are diagnosed in the dipole spectrometer visible on the right. The Thomson backscattering source is not visible on this photograph. Foto: HZDR/André Wirsig.

further developed in a parallel project aimed at using inverse Compton scattering as a tool for advanced diagnostic for electron beams from laser plasma acceleration[2].

The chamber is a 5.6 metre long modular design, intended to offer the highest possible flexibility in element placement and accessibility. The modular design offers the possibility for future extension if required. In order to decouple pump vibrations and chamber deformation due to pressure forces under vacuum operation, an optical breadboard is placed inside the vacuum chamber decoupled from the chamber itself.

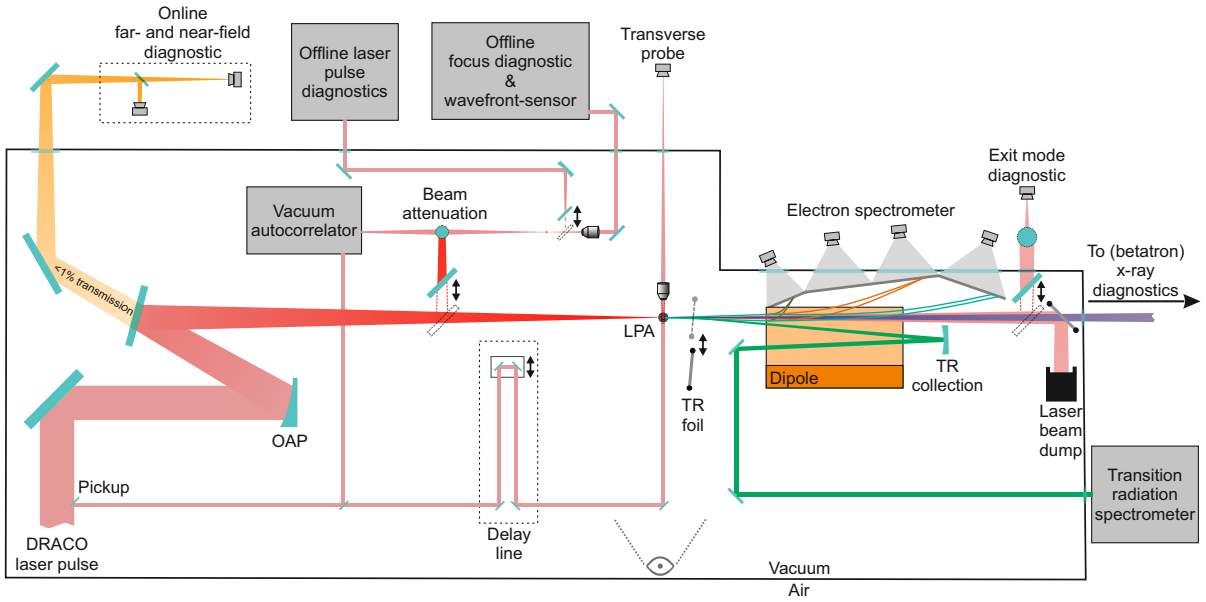

Figure 3.3.: **Schematic representation of the LPA setup.** The eye symbol roughly indicates the field-of-view from figure 3.2

The breadboard is a high-flatness aluminium plate with a 25 millimetre thread grid, having a 100 millimetre thickness in order to provide a rigid platform which does not deform under placement or movement of heavy elements. Five elements are rigidly connected, providing complete freedom of element placement throughout the entire chamber. The vacuum is maintained by three turbomolecular pumps which are able to create a vacuum in the low 10^{-6} mbar range under experimental conditions. Figure 3.2 an partial inside view of the experiment chamber.

3.2. EXPERIMENTAL SETUP OF THE LPA

Figure 3.3 shows a schematic representation of the LPA setup and associated diagnostics located in the target chamber discussed in section 3.1. The Thomson backscattering setup with the ELBE accelerator is not shown here.

The DRACO laser pulse (see section 3.3) is coupled into the experimental chamber using a vacuum transport line from the DRACO vacuum compressor. Using an off-axis parabola (OAP) the laser beam is focussed roughly 1.5 mm above the gas-jet target which provides the acceleration medium. This target is discussed in detail in section 3.4.4. The OAP is mounted such that it can easily be interchanged for several focal lengths. For the experiments described in this thesis an f/20 OAP is used.

Before experiments, a movable mirror is placed into the beam's path to redirect it to several offline diagnostics. For this purpose, the beam is attenuated by reflection over several high surface quality uncoated wedges. The focus created by the OAP is imaged using a high quality objective on a CCD for focal spot optimisation (see section 4.1.1) or on a wave-front sensor (PHASICS SID4) for wave-front optimisation in a closed loop with a deformable mirror located in the DRACO vacuum compressor.

Another movable mirror allows the beam to be collimated and coupled out for further

offline diagnostic. A self-referenced spectral interferometer (WIZZLER-Fastlite) for single shot spectral phase and intensity measurements can be used in close loop with an acousto-optic programmable dispersive filter (DAZZLER-fastlite) for spectral phase correction as discussed in section 4.1.2. Other diagnostics which can be positioned here for cross-reference are a spectral-phase interferometer (SPIDER-A.P.E.) or a scanning third-order cross-correlator (SEQUOIA, Amplitude technologies).

A single shot second order vacuum autocorrelator can be used both offline as well as online, using a pickup, to monitor the laser bunch length stability during the LPA experiments. The laser beam stability is furthermore monitored during experiment in the far-field and near-field using a low transmission fraction of a mirror positioned between the OAP and the LPA.

The acceleration process is transversally probed using an objective imaging the accelerator onto a camera. A probe beam, created by picking part of the main laser beam, acts as a back-lighter. The laser pulse length defines the temporal resolution while a delay line gives the possibility to tune probe timing in respect to the main laser pulse.

The exit mode diagnostic, downstream of the gas target, images the target. During LPA operation, the laser exit mode after driving the accelerator can be diagnosed. Before experiment it allows for diagnoses and precise positioning of the laser focus onto the gas target.

Alternatively, the exit mode diagnostic mirror can be moved from the acceleration axis. This allows for diagnosis of x-rays, either generated by betatron radiation or by Thomson backscattering. X-ray diagnostics can be positioned up to twelve metres downstream from the accelerator exit depending on requirements.

A dielectric foil can be positioned directly behind the LPA, either for the generation of transition radiation or to act as a plasma mirror to reflect the driver laser pulse. The reflected laser pulse can interact with the electron bunch for x-ray generation by Thomson backscattering. The transition radiation can be used for bunch length determination as is described in section 4.6.

The accelerated electron bunch is diagnosed for charge and energy distribution in a permanent dipole magnet spectrometer. This spectrometer, with a range from a few MeV up to 550 MeV is discussed in more detail in section 3.5.

3.3. DRACO LASER SYSTEM

In order to drive a LPA in the bubble regime, a high intensity ultrashort laser driver is required. As discussed in section 2.5, an a_0 of at least two is needed to enter this regime, while at the same time the laser pulse should be short enough to fit within the bubble-shaped cavity, i.e. $c\tau < R_b$.

In order to reach these conditions, the double chirped pulse amplification (CPA)[16,17] DRACO high intensity laser system is used for experiments presented in this thesis. CPA is a technique that enables amplification of laser pulses to very high powers by temporally stretching pulses prior to amplification. This reduces the peak power during the amplification process, avoiding non-linear effects in and damage to optical elements and amplifying crystals while the laser system can be built relatively compact. Only after amplification the laser pulse is temporally and spatially compressed to reach the

desired high peak intensities required for LWFA.

Recently upgraded, the DRACO system is a dual beam system providing full Petawatt (30 J in 30 fs) and 150 TW (4.5 J in 30 fs) after compression with optimised temporal pulse contrast and high beam quality.[4] The system is based on the commercially available PULSAR laser system by *Amplitude Technologies* and uses titanium doped sapphire (Ti:Sa) crystals as gain medium at a central wavelength of 800 nm and a pulse bandwidth of up to 80 nm. The optical properties, broad amplification bandwidth and high thermal damage threshold of Ti:sapphire makes this material especially suitable for the amplification of ultra-short, ultra-high-intensity laser pulses.

A schematic representation of the DRACO laser system is shown in figure 3.4. The laser chain starts at a commercial *Femtolasers* oscillator which delivers pulses at 800 nm central wavelength and a spectral width above 100 nm resulting in 10 fs pulses at the nanojoule level with a 78 MHz repetition rate. A Pockels cell (PC) pulse picker reduces the repetition to 10 Hz for seeding into the laser system. A booster amplifier increases the pulse energy to the microjoule level before the pulses fed into the first CPA stage. Upon entry of the CPA1 stage, pulses are stretched in an all-reflective stretcher to a pulse duration of about 500 ps. The increase of pulse duration ensures that the temporal peak power stays below the damage threshold of subsequent optics during the amplification process. An acousto-optic programmable dispersive filter (Dazzler-*Fastlite*) is implemented in the pulse stretching unit to allow for fine-tuning of the spectral phase for the purpose of pulse compression optimisation at the end of the CPA stage.

The stretched pulses are then amplified in a regenerative amplifier to about 0.5 mJ before being amplified to 25 mJ in a multi-pass amplifier. An acousto-optic programmable gain filter (Mazzler-*Fastlite*) in the regenerative amplifier allows for fine control of the spectral gain by reducing the transmission in high-gain spectral regions.

The pulse is subsequently compressed in an air compressor to a pulse length of 30 fs. This in-between compression is performed to gain sufficient peak-intensity for cross-polarised wave (XPW) pulse cleaning[118], suppressing pre- and post-pulses and thus optimising temporal contrast.

The low efficiency of the XPW pulse cleaning process reduces the energy per pulse to about 0.3 mJ. These pulses are coupled into the CPA2 stage of the laser system, which parallel to the CPA1 stage amplifies pulses by subsequently passing through a stretcher (∼1 µs), regenerative amplifier and a multi-pass amplifier. Additionally the pulse energy is further increased by two further multi-pass amplifiers to 100 mJ and finally 1.5 J. The laser system up to this point constitutes the front-end. Here the laser system splits into its two arms, towards the 40 J cryostat amplifier for the petawatt arm and towards the 6 J cryostat amplifier for the 150 TW arm. Both arms can be operated either individually or in parallel. As both arms are seeded by the same front-end, synchronisation between both arms is inherent. In this thesis only the 150 TW arm is used.

The last multi-pass is only seeded on demand by a Pockels cell pulse picker, allowing for operation from single shot to continuous 10-Hz operation. To handle with various repetition rate and the high thermal load, the last multi-pass' amplifier crystal is cryogenically cooled to avoid thermal lensing.

After final amplification the pulses are expanded to the final beam size of 100 mm and transported to the compressor where the pulses are compressed to a duration of 30 fs. This final compression and subsequent beam transport occurs in vacuum, as the

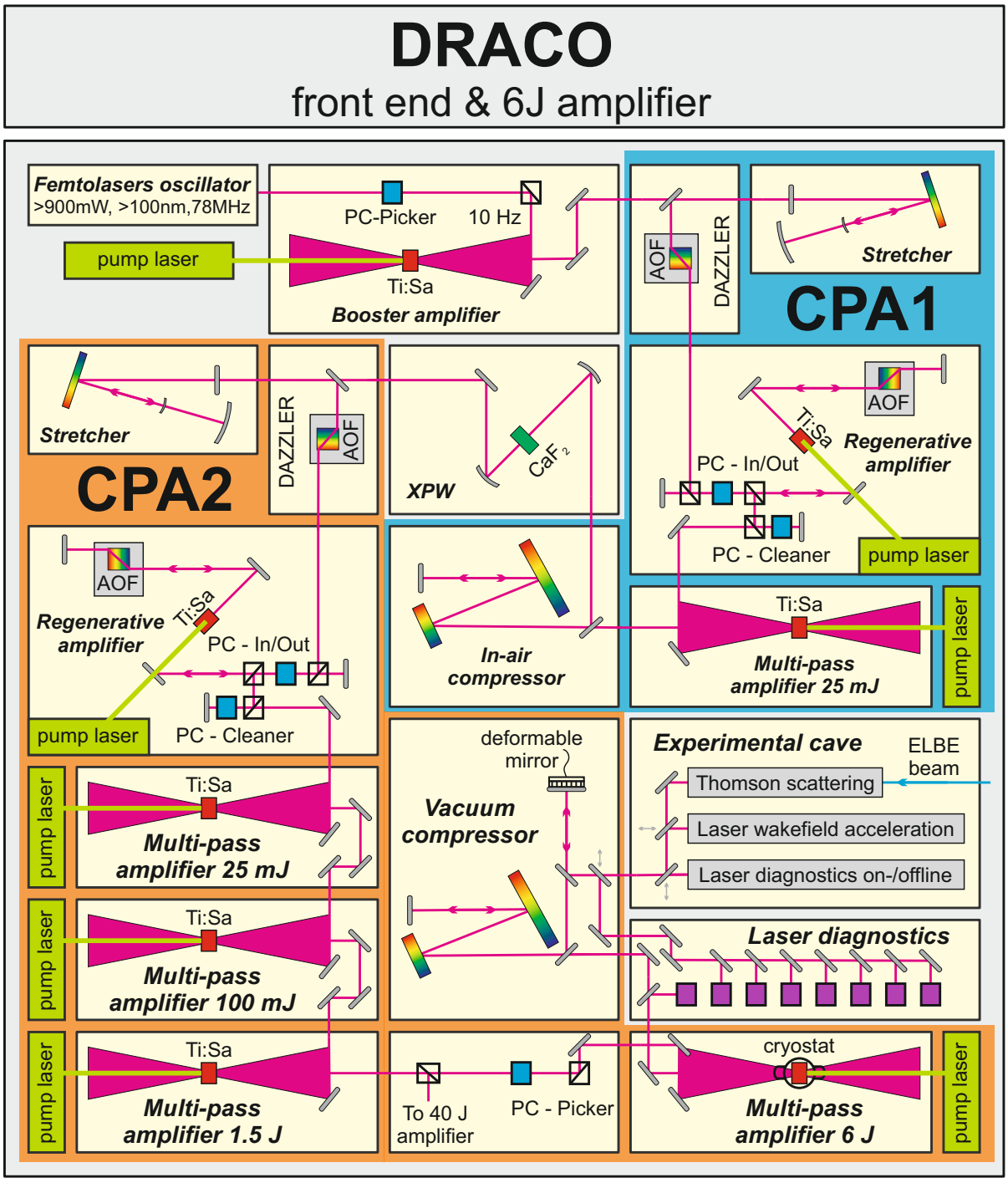

Figure 3.4.: Schematic of the DRACO laser system front-end and 150 TW arm.

laser field at this point becomes high enough to cause ionisation in air and subsequent filamentation[119]. A deformable mirror allows for wavefront optimisation in a closed loop with a wavefront sensor (*PHASICS* SID4) situated at the experimental cave. A beam transport switching system allows for transport of the beam either to the ion acceleration area or to the electron acceleration area as shown in figure 3.1.

3.4. LPA TARGETS & CHARACTERISATION

The medium in which the laser interacts with the plasma is one of the most essential aspects in a laser-plasma accelerator. Exact design, tailoring, control and diagnostic of a target which provides such a plasma medium is not straightforward and bound to many requirements. The laser plasma interaction with an ultra-short laser pulse which intensity is sufficient to cause highly non-linear effects is highly sensitive to plasma density and profile.

The laser being focussed down to a only a few tens of microns spot size, intensities of above 10^{18} W/cm^2 are reached and any interaction with matter causes strong temporal and spatial modulation of the laser pulse. Such interaction occur in the plasma medium itself and is required to have laser wakefield acceleration at all, however any such interaction before the target is reached is undesired. Therefore laser beam propagation occurs in a vacuum vessel with a pressure of generally below 10^{-5} mbar. This is in sharp contrast to the plasma densities required for the accelerator, which are generally in the range of 10^{17} to 10^{19} electrons cm^{-3}. A target provider must therefore be able to deliver a well-defined plasma distribution at an exact position at nearly atmospheric pressure without compromising the vacuum condition of the direct surrounding.

Main providers in experiments that are capable of fulfilling these requirements are discharge capillaries, gas cells and gas-jets. Discharge capillaries are the only target providers that directly deliver a pre-ionised plasma medium by ionising a gas with a high-voltage discharge shortly before the driver laser arrives. If designed appropriately, the pre-ionised channel can have a transversal density gradient guiding the laser pulse over many times the Rayleigh length[64]. Such a pre-ionised channel has the advantage that the guided laser spot size is decoupled from the laser intensity and that no non-linear effect is required for self-focussing. Thus, it enables to operate a LPA in a stable (quasi)linear regime over many times the Rayleigh length. However, the technical complexity of the discharge makes discharge capillaries challenging to operate.

Gas cells and jets are well-established target providers which are technically less challenging and easy to operate. In contrast to capillary discharge targets, they only deliver a gas distribution and subsequently rely on ionisation by the main laser pulse itself to create a plasma. With no external guiding present in gas cells and jets, the driving laser has to be of a high enough intensity to reach the self-focussing regime (see section 2.3) to stay confined beyond the Rayleigh length. In effect, the laser spot size is coupled with the plasma density and operation is the non-linear regime is required. Although this regime gives less tunability and is potentially less stable than a (quasi)linear regime, it does have the advantage of high acceleration gradients and a bubble shaped accelerating structure which is able to confine and accelerate high charge beam over a large distance.

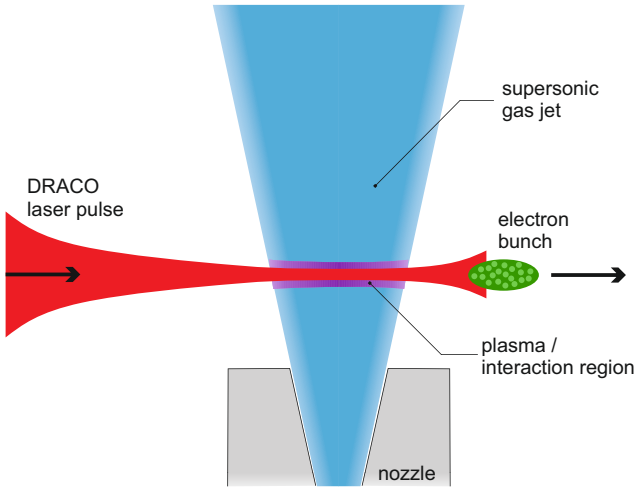

Figure 3.5.: **Schematic representation of a gas-jet LPA.** The laser is positioned to interact with the gas-jet above the nozzle, typically ∼1 mm. A supersonic gas-jet is required to ensure a sharp density transition even further above the nozzle. The open design of gas jet targets allows for easy diagnostic of the acceleration process.

Gas cells and capillaries generally have small entrance and exit apertures in order to constrain the gas medium, to create the required vacuum/gas border and to facilitate the discharge in the case of discharge capillaries. This makes them sensitive to laser misalignment and shot-to-shot pointing fluctuations. Gas-jets create a sharp vacuum/gas border by allowing a super-sonic expansion of gas into the vacuum. The open design of gas jets allows for easy diagnostics of the acceleration process. A schematic representation of a laser wakefield accelerator using a gas-jet as target provider is shown in figure 3.5. These advantages have lead to gas-jets becoming the main acceleration media provider. Generally, only when a low plasma density is required, as needed for longer interaction lengths, gas cells are used instead. The LPA presented in this thesis uses a gas jet target provider.

Although nozzle design and simulation can provide a good prediction on the gas jet density distribution it will provide, imperfections which can arise from alignment errors, production failures or degradation during experiment due to expansion shocks are not taken into account. Therefore an experimental characterisation of gas jets is required before usage in acceleration experiments.

In this section the characterisation of gas-jet targets is presented. Generally gas-jet targets for LPAs are operated at helium gas for its low ionisation threshold (see section 2.1). However, helium has a very low refractive index, making characterisation by interferometric phase shift measurement challenging. In order to resolve the phase shifts induced by a helium gas jet, an ultra sensitive and stable interferometric setup is required. The setup used for target characterisation, including its working principles is introduced in section 3.4.1. The need for a tomographic analysis of the gas-jets, instead of relying on a reconstruction protocol assuming circular symmetry, is demonstrated in section 3.4.2. Often gas-jet targets are operated with a higher refractive gase like argon or nitrogen for characterisation[120–122], but as will be shown in section 3.4.3 this does

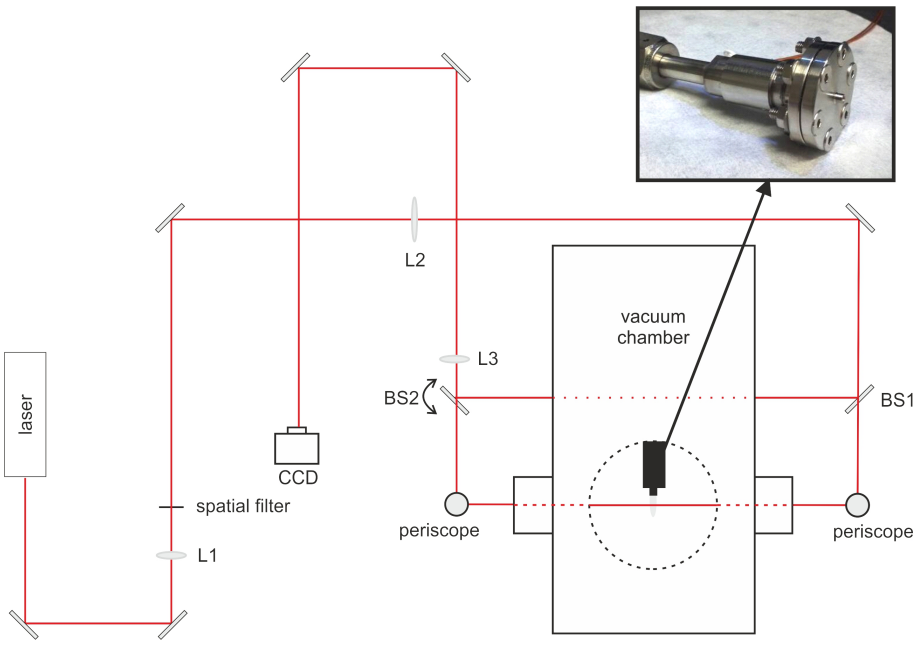

Figure 3.6.: **Schematic representation of the gas-jet interferometry setup.** Lenses L1 & L2 function as a beam expander. L3 images the target plane onto the CCD. The inset shows a 0.75 mm cylindrical nozzle. For tomography purposes the gas-jet target can be rotated to take measurements under multiple angles.

not necessarily represent the exact gas density profile of the same nozzle operated with helium gas. Finally, the specific gas jet target used for operation of the LPA as presented in chapter 4 & 5 is introduced in section 3.4.4.

3.4.1. INTERFEROMETRIC ANALYSIS OF GAS-JET TARGETS

A Mach-Zehnder type interferometer is used to characterise the gas-jet target. By positioning the gas jet in the signal arm of the interferometer, a gas density dependent optical path length difference is induced between the probe arm and the reference arm. This results in a phase shift in the interferogram from which the original gas density profile can be deducted. A schematic of the setup is shown in figure 3.6.

The interferometer uses a 18 mW continuous wave HeNe laser at 632.8 nm (Linos G040-814-00 with PS-3170) as a lightsource. Depending on the nozzle size, the laser beam is expanded to illuminate the entire gas-jet by lenses L1 and L2 in a telescope configuration. In this telescope the beam is spatially filtered using a pinhole to acquire a homogeneous beam. Both interferometer arms have approximately the same length to stay within the coherence length of the laser. 50:50 beamsplitters (BS1 & BS2) are used to achieve the highest interferometric fringe contrast. The arms overlap at a CCD camera (PCO.pixelfy) which is positioned at the lens L3 image plane of the gas-jet. Temporal resolution is achieved by a short (µs-range) camera exposure. A small angle α introduced at BS2 results in a fixed sinusoidal interference pattern along the x-direction according to[123,124]

$$I = 2I_0\left[1 + \cos\left(kx\sin\left(\alpha\right)\right)\right], \tag{3.1}$$

where $k = (2\pi)/\lambda_l$ is the laser wavenumber. This constant pattern acts as the carrier pattern, which is necessary as a carrier for the phase-shift that the gas-jet induces in the signal arm.

The gas-jet in the signal arm introduces an optical path length difference (Δ_{OPL}), which adds to the intensity function which is imaged on the CCD:

$$I = 2I_0 \left(1 + \cos\left(kx\sin(\alpha) + \frac{2\pi\Delta_{OPL}}{\lambda_L}\right)\right) \quad \text{with} \quad \Delta_{OPL} = \int_C \Delta n(s)\,\mathrm{d}s. \tag{3.2}$$

The cosine term contains both the above-mentioned carrier contribution as well as the contribution from the gas-jet induced phase shift. The optical path length difference depends on the density distribution of the gas-jet and its associated refractive index change $\Delta n(s)$ along a path C.

SETUP STABILITY

Besides the phase shift introduced by the gas-jet, disturbances like air flow, irregularities in optics and scattered laser-light add unwanted extra phase disturbances, reducing the setup's ability to detect small phase shifts. Including these extra influences and rewriting equation (3.2) gives

$$I(x, y) = I_A(x, y) + I_B(x, y)\cos\left[\varphi_c(x, y) + \varphi_s(x, y) + \varphi_d(x, y)\right]. \tag{3.3}$$

The CCD-chip defines the x,y-plane. I_A is the background and I_B the local amplitude of the fringe function, which may vary in the case of a non-uniform illumination. φ_c is the carrier phase and φ_s is the signal phase, they correspond to the first and second part within the cosine of equation (3.2) respectively. φ_d contains all disturbances that do not come from the static fringe pattern or the gas jet. The setup has been optimised to keep φ_d as low as possible. This is achieved by using active vibration isolation of the optical table, encasement to minimise air-turbulences and dust scattering and placing optics away from the imaging plane such that unwanted scattering from optics defects do not image to the camera plane.

Figure 3.7 shows a noise map of the setup. This map is constructed by taking measurements under experimental conditions but without a gas-jet present. Ideally, every single measurement should render the exact same phase map. Small fluctuations in setup stability introduce phase disturbances φ_d for every shot. The shot-to-shot standard deviation is a measure for the noise in the setup. Overall, the average standard deviation is 3.9×10^{-3} rad, well below the shift expected for the gas-jet targets.

DATA PROCESSING

After acquisition of gas-jet induced phase shift images, further processing of the data is required to reconstruct the gas density profile. This is done in two steps: Phase retrieval, followed by gas density reconstruction, either by Abel-inversion or by tomographic reconstruction. This process, including intermediate steps, is shown in the flowchart in figure 3.8.

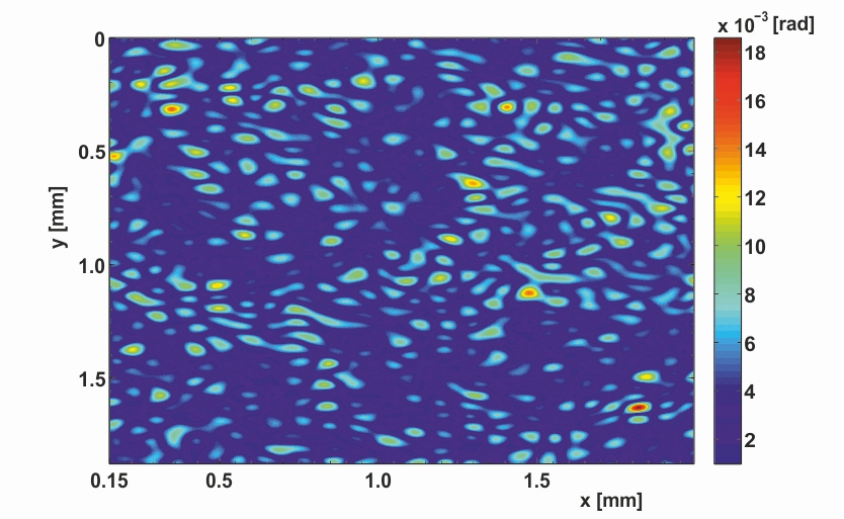

Figure 3.7.: **Standard deviation map over 30 measurements.** The phase map was constructed when no jet was present and shows the stability of the setup.

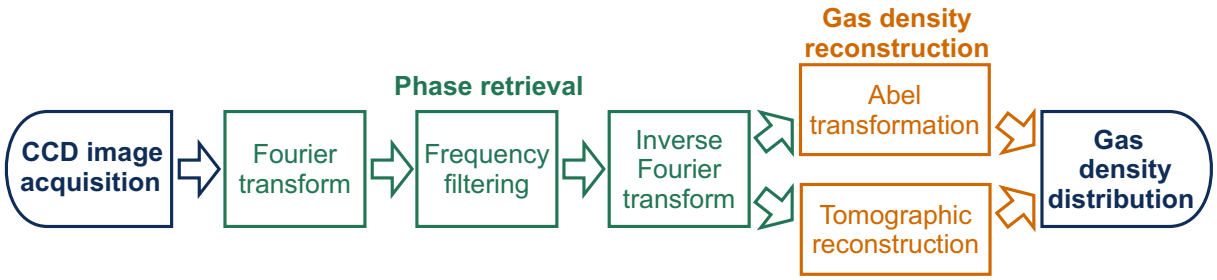

Figure 3.8.: **Flowchart showing data processing for gas density profile reconstruction.**

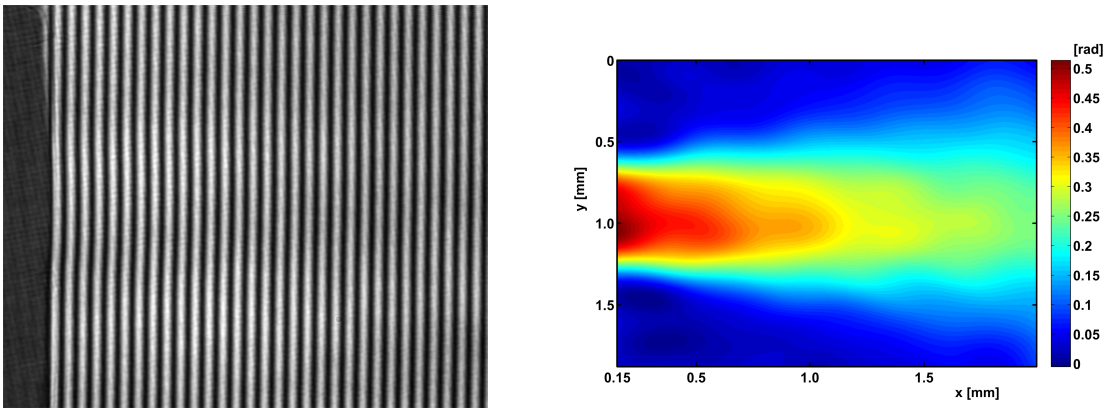

(a) Interferogram as acquired by the camera. The nozzle can be partly seen on the left.

(b) Induced phase shift. Acquired over 25 averages

Figure 3.9.: **Interferogram and corresponding phase shift.** Induced by a helium gas-jet produced by a 0.75 mm Mach 4.8 de Laval nozzle with a backing pressure of 70.5 bar.

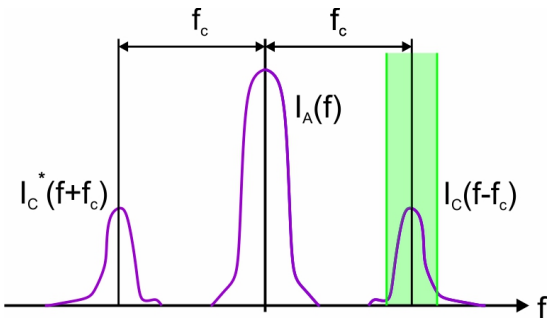

Figure 3.10.: **Illustrative Fourier spectrum with separated contributions.** The green area represents a possible filter range.

Phase retrieval A typical interferogram can be seen in figure 3.9(a). This image contains all the information as expressed in equation (3.3). Since only the phase shift φ_s is of interest, data-processing is required to extract this information. Using the Fourier-transform method[125] the image is transformed into the Fourier domain to filter the phase information. Rewriting equation (3.3) in the frequency domain gives:

$$\hat{I}(f_x, f_y) = \underbrace{\hat{I}_A(f_x, f_y)}_{\text{carrier}} + \underbrace{\hat{I}_C(f_x - f_{c,x}, f_y - f_{c,y})}_{\text{signal + disturbance}} + \underbrace{\hat{I}_C^*(f_x + f_{c,x}, f_y + f_{c,y})}_{\text{signal* + disturbance*}}, \tag{3.4}$$

where the hat denotes the Fourier transform and the asterisk superscript denotes the complex conjugate. At this stage a frequency filter is applied to the Fourier transform. Only the $\hat{I}_C(f_x - f_{c,x}, f_y - f_{c,y})$ part is selected. A two-dimensional representation of this process is shown in figure 3.10. By defining the range of the filter, noise components outside this range are filtered out.

Performing a back Fourier transformation over the selected filter gives an intensity distribution I_c with the background variation contained in the real part and the phase in the imaginary part. The phase information is extracted by:

$$\tan^{-1} \frac{\Im\left[I_C(x, y)\right]}{\Re\left[I_C(x, y)\right]} = (\varphi_c + \varphi_s + \varphi_d)(x, y). \tag{3.5}$$

To remove the carrier phase component the same process is also performed on a reference shot where no gas-jet is present, which renders an interferogram which does not contain a φ_s term. By subtracting the reference shot phase from the signal shot phase, the φ_c term is removed from equation (3.5). Figure 3.9(b) shows the resulting phase map corresponding to the interferogram from figure 3.9(a) acquired according to this method.

Gas density reconstruction In experiment, the signal laser beam travels through the three-dimensional (3-D) gas jet and projects the gas-density information on the two-dimensional (2-D) CCD-chip. To obtain a 3-D gas-jet density map either an Abel-inversion or a tomographic back-projection must be performed.

For axisymmetrical gas-jets, Abel inversion can be used. In this case, the gasjet is reconstructed under assumption of cylindrical symmetry from a phase shift measure-

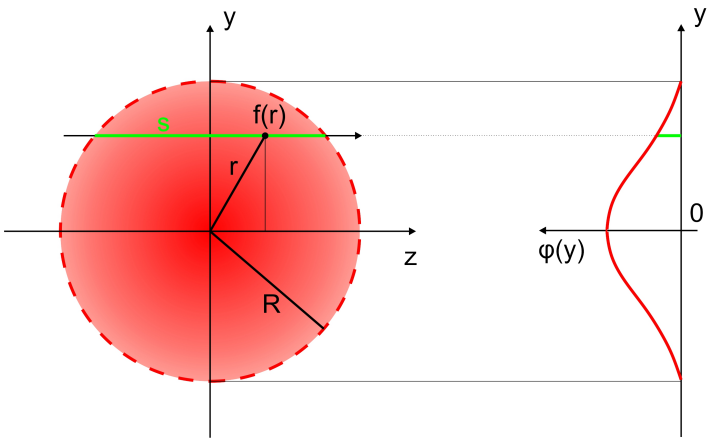

Figure 3.11.: **Abel Transformation.**

ment taken under a single angle. Figure 3.11 shows the Abel transformation from a 3-D gas-jet to a 2-D projection. The measured phase shift at a certain height x above the nozzle $\varphi(y)$ is the integral according to equation (3.2) along the optical path s. Via the inverse Abel transform $\varphi(y)$ can be translated into $f(r)$, which is a function related to the gas density at a distance r from the nozzle centre. The analytical solution of the inverse Abel transform is[126]:

$$f(r) = -\frac{1}{\pi}\int_r^R \frac{\mathrm{d}\varphi(y)}{\mathrm{d}y}\frac{\mathrm{d}y}{\sqrt{r^2-y^2}}. \tag{3.6}$$

Since a full analytical solution is not possible for data-analysis a numerical Abel inversion is used. Results presented here are processed with the Interferometrical Data Evaluation Algorithms (IDEA) software developed by the Graz University of Technology using the f-interpolation method[127].

For gas-jets that are not axisymmetric or in order to be able to resolve non-axisymmetric nozzle defects, a tomographic reconstruction algorithm must be used. Here, different 2-D projections are taken under multiple angles, after which the 3-D gas-jet can be reconstructed using the Fourier slice theorem:[128]

$$f(x,y) = \int_0^{\pi}\int_{-\infty}^{+\infty} \hat{I}(k_r,\theta)|k_r| e^{i2\pi k_r x\cos(\theta)+y\sin(\theta)}\mathrm{d}k_r\mathrm{d}\theta, \tag{3.7}$$

with $\hat{I}(k_r,\theta)$ the Fourier transform of the measured projection in polar coordinates. $|k_r|$ is the filter that weights the spatial frequency contributions in the projection. Using this filter prevents blurring of the reconstructed image. In the analysis presented here a Hann-filter[129] is used.

The function f, obtained either by Abel inversion or tomography, is related to the refractive index of the gas by:

$$f(r) = \frac{2\pi}{\lambda}\left(\eta(r)-1\right). \tag{3.8}$$

Table 3.1.: **Polarisability and the index of refraction of several gases** at 273K, p = 1 atm. and a probe wavelength of λ = 633 nm. Values of η from[133]. Values for α according to eq. (3.9).

	$\eta - 1(10^{-5})$	$\alpha(10^{-41}$ F m$^2)$
He	3.492	2.300
Ar	28.12	18.52
H_2	13.88	9.143
N_2	29.79	19.62

The index of refraction η is dependent on the gas density n and the laser wavelength λ according to the Lorentz-Lorenz equation[130–132].

$$\frac{\eta(\lambda)^2 - 1}{\eta(\lambda)^2 + 2} = \frac{n\alpha(\lambda)}{3\epsilon_0}, \tag{3.9}$$

with α the polarizability of the gas and ϵ_0 the permittivity of free space. For $\eta \approx 1$, the gas density can be approximated by

$$n \approx \frac{2\epsilon_0}{\alpha(\lambda)} \left(\eta(\lambda) - 1\right). \tag{3.10}$$

Table 3.1 gives values for η and α for various gases. With these values and equation (3.10) the gas density can be calculated from the Abel transformed or tomographic reconstructed data.

A helium jet of 0.75 mm with a gas density of 7×10^{18} cm^{-3} gives an expected phase shift of only 6×10^{-2} radians. The same jet operated with the same density argon or nitrogen will give a considerably larger phase shift of around 0.5 radians. Taking the stability (section 3.4.1) into account, this setup is capable to perform direct measurements on helium gas-jets.

3.4.2. COMPARISON BETWEEN ABEL INVERSION AND TOMOGRAPHY

The assumption of axisymmetry in the Abel inversion simplifies the analysis protocol; less data has to be acquired and the data analysis is simplified. Therefore Abel inversion is often preferred over tomography and a valid approach in case of a real axi-symmetric jet. However, if a nozzle defect is present Abel inversion is often not able to resolve this, as an non-axi-symmetric phase disturbance is rotationally averaged as follows from equation (3.6). To demonstrate this, this section presents a comparison between Abel inversion and tomographic analysis of the same jet.

For this comparison a conical Mach 4.8 de Laval nozzle[134] is used. The nozzle has a throat of 0.25 mm and a nozzle exit diameter of 0.75 mm. This nozzle is designed to provide a flat-top density profile with steep gradients and has been analysed as such[135,136]. After extensive use in LWFA experiments this nozzle has degraded and a defect was suspected. Figure 3.12 shows analysis of this nozzle by both methods. Both methods show that the nozzle has degraded to the point where it does not have a steep-gradient flat-top profile. But since the Abel inversion method assumes

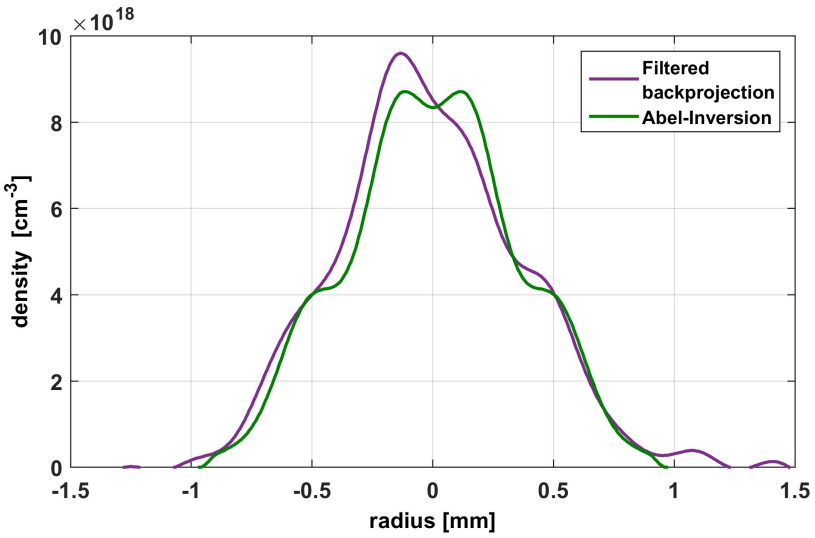

Figure 3.12.: **Comparison between Abel-inversion and tomography**. Results from a degraded conical Mach 4.8 de Laval nozzle at 700 µm above the nozzle exit. Argon, 20 bar backing pressure. Line-out over the nozzle centre for the tomography, Abel-inversion relies on centro-symmetry.

axisymmetry, this method is not able to detect the asymmetry in the density profile that clearly shows up in the tomographic analysis.

A tomographic analysis is thus required in order to resolve certain nozzle defects. Nonetheless, under certain conditions Abel inversion analysis can still be a preferable method. For Abel inversion, there is no need to rotate or observe the gas-jet under multiple angles as is required for tomographic analysis. Therefore, especially in the case of on-site analysis of gas-jet targets during LWFA experiments where the degradation of the gas-nozzle has to be monitored, Abel inversion analysis can be favourable due to the simplification of the setup.

3.4.3. COMPARISON BETWEEN ARGON AND HELIUM GAS

Although LWFA experiments are generally performed on helium jets, the nozzles used to provide these jets are often characterised using argon gas[120–122,137]. This is for the higher refractive index of argon compared to helium (Table 3.1), which will result in a corresponding larger phase shift, thus relaxing the sensitivity requirements of the interferometry setup. Argon and helium are both mono-atomic gases with the same adiabatic index. Theory and simulation performed for de Laval type nozzles predict different nozzle exit velocities for argon and helium, but no major differences in gas density[134,138].

To test whether this assumption can be applied, a gas density measurements on a nozzle driven by both argon and helium is performed. The nozzle used for this comparison is a Mach ∼3.3 nozzle (Sourcelab SL-NOZ-SS) with a throat size of 0.5 mm and an exit size of 1 mm.

Tomography depends on measurements under multiple angles for which is assumed that the gas-jet is equal for every shot. Therefore the shot-to-shot stability of the jet is important. This is also relevant for LPA operation where a stable acceleration medium is

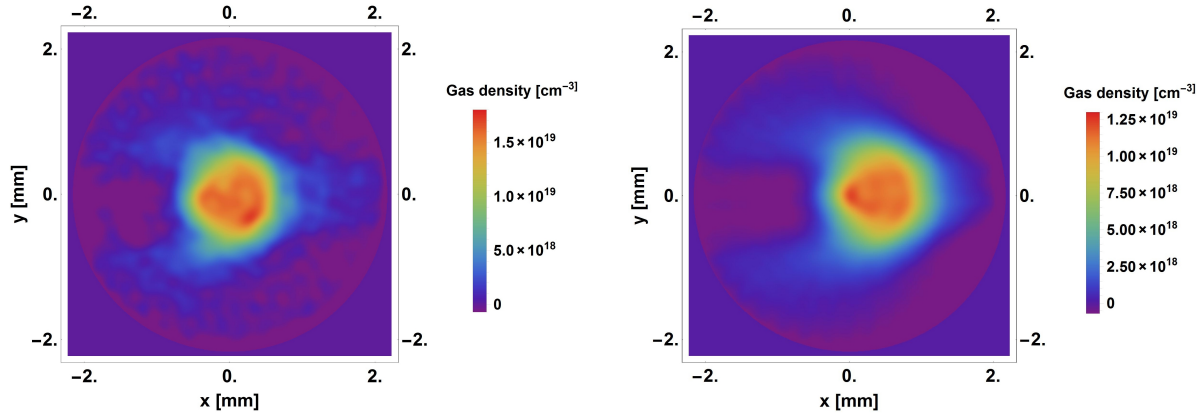

(a) Helium gas density profile

(b) Argon gas density profile

Figure 3.13.: **2-D Gas density profile at helium and argon.** Acquired with a 0.5 mm throat, 1 mm exit Mach 3.3 nozzle. 1 mm above the nozzle exit, obtained by tomographic reconstruction. Driven at 40 bar backing pressure for both helium and argon.

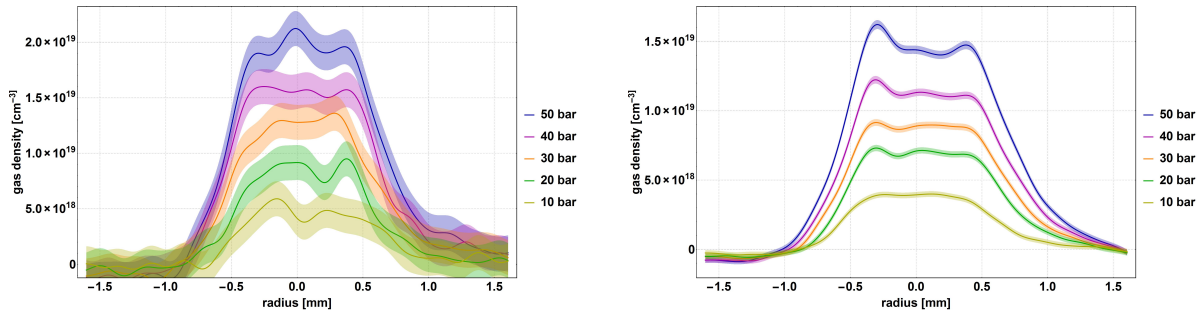

(a) Helium gas density profile.

(b) Argon gas density profile

Figure 3.14.: **Gas density line-outs at different backing pressures.** Acquired with a 0.5 mm throat, 1 mm exit opening Mach 3.3 nozzle. 1 mm above the nozzle exit, obtained by tomographic reconstruction. Driven by both Argon and Helium gas. The area around the solid line indicates the measurement uncertainty.

required. To evaluate the shot-to-shot stability of the target, ten different measurements at one minute intervals with the gas-jet driven at 20 bar argon were taken. One angle is considered and the stability is evaluated on the acquired phase maps. The inner area of the jet (± 0.25 mm around the centre and up to two mm from the nozzle exit) is considered. In this area the gas-jet shows an average shot-to-shot relative phase fluctuation of 1.6% (standard deviation). Thus the jet shows stable behaviour such to not add any relevant error to the tomographic reconstruction when multiple angles over separate shots are considered.

Figure 3.13 shows the 2-D gas density maps at 1 mm above the nozzle exit for both argon and helium at 40 bar backing pressure. The density maps have been acquired by tomographic reconstruction using 20 angles. The reconstruction shows an asymmetry, which is believe to originate either from an irregularity of the nozzle or from an imperfect alignment of the nozzle onto the valve. Note that this asymmetry can only be diagnosed because of the use of tomographic reconstruction.

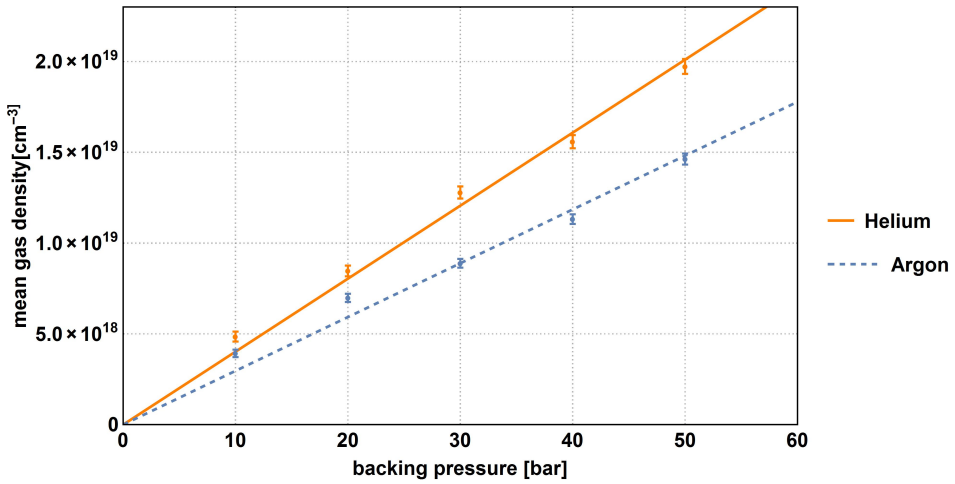

Figure 3.15.: **Mean gas density dependency on backing pressure for helium and argon.** Density determined at the jet centre for different backing pressures with corresponding linear fits.

Figure 3.14 shows line-outs for different backing pressures for both argon and helium. The shaded area around the measurement line shows the uncertainty and includes gas-jet stability as mentioned above as well as an analysis uncertainty. The analysis uncertainty has been determined by processing a zero-measurement without gas-jet present (section 3.4.1) that has been acquired under experimental conditions. This zero-measurement is processed using the same procedure as used for gas-jet data, including tomographic reconstruction. The maximum phase error found in the reconstruction is taken as the analysis uncertainty. Taking refractive indexes of both gases into account, this results in an local absolute gas density uncertainty of $1.95 \times 10^{17}\,\mathrm{cm}^{-3}$ for argon and $1.58 \times 10^{18}\,\mathrm{cm}^{-3}$ for helium.

Figure 3.15 shows the average gas densities around the centre (±0.3 mm) of the jet together with a linear fit for both argon and helium. The error bar here is smaller compared to figure 3.14, as for determining the mean gas density not the local gas density uncertainty (determined by the maximum phase error) is relevant, but the gas density uncertainty over the entire centre of the jet is relevant. There is a clear difference between the densities obtained with both gases. In this specific case one needs apply a correction factor of 1.36 (±10%) to convert a density measurement performed on argon to the helium gas density.

3.4.4. LPA GAS MEDIUM CHARACTERISATION

The nozzle used for the LPA and beam loading experiments as described in chapter 4 & 5 is characterised and analysed with the setup and methods as described above. The nozzle used in this case is a Mach 10.4 supersonic de-Laval nozzle with a 0.35 mm throat and a 3 mm exit diameter, according to the design found in appendix D. It has been designed to provide a laminar gas-jet with steep gradients and a flat-top density profile[134]. The nozzle is mounted on a Parker 9-series fast gas valve as shown in figure 3.16(a). An opening time of 20 ms before characterisation was chosen in order to reach a steady-flow state. The same opening time was also used LPA operation.

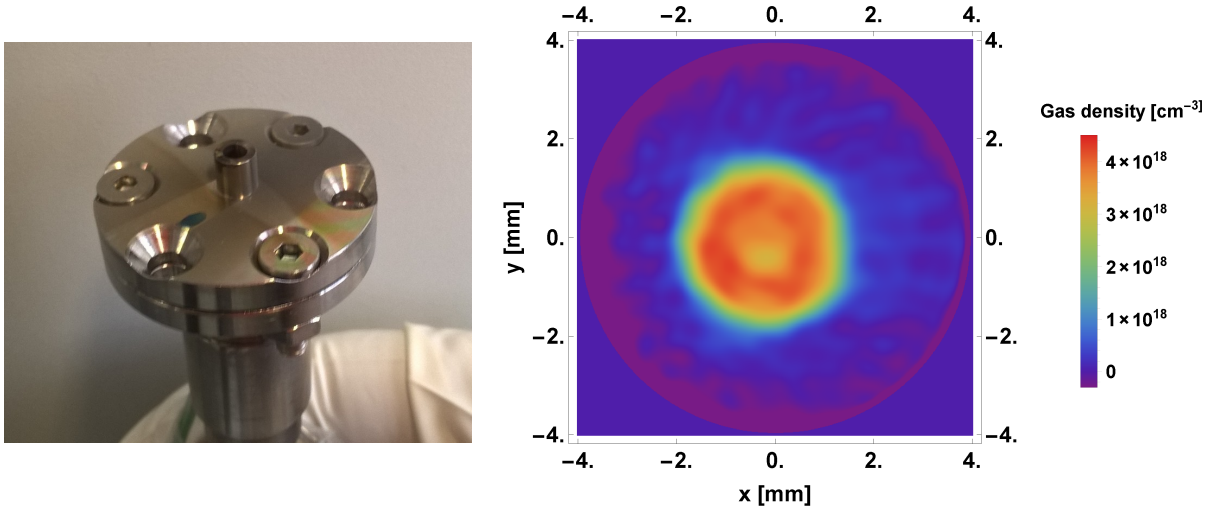

(a) Nozzle mounted on a Parker 9-series gas valve.

(b) Density profile of the helium gas jet at 1 mm above the nozzle opening at 25 bar backing pressure.

Figure 3.16.: **LPA medium provider.** Supersonic de Laval nozzle (Mach 10.4) with a 3 mm exit diameter

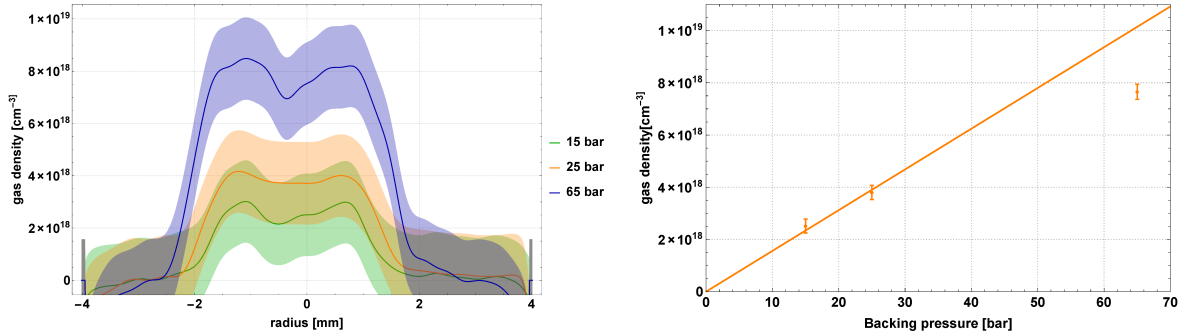

(a) Lineout of the density profile through the gas-jet centre at z = 1 mm for different backing pressures. The area around the solid line indicates the measurement uncertainty.

(b) Density dependence on backing pressure.

Figure 3.17.: **Characteristics of the helium gas jet.** Driven by a 3 mm Mach 10.4 supersonic de-Laval nozzle at 1 mm above the nozzle opening.

A tomographic reconstruction based on twenty angles of the helium gas-jet delivered by this nozzle is shown in figure 3.16(b). The gas nozzle was driven with 25 bar backing pressure and the reconstruction is at 1 mm above the nozzle opening. The small offset of the jet from the reconstruction centre is due to positioning precision in the interferometric setup. In contrast to the gas-jet characterised in section 3.4.3, the gas-jet shows an axisymmetric density profile. The nozzle does not provide a perfect flat-top profile, but has a small depression at the centre. This is also visible on the density line-out shown in figure 3.17(a). Because this jet is operated at a relatively low gas density, the measurement uncertainty area around the measured profile is relatively large. As described above this region is determined by the maximum analysis uncertainty and therefore represents potential local density variations that might not be experimentally resolved.

Figure 3.17(b) shows how the average gas density along the center of the gas jet depends on the backing pressure. The gas density initially follows the expected linear dependency up to a backing pressure of 25 bar, corresponding to a gas density of $3.9 \times 10^{18}\,\mathrm{cm}^{-3}$. A clear deviation is present at 65 bar. It is suspected that this deviation is due to a limited orifice opening of the pressure valve. In experiment the nozzle is operated below 25 bar backing pressure, within the linear range.

3.5. ELECTRON SPECTROMETER

In order to determine the electron beam quality after the LPA, key beam parameters such as energy, energy spread, charge, divergence, pointing, emittance and duration need to be determined. Except for emittance and duration, these parameters can be directly diagnosed by the electron spectrometer.

A single shot spectrometer that covers an entire energy range from a few MeV up to several hundreds of MeV is required in order to properly characterise the acceleration process while still retaining a high energy resolution. This in contrast to well-established conventional accelerators, where electromagnets (often in combination with permanent magnets) are used, aiming at a high energy resolution at a limited but tunable energy range.

The spectrometer which was designed and implemented to accommodate above-mentioned requirements is presented in this section. It consists of a permanent dipole magnet that energy-dependent deflects electrons, spatially separating them according to energy on a charge-sensitive scintillating screen. The spectrometer is designed to cover a range from a few MeV up to 550 MeV, limited at the upper range by spatial restrictions in the experimental chamber. To account for LPA shot-to-shot pointing jitter and beam divergence, the spectrometer was designed to provide point-to-point imaging up to 200 MeV while at higher energies the measurement uncertainty is kept below 6% for typical LPA operation.

The approach in designing and optimising the spectrometer is as follows. First, the three-dimensional field of the spectrometer is measured and presented in section 3.5.1. Then, in section 3.5.2, the spectrometer is represented as a first order 6×6 transfer matrix to extract the requirements for point-to-point imaging. The parameters extracted from this linear approach were used as starting values in section 3.5.3 for the numerical optimisation via particle tracing using the measured field map. The energy accuracy of the final design is discussed in section 3.5.4. Charge diagnostic using scintillator screens and their calibration is discussed in section 3.5.5 and their implementation into the spectrometer in section 3.5.6.

3.5.1. DIPOLE FIELD MAP

The magnetic dipole forming the basis for the spectrometer in this work consists of four 100 mm × 150 mm dipole magnet sections giving a total length of 400 mm as shown in figure 3.18(a). Each section consists of an iron yoke with six permanent magnets (VACODYM 764 TP[139]) at each side with a 40 mm pole gap and a design field strength of ∼1 T.

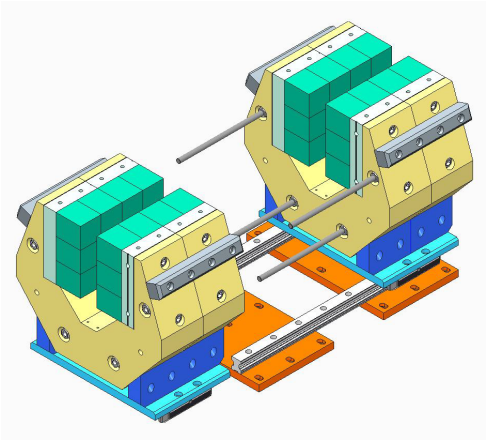

(a) **Spectrometer dipole design.** Not all sections are connected in this drawing. Every section contains twelve permanent magnets (turquoise) connected to a iron yoke (yellow). The dipole is mounted on a rail to allow exact positioning.

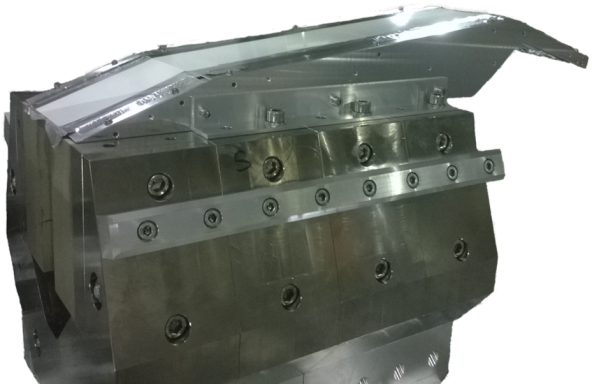

(b) **Photograph of spectrometer dipole with mounted lanex screen for electron detection.** Electrons enter the spectrometer from the left. The light shielding structure is removed in this picture in order to show the lanex screen position.

Figure 3.18.: **400 mm dipole spectrometer.** Dipole design *(a)* and a photograph of the spectrometer *(b)* with lanex screen mounted for electron detection.

The design field strength can be used for spectrometer design under the assumption of an ideal dipole field, but material and construction imperfections can cause deviations from the predicted field.

In order to quantify and consider such deviations field mapping was performed for the relevant section of the dipole using a Hall probe (Lakeshore MMTB-6J04-VG) with a three-dimensional two millimetre grid. The resulting field map is show in figure 3.19. The peripheral magnetic field extends out of physical borders of the dipole, forming the fringe field. The maximum field strength is only reached further inside the magnet, with the measured magnetic field 0.9 T compared to the design value of ∼1 T.

Comparing two-dimensional slice field maps at the centre of the dipole (figure 3.19(b)) and closer to the pole (figure 3.19(c)) we notice that the field is not completely homogeneous between the poles, this effect being most pronounced at the edges. Furthermore periodical field fluctuations are visible originating from the combination of individual magnets from which the dipole is constructed as shown in figure 3.18(a).

An particle tracking simulation is performed in section 3.5.3 tracing electron trajectories propagating within the measured 3D magnetic field to take above-mentioned observations into account.

3.5.2. SPECTROMETER BASICS AND MATRIX APPROACH

The core principle of the electron energy spectrometer is the deflection of moving electrons in its dipole magnetic field following the Lorentz equation ($\vec{F} = -e\vec{v} \times \vec{B}$). Given a fixed magnetic field strength B, the radius ρ of the path followed by an electron depends on its momentum p according to the cyclotron equation:

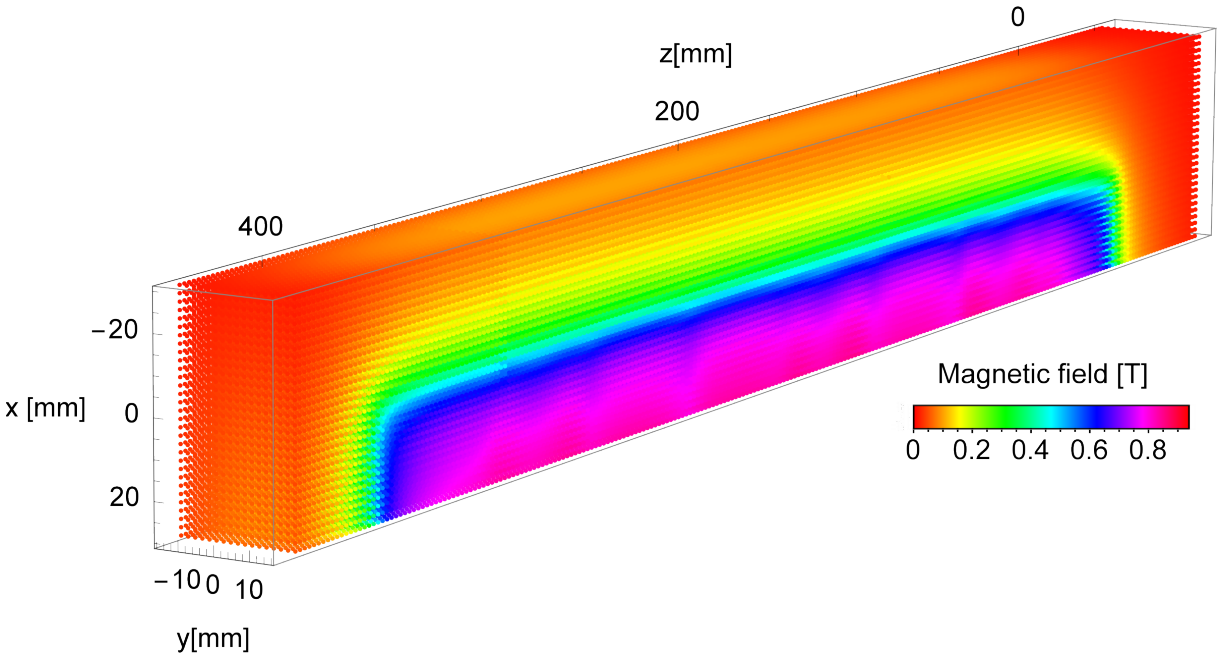

(a) Three-dimensional field map of the upper region of the spectrometer dipole.

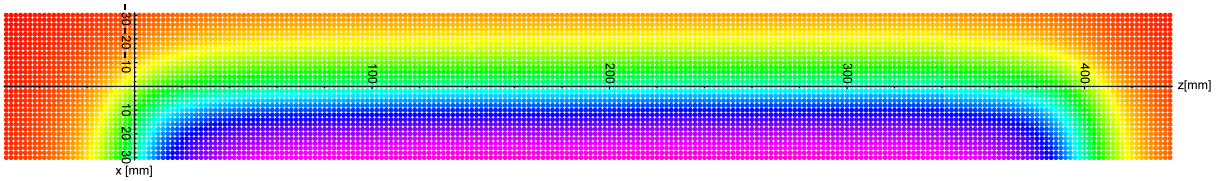

(b) 2-D field map at y = 0 mm, i.e. equidistant from both poles.

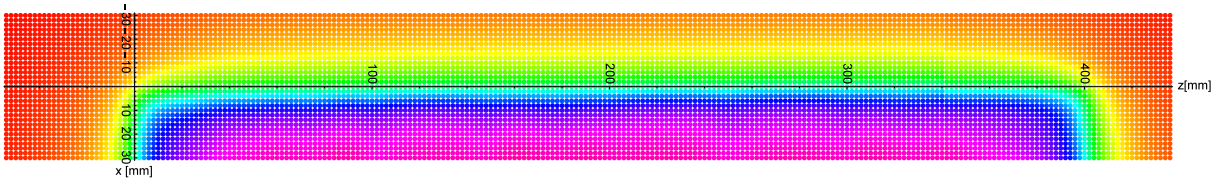

(c) 2-D field map at y = 14 mm.

Figure 3.19.: **Measured magnetic field map of the electron spectrometer dipole.** Each dot represents a measurement point with the colour indicating the local magnetic field strength. The field strength was measured on a three-dimensional 2 mm grid. The physical top edge of the spectrometer dipole is situated at the x=0 mm plane. The physical sides of the dipole are located at z=0 mm and z=400 mm. The y=0 mm plane marks the middle of the pole gap.

$$\rho[\mathrm{m}] = \frac{p\left[\frac{\mathrm{GeV}}{\mathrm{c}}\right]}{0.2998 B[\mathrm{T}]}. \tag{3.11}$$

This bending radius is known as the Larmor or cyclotron radius. Different momentum-dependent Larmor radii result in a spatial separation after the dipole from which the original electron energies can be deduced.

A convenient way to calculate the path of electrons through a dipole is provided by matrix calculations where a transfer matrix describes the transport of an electron or a beam envelope through a magnetic system. A first-order matrix 6 × 6 approximation of bending magnets is given in ref.[140]. The vector of the input beam is given by:

$$X = \begin{bmatrix} x \\ x' \\ y \\ y' \\ \delta l \\ \frac{\delta p}{p} \end{bmatrix}, \tag{3.12}$$

where y is the coordinate out of the page, δl is the path length difference from the reference particle trajectory and $\delta p/p$ is the relative momentum difference from the central momentum. Given a transport matrix T of a system, the beam parameters after passing through the system, X', can be calculated by

$$X' = TX. \tag{3.13}$$

The transport matrix T is constructed by several individual segments. The main body of a dipole can be described by

$$M_{\mathrm{body}}(\rho, \alpha) = \begin{bmatrix} \cos(\alpha) & \rho \sin\alpha & 0 & 0 & 0 & \rho(1-\cos\alpha) \\ -\frac{\sin(\alpha)}{\rho} & \cos\alpha & 0 & 0 & 0 & \sin\alpha \\ 0 & 0 & 1 & \rho\alpha & 0 & 0 \\ 0 & 0 & 0 & 1 & 0 & 0 \\ \sin\alpha & \rho(1-\cos\alpha) & 0 & 0 & 1 & \rho(\alpha-\sin\alpha) \\ 0 & 0 & 0 & 0 & 0 & 1 \end{bmatrix}, \tag{3.14}$$

where ρ is the Larmor radius from equation (3.11). α is the circle sector of the electron's trajectory within the dipole. Fringe fields at both the entrance and the exit of the dipole will result in an edge focussing effect which in the first order can be described by

$$M_{\mathrm{edge}}(\beta, \rho) = \begin{bmatrix} 1 & 0 & 0 & 0 & 0 & 0 \\ \frac{\tan\beta}{\rho} & 1 & 0 & 0 & 0 & 0 \\ 0 & 0 & 1 & 0 & 0 & 0 \\ 0 & 0 & -\frac{\tan(\beta-\psi)}{\rho} & 1 & 0 & 0 \\ 0 & 0 & 0 & 0 & 1 & 0 \\ 0 & 0 & 0 & 0 & 0 & 1 \end{bmatrix}. \tag{3.15}$$

β is the angle under which electrons enter or exit the magnetic field. For positive β the edges are defocussing in the bending plane and focussing in the non-bending plane.

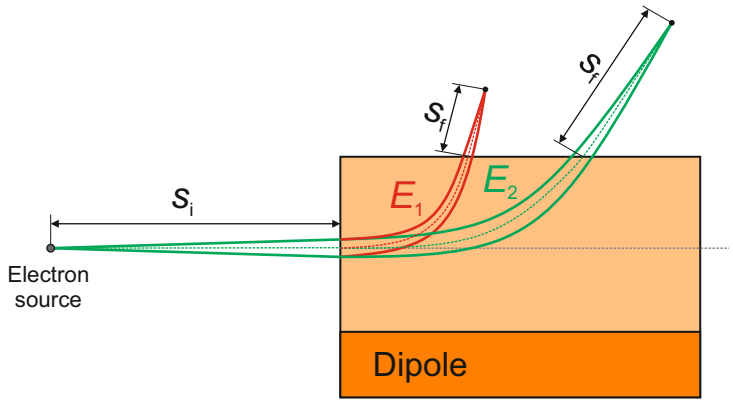

Figure 3.20.: **Schematic representation of dipole point-to-point imaging.** Shown are two divergent electron beams ($E_1 < E_2$) originating from the exit of the plasma accelerator, which acts as a point source. Using dipole focussing, energy-dependent imaging occurs when $T_{12}(s_i, s_f) = 0$ (equation (3.18)).

The angle ψ is a correction angle related to the finite length of the fringe field due to the finite dipole gap size G, and is given by

$$\psi = \frac{KG}{\rho}(1 + \sin^2\beta). \tag{3.16}$$

The fringe field integral K is dependent on the field geometry and is equal to 1/6 for a linear field.

Drift sections of a length s can be described by

$$M_{\text{drift}}(s) = \begin{bmatrix} 1 & s & 0 & 0 & 0 & 0 \\ 0 & 1 & 0 & 0 & 0 & 0 \\ 0 & 0 & 1 & s & 0 & 0 \\ 0 & 0 & 0 & 1 & 0 & 0 \\ 0 & 0 & 0 & 0 & 1 & s \\ 0 & 0 & 0 & 0 & 0 & 1 \end{bmatrix}. \tag{3.17}$$

For a dipole spectrometer the overall transport matrix from object (plasma accelerator source) to image (charge diagnostic screen) can be constructed from above-mentioned segments:

$$T = M_{\text{drift}}(s_f) \cdot M_{\text{edge,exit}}(\beta_{\text{exit}}, \rho) \cdot M_{\text{body}}(\rho, \alpha) \cdot M_{\text{edge,entr}}(\beta_{\text{entr}}, \rho) \cdot M_{\text{drift}}(s_i). \tag{3.18}$$

Electron beams from laser plasma accelerators can exhibit relatively large shot-to-shot pointing fluctuations due to laser pointing stability and the acceleration process itself. Furthermore, the beam will have a certain divergence, which can also fluctuate. These effects will result in non-zero terms for the beam initial transversal momentum, i.e. x_i' and y_i' in equation (3.12). Such non-zero terms can have a negative influence on the resolution of the spectrometer, as they add to the momentum dependency for position in the system's transfer matrix. This effect can be prevented by equipping the spectrometer with a finite size entrance slit directly at the dipole entrance, thus fixing the entry position and angle of electrons by sampling only a part of the electron

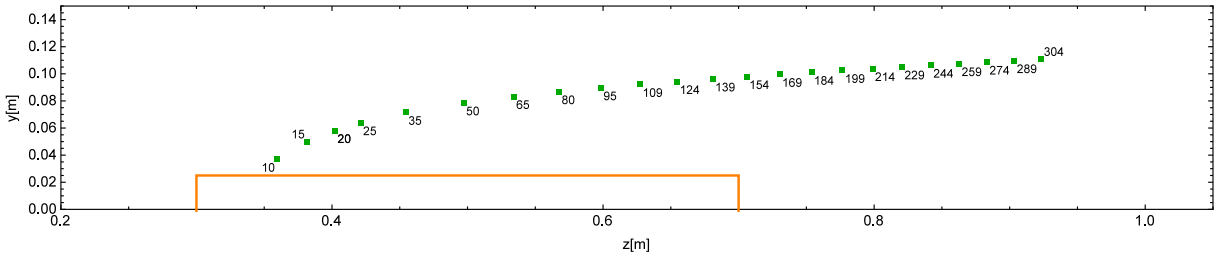

Figure 3.21.: **Spectrometer imaging points determined by first-order matrix calculations assuming a dipole with an 1 T field strength.** The orange outline indicates the dipole position. The electron source (object point) is located at the origin y=z=0 (not shown in this figure). The green squares indicate a selection of calculated imaging points for different electron energies, indicated in MeV.

bunch. However, as the energy-discriminative charge diagnostic is located after the dipole, this is not a viable option. Instead, the spectrometer is designed such that it exhibits point-to-point imaging in the bending plane over an as large as possible energy range. The exit of the plasma accelerator forms an object point which is imaged on the scintillator screen with a certain magnification. Point-to-point imaging is shown in figure 3.20 and occurs in the bending plane with object distance s_i and focal plane distance s_f when $T_{12}(s_i, s_f) = 0$. Assuming the exit of the accelerator as a stable point, i.e. $x_i \,\&\, y_i \ll s_i \,\&\, s_f$, this criterion is used to define the spectrometer geometry.

The dipole is placed at 300 mm from the accelerator exit in order to facilitate further experimental tools, e.g. electron beam profiler, foils for transition radiation, plasma mirror for Thomson scattering experiment etc. This fixes s_i for all energies. Using equation (3.18) several geometries can be explored by varying the electron entry point at the dipole and dipole orientation angle, thus changing the spectrometer energy range and imaging points positions. A for-purpose optimal geometry with the electron entry point 25 mm from the top corner of the dipole and no rotation in respect with the electron beam axis was found. This configuration gives a point-to-point imaging range from 10 up to 300 MeV, limited at the upper energy level by spatial construction restrictions. The positions of the imaging points relative to the dipole are shown in figure 3.21.

3.5.3. PARTICLE TRACING

With the measured three-dimensional magnetic field map presented in section 3.5.1, particle tracing can be used to make a more accurate calibration of the electron spectrometer compared to the matrix approach described before. This way the actual magnetic field maps is taken into account, including the observed local field strength fluctuations and without relying on an idealised description of the fringe field.

For this purpose, the measured field strength map was implemented in the General Particle Tracer (GPT) code[141]. Test particles with different momentum are introduced into the simulation originating from a virtual particle accelerator. For each energy three test particles are introduced, one with zero pointing, following the reference trajectory, and two with a certain pointing/divergence in the dipole bending plane. These outer particles have equal divergence magnitude, but with opposite sign. The result of this

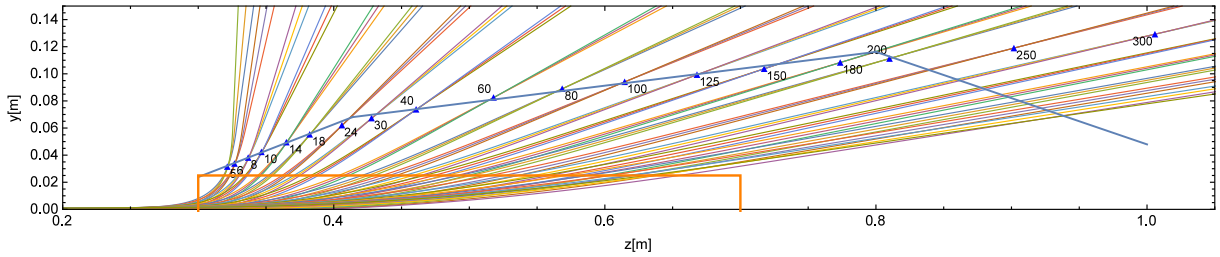

Figure 3.22.: **Simulated path of electrons through the spectrometer dipole.** Simulations performed using the GPT code. The physical borders of the dipole are outlined in orange. For every energy three paths are simulated, one for zero pointing and two for a positive and negative divergence/pointing of 5 mrad. The electron source (object point) is located at the origin (not shown in this figure) and the blue triangles are imaging points for specific energies (labels in [MeV]). The blue line segments show the position of the scintillator screens chosen for optimal resolution given the physical constraints.

simulation is shown in figure 3.22 with a selection of energies shown.

Due to the dipole focussing effect, per energy the three test particles' trajectories intersect, forming an imaging point indicated by the blue triangles. These points are insensitive to divergence (in the bending plane) or pointing fluctuations. The focal length of the system increases with increasing electron energies thus placing the focus point of higher energies further away from the dipole.

The focus points acquired from particle tracing are used to choose the position of the scintillating screens for electron detection. Three separate screens are positioned under different angles to reach optimal overlap with the focus points, given the physical constraints. The screen positioning is indicated by the blue lines in figure 3.22 and can also be seen in figure 3.18(b). The physical constraints, given by vacuum chamber size, laser and diagnostic optics and the required scintillator screen imaging system, are not shown in these figures.

From 5 to 200 MeV every screen position is located at or near to point-to-point imaging. The screen covering higher electron energies does not overlap with the focus points. This solution is chosen to abide to spatial constraints and to limit screen size while retaining a large enough measurement range for divergence in the non-bending axis. Laser beam diagnostics directly behind the spectrometer (not shown in image) limits the maximum length of the high energy screen, limiting the maximum resolved energy to 550 MeV.

COMPARISON BETWEEN PARTICLE TRACING & MATRIX CALCULATION

Figure 3.23(a) shows a comparison between the results obtained from particle tracing and results obtained from the first order matrix calculation. The scintillating screen positioning as chosen from GPT tracing using the measured field map deviates clearly from the focus positions predicted by matrix calculation. The particle tracing simulations show a clearly lower bending power of the dipole, being most pronounced at higher energies.

The differences between GPT tracing and matrix calculation partially occur due to the lower measure maximum field of the dipole magnet compared to its assumed

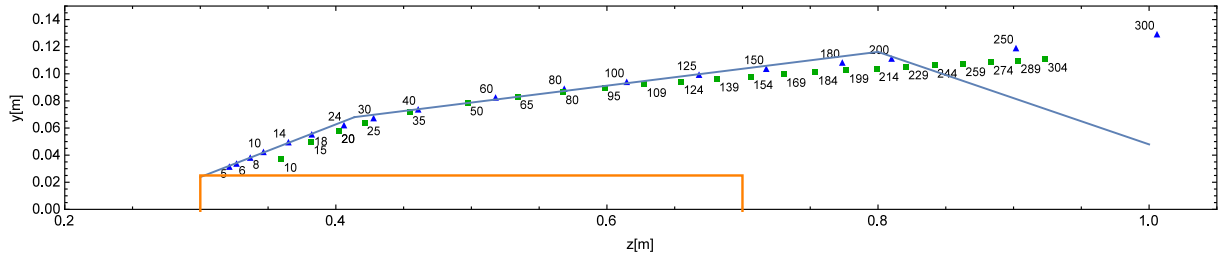

(a) Comparison between imaging points acquired by first order matrix calculation assuming a 1.0 T dipole (green squared) and imaging points acquired by particle tracing.

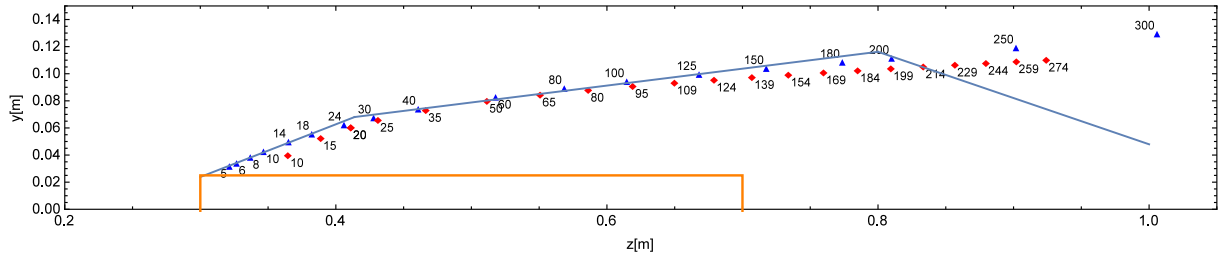

(b) Comparison between imaging points acquired by first order matrix calculation assuming a 0.9 T dipole (red diamonds) and imaging points acquired by particle tracing.

Figure 3.23.: **Comparison between imaging point acquired by first order matrix calculation and particle tracing.** Particle tracing was performed using the General Particle Tracer software using a measured magnetic field map. Labels show electron energy in MeV for particle tracing image points (above the points) and matrix calculation points (below the points). The electron source (object point) is located at the origin (not shown in this figure) and the dipole physical border is indicated by the orange outline. The blue line segments show the position of the scintillator screen chosen in the final design.

design value used in the GPT tracing. Figure 3.23(b) shows a comparison between both methods, now assuming an ideal dipole with ideal fringe fields according to the approach of equation (3.18) with a maximum field of 0.9 T.

In this case the differences between both methods become less pronounced, especially for higher electron energies, although a mostly vertical offset of imaging points is still present. At lower energies there is still a large difference between both methods, both in imaging point position and energy scaling. This is due to low energy electrons traversing a relative large fraction of their total path or even exclusively through the fringe field located at the dipole corner (figure 3.19(b)) which is not correctly described by the first order approximation used in the matrix calculations.

Thus, in spectrometer design, the matrix approach using an idealised magnetic dipole field can be used as a quick parameter study tool. Then, in order to achieve a correct energy calibration with an optimal resolution, it is required to perform a particle tracing simulation using a measured field map of the entire relevant dipole section.

3.5.4. SPECTROMETER ACCURACY

The section above describes how the point-to-point imaging is used in order to minimise the spectrometer energy readout error caused by to beam pointing. However, as the scintillator screens are flat and bending is to be avoided, the imaging screen is divided into three flat sections to give the best practical executable solution while approaching

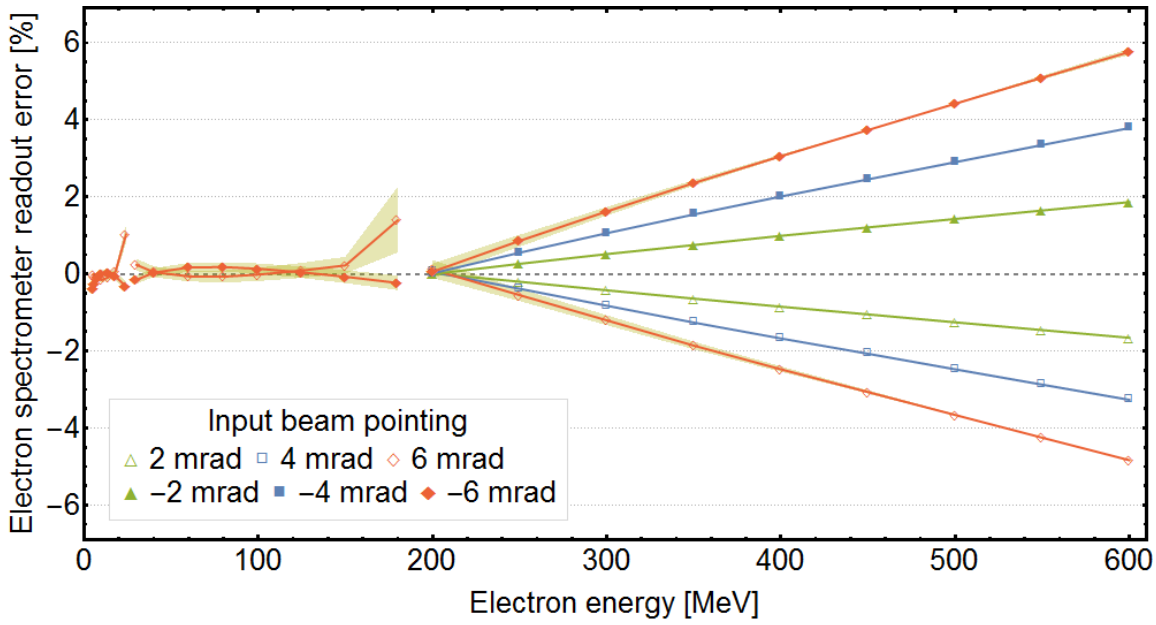

Figure 3.24.: **Divergence and electron source position dependent readout error of the electron spectrometer.** Results obtained by particle tracing in GPT using the measured field map. Values shown indicate a divergence/pointing of the incoming beam in the bending plane. Shaded areas indicate the influence of vertical position errors of the incoming beam (+/- 0.2 mm) on top of a +/- 6 mrad pointing error. Figure also published in[4].

the point-to-point imaging configuration as best as possible. Above 200 MeV the point-to-point imaging is abandoned due to spatial constraints and to limit the screen size. These two design choices result in a readout error of the electron spectrometer dominated by beam divergence and pointing in the magnet's bending plane. Utilising the same particle tracing method, again using the measured magnetic field strength map, this effect has been simulated and the results are shown in figure 3.24 for typical divergence values and transverse position offsets.

The two sections for low energies (up to 200 MeV) each have two positions where beam pointing does not add any error, at these positions the screen is positioned exactly at an imaging point. Further away from these positions the error grows, but the readout error stays below 1.4% for a beam pointing up to 6 mrad. For the high energy screen, above 200 MeV, the error grows strongly with electron energy as the imaging points no longer overlap with the readout screen.

Besides pointing fluctuations and divergence the input beam can also exhibit shot-to-shot fluctuations in transverse position. The influence of has also been investigated and the effect of a 0.2 mm vertical position offset is also shown in figure 3.24, indicated by the shaded area on top of a of a +/- 6 mrad pointing error. This additional readout error becomes most relevant at energies around 180 MeV where it rises to roughly 0.9%. At this point a 6 mrad pointing error combined with a 0.2 mm beam source offset causes an energy readout error of 2.2%. For the region where no point-to-point imaging is present the offset error is negligible compared to the pointing readout error. Errors caused by a horizontal offset (source distance to spectrometer entrance) were also investigated, but due to the relatively large object (s_i) and screen distance, these were found negligible even for large offsets up to 1 mm.

3.5.5. SCINTILLATOR SCREEN CALIBRATION

After dipole dispersion, a detector is required that is able to resolve both the spatial distribution, required for determining the energy distribution, and the local charge distribution. As electron beam energy is mapped to position over several hundreds of cm^2, this detector has to cover a large area. Specifically, the electron spectrometer as is shown in section 3.5.3 covers 658 mm × 75 mm = 49350 mm^2. Established techniques for charge determination like Integrating Current Transformers (ICT) or Faraday cups are not suitable, as they do not offer the required spatial resolution.

Instead, scintillator screens offer a feasible alternative. These screens consist of powdered rare earth phosphor, e.g. terbium doped gadox (Gd_2O_2S:Tb), deposited in a typically 10 to 100 µm thick layer on a plastic carrier. Such screens are commercially available, commonly under the trade name LANEX. Although marketed for x-ray detection, they are also suitable for charge-sensitive electron detection, where part of the electron beam energy is converted into visible light. This process is dominated by fluorescence with a sub-millisecond lifetime[142], making these detectors suitable as single shot diagnostics at relevant LPA repetition rates of several hertz. This in contrast to imaging plates, which also offer spatial-dependent charge diagnostic with a high dynamic range[143–145], but require a slow readout process, making them only useful as an one-shot diagnostic.

Scintillator screens generally do not have a manufacturer specified response to relativistic electrons and therefore require calibration before they can be implemented as a charge diagnostic. Several calibration studies have been performed and published[146–149] on this topic. The work of Buck et al.[147] offers an absolute calibration of several commercially available screens and has been widely used as a reference for charge determination in the LPA-community. However, this calibration from 2008 was performed at the ELBE accelerator under different conditions than typically found in LPA beam diagnostic and has several shortcomings.

Two shortcomings offer major potential interfering noise sources. In order to image the scintillating screen, Buck et al. placed a mirror in the path of the electron beam. This can be a source of optical transition radiation (OTR) which can be a significant extra light contribution if collected by the camera[150]. Furthermore, the electron beam was coupled out from the accelerator vacuum system through a beryllium window, potentially causing an additional charge-dependent Bremsstrahlung x-ray background, to which the scintillator screens are highly sensitive.

A further two deviations from typical operational conditions in LPAs were also present in the 2008 setup, but are not expected to have a major influence. Firstly, the scintillator screens were not positioned in vacuum but were excited in air. Secondly, the beam size was expanded up to over ten millimetres compared to typical few millimetres, thus a higher total charge was required to reach the same spatial charge density.

Above-mentioned points have been carefully addressed in an improved calibration setup designed to closely mimic LPA beam detection conditions, this setup is schematically shown in figure 3.25

As in Buck et al., scintillator screens are cross-calibrated at the ELBE conventional electron accelerator, introduced in section 3.1. To be calibrated screens are positioned

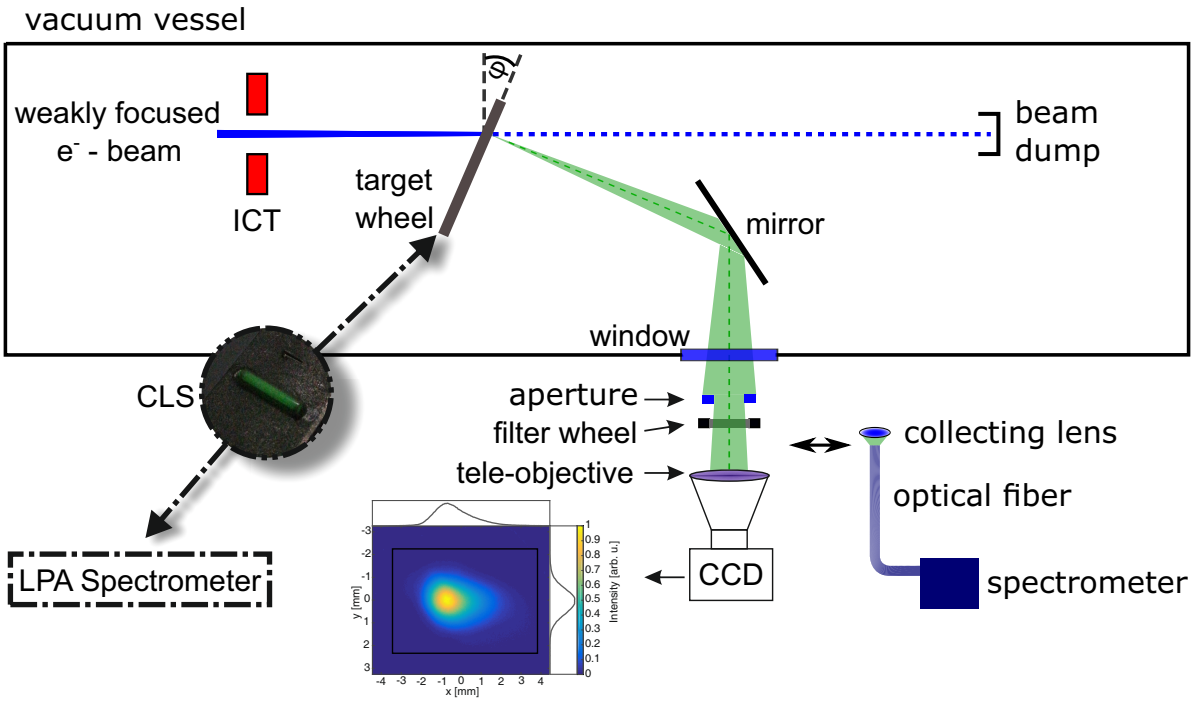

Figure 3.25.: **Lanex calibration setup.** The electron beam from the conventional accelerator ELBE is weakly focussed onto the scintillating screens, which are positioned in a rotational target wheel. The scintillator screen under a normal angle observation is imaged onto the CCD camera. A CLS (*inset*) is also positioned in the target wheel to provide relative cross-calibration for the LPA spectrometer after the scintillator screen calibration. Figure adapted from[11].

inside a vacuum vessel directly connected to the accelerator beam-line with the electron beam weakly focused to a spot of 2 to 3 mm^2 (FWHM) onto the screen by magnetic quadrupoles several metres upstream. Scintillating screens are mounted on a rotatable target wheel, enabling calibration of multiple screens within the same beamtime. Directly in front of the target wheel an ICT (ICT-082-070-05:1-VAC, Bergoz Instrumentation, France) is placed for charge determination. Its signal is amplified by an amplifier (ZPUL-30P, Mini-circuits) and is recorded by an oscilloscope (RTE1204, Rhode & Schwarz, Germany) on a 50 Ohm termination for every single interaction. After interaction the electron beam is disposed of in a shielded beam dump.

The scintillator screens are imaged onto a 12-bit CCD camera (Basler acA1300-30gm) with a tele-objective. Special care is taken to place the mirror of the optical imaging system out of the electron beam path to avoid optical transition radiation superimposing with the scintillator screen signal. A filter wheel with neutral-density (ND) filters at optical densities ranging from 0.5 to 4.0 offers a dynamic range of four orders of magnitude on top of the camera's dynamic range. The ND-filters are calibrated using a photo–spectrometer (Cary 50 UV-VIS) with sub-0.5% relative error, taking into account the emission spectrum of the scintillator screens, which are measured by a fibre coupled spectrometer (Ocean Optics, HR4000). An aperture is introduced to the optical imaging system limiting the collecting angle to $(3.18 \pm 0.07) \times 10^{-3}$ sr. The target wheel has been placed at a $\varphi = (22 \pm 1)°$ angle offset from perpendicular to the beam propagation such that the screen can be observed under a zero degree angle. This angle results in

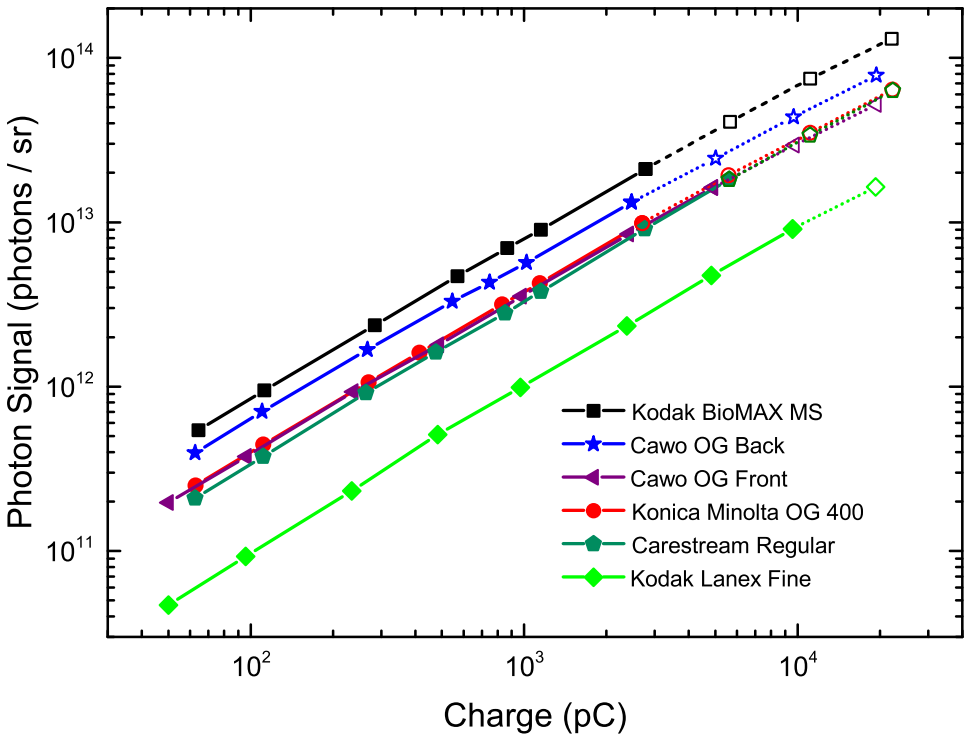

Figure 3.26.: **Scintillator screen response to relativistic electrons** for several commerially available screens. Filled data points, connected by a solid line, are within the region where a screen shows a linear response. Open data points, connected by a dotted line, indicate the region where the screens deviate from linear response by at least 10%. Figure adapted from[11]

a longer interaction length of the electron beam with the phosphoric layer by a factor $1/\cos(\varphi)$ compared to perpendicular incidence. The scintillator signal increases linearly with the interaction length and this factor is taken into account in the analysis.

The calibration of the scintillator was performed at the ELBE accelerator at 23 MeV. As the ELBE accelerator is not tunable toward a higher energy range, the energy-dependent response of the scintillator could not be experimentally determined. However, simulations and measurements show that the energy deposition in scintillating screens per electron is almost constant for electron energies above 3 MeV[146,149,151,152] Nakamura et al.[148] also discuss this issue in detail. In this paper a near-linear (1% less photons for every 100 MeV energy increase) response of scintillating screens was experimentally confirmed in the energy range between 106 and 1522 MeV. Thus the calibration performed at 23 MeV can be assumed valid for all relevant relativistic electron energies.

This setup is used to create an absolute response calibration, i.e. emitted photons per solid angle per picocoulomb, of multiple scintillator screens over a large charge density range. This study, including saturation, degeneration and long-term stability tests, is reported in full detail in ref.[11]. The response of several scintillating screens is shown in figure 3.26. The Konica Minolta OG 400 scintillating screen characterised here is also implemented in the spectrometer, with all screens originating from the same production batch. They are found to have a linear response up to $(1.9 \pm 0.2) \times 10^3\,\mathrm{pC\,mm^{-2}}$, which is well above the charge densities observed in experiment of up to $2.5\,\mathrm{pC\,mm^{-2}}$. Using all data points within the linear regime, the absolute response to relativistic electrons is

Table 3.2.: **CLS calibration values.**

CLS #	$N_{scint}/N_{CLS,100\,ms}\,Q^{-1}$ [pC^{-1}]
1	2.06
2	1.86
3	1.85
4	1.92
5	2.00
6	1.96
7	1.91
8	1.92

determined to be $(3.7 \pm 0.7) \times 10^9$ photons $sr^{-1}\,pC^{-1}$.

An absolute response calibration is a good method to compare separate calibrations and can also be used to calibrate charge diagnostics in which scintillator screens are used. However, intermediate steps are required which have to be implemented with great care in order to avoid errors. The imaging system absolute collection angle, the imaging system attenuation factor and the camera photon-to-count efficiency has to be determined. To avoid these complexities and potential error sources a relative calibration method is used instead, which is easier and more reliable to implement.

In relative calibration a constant light source (CLS) is used to cross-calibrate the imaging system at the lanex calibration setup with the imaging system at the charge diagnostic setup. This way, the charge dependent response of a scintillating screen determined at the calibration setup can be easily transferred.

As CLS, cylindrical capsules filled with tritium and covered with scintillating material (mb-microtec trigalight T 5419-1/l green) as shown in the inset in figure 3.25 are used. During the absolute charge calibration, the CLS is added to the scintillating screen target wheel to enable direct comparison of screen response and CLS intensity, giving a charge equivalent of the CLS intensity over an integrated observation time. For the specific CLS shown in figure 3.25, for Konica Minolta OG 400, hundred milliseconds of CCD integration time for the CLS is found to be equivalent to 0.485 pC, or $N_{scint}/N_{CLS,100\,ms}\,Q^{-1} = 2.06\ [pC^{-1}]$.

For charge calibration of the spectrometer multiple CLS' were used in order to cover the large scintillator screen range. Each CLS is individually calibrated. These values are given in table 3.2. Differences in intensity exists even though these tritium filled capsules are originating from the same batch. Although the tritium decay is well defined, the scintillating material decay is not. For this reason CLS cross-calibration between the lanex calibration setup and LPA electron spectrometer should be done within a short time window. For the case presented here cross-calibration was performed within one month. After long time periods it is required to recalibrate the CLS' against a master light source[11].

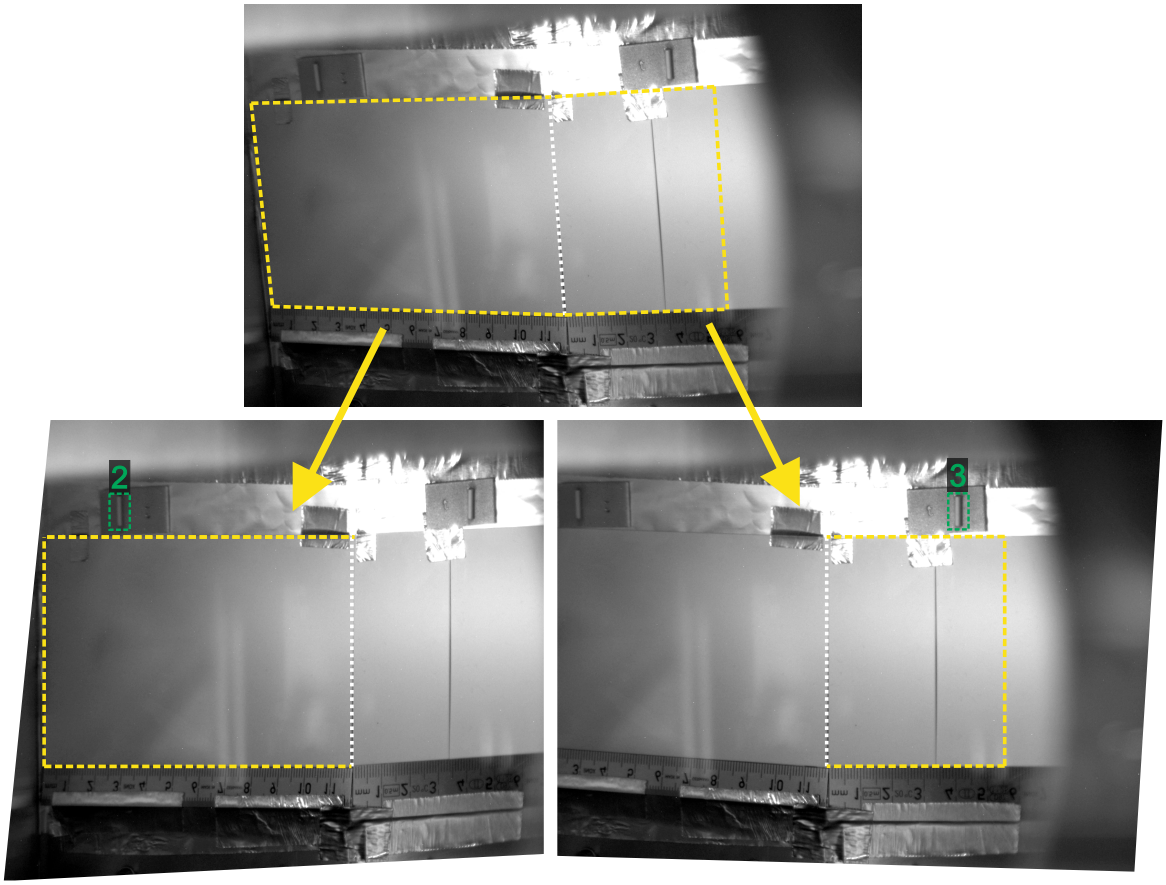

Figure 3.27.: **Correction of perspective distortion.** The original camera image (*top*) covers two different scintillating screen sections. The border between both sections is indicated by the dashed white line. Each section requires a separate spatial transformation(*bottom*). After transformation, images can be stitched together (see figure 3.28). CLS' (highlighted by green dashed boxes) are positioned next to the scintillating screen for charge calibration.

3.5.6. SCINTILLATOR SCREEN IMAGING & CORRECTIONS

The spectrometer scintillator screen measures 658 millimetres in total length, subdivided in three sections under different angles (see figure 3.22). Due to the large size and construction restrictions, a total of four cameras (Basler acA-1300-30gm) is required because screens cannot be imaged perpendicular. Viewing angles and the large imaging area cause perspective distortion, which has to be compensated by applying spatial transformations to the camera images. This process is illustrated in figure 3.27 for a low energy region of the spectrometer. This camera (A) covers the entire first section (up to 24 MeV) and part of the second section (up to 42 MeV) of the scintillator screen. Two separate geometric transformations are performed for each section. The region of interest (ROI), i.e. the scintillating screen, is indicated with the yellow dashed line. The CLS' used for charge calibration are highlighted by the green dashed boxes.

Performing this process for each camera (A to D) and section, these images are combined to cover the entire energy range, as is shown in figure 3.28. This image shows the scintillating screen within the yellow dashed lines (not illuminated) and the CLS' (2 to 8 from table 3.2) positioned for cross-calibration.

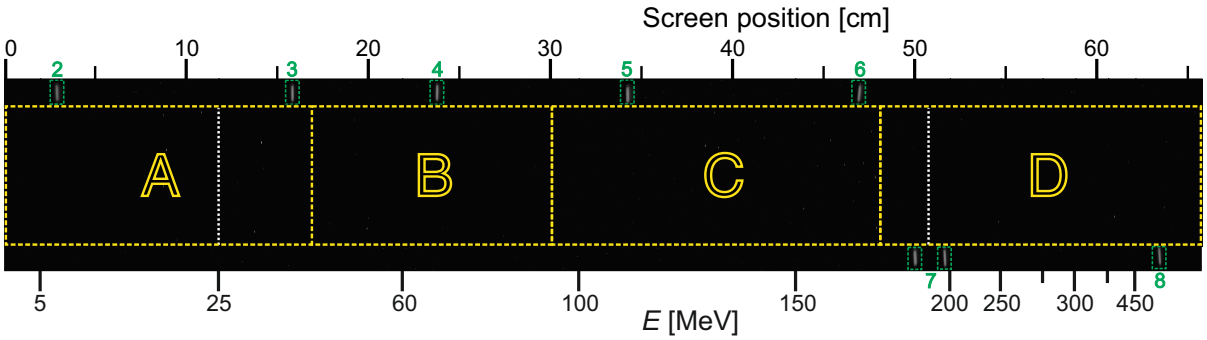

Figure 3.28.: **Representation of the stitched scintillator screen.** After perspective distortion correction, camera images (A-D, yellow dashed lines) are combined. Scintillator screen section borders are indicated by white dashed lines. Camera area A corresponds to figure 3.27. CLS' (green dashed boxes) are positioned next to and along the scintillator screen for charge calibration.

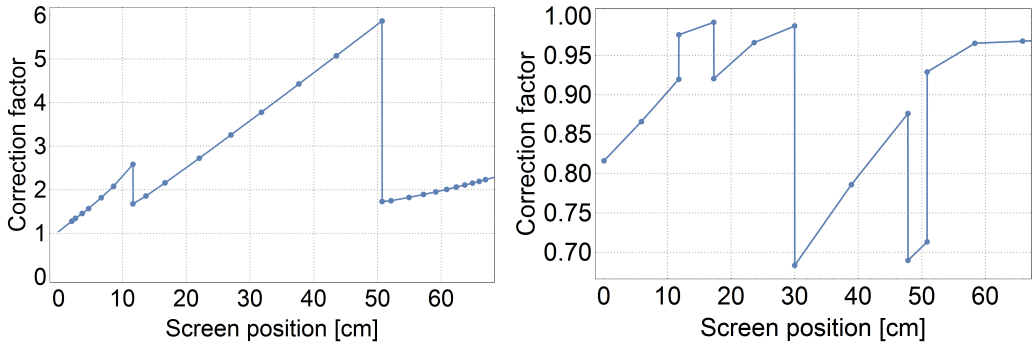

(a) Electron incident angle correction factor. (b) Camera viewing angle correction factor.

Figure 3.29.: **Charge correction factors.** The measured signal on the scintillator screen needs to be divided by a position-dependent correction to correct for electron incident angle and camera viewing angle.

Before the energy-charge distribution can be determined two further corrections have to be applied.

First, the interaction angle of the electrons with the screen is not perpendicular and not equal across the screen as can be seen in figure 3.22. The non-perpendicular interaction causes an increase in signal due to the longer interaction length by a factor $1/\cos(\varphi)$. Using the trajectories found in GPT particle tracing (section 3.5.3), the interaction angle φ is determined. Figure 3.29(a) shows the correction factor for each position on the lanex screen. The measured signal is divided by this correction factor to correct for the electron incident angle. The shallow angle of the electrons at the end of second section of the screen (up to 180 MeV) causes an interaction length of up to 5.9 times compared to normal incidence. The two steps, at 11.8 & 50.8 centimetres, corresponding to 24 & 180 MeV, are related to the section borders of the scintillator screen, where the screen angle and thus incident angle undergoes a step change.

A second correction factor has to be applied for the observation angles of the cameras. The scintillating screen can be approximated as a Lambartian radiator[153], i.e. an ideal diffusive radiating surface where the observed intensity under an angle θ follows a $\cos(\theta)$ dependence. By determining the camera viewing angles for different screen

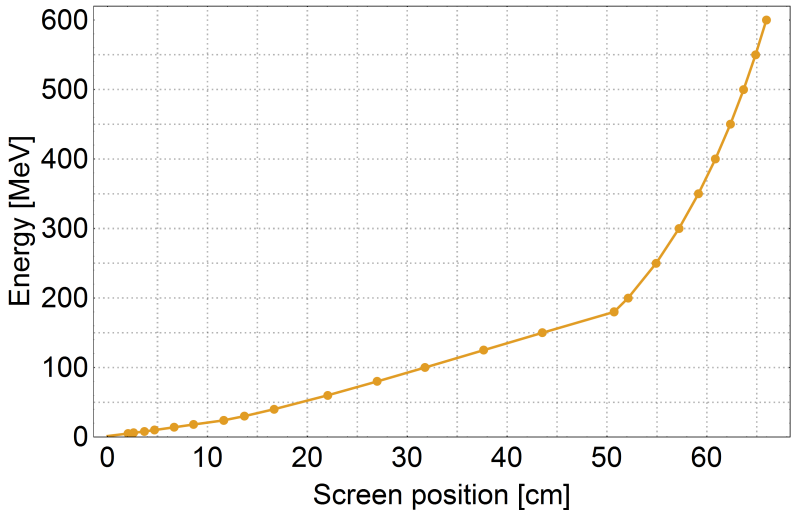

Figure 3.30.: **Spectrometer scintillating screen position to energy dependency.**

positions the required correction factor is determined and shown in figure 3.29(b). Here, the non-normal viewing angle leads to a reduction in signal. Again, the measured signal is divided by this correction factor to correct for the viewing angle.

Finally, the screen position has to be translated to the corresponding energy. Again using electron trajectories found in GPT particle tracing, this correlation is shown in figure 3.30. For the first two sections of the spectrometer, up to 24 MeV, and from 24 MeV to 180 MeV, this function is roughly linear. After 180 MeV, for the third section of the screen, imaging is abandoned and the function no longer follows a linear dependency. The different screen angle causes a sudden increase of energy bin density (ΔMeV/cm), which increases further towards higher energies.

4. IMPROVED PERFORMANCE OF LWFA BY TAILORED SELF-TRUNCATED IONISATION INJECTION

In this chapter the plasma accelerator is introduced, detailing on tailoring of the self-truncated ionisation injection (STII) method to reach high-charge quasi-monoenergetic operation. Ionisation induced injection is a simple and efficient scheme that is able to load large quantities of charge into a wakefield, but generally suffers from continuous injection as long as the laser intensity is sufficiently high to ionise the used dopant gas species and a correspondingy large energy spread. Since the first demonstration of the ionisation injection scheme in the blowout regime 2010 by McGuffey et al.[105] and Pak et al.[104] several approaches to prevent continuous injection have been proposed.

The use of dual-stage targets only provides a dopant over a limited length injector stage, while the main acceleration stage takes place in an undoped gas[154,155]. In shock assisted ionisation injection, a sharp density step limits the region in which ionised electrons can be trapped[156].

The STII scheme is a concept utilising the evolution of the plasma cavity and associated trapping conditions following the nonlinear evolution of a laser pulse in a plasma to limit the injection time[109,110,157]. This scheme is a straightforward adaptation of the traditional ionisation injection process, strongly reducing the energy spread due to the limited injection time. However, until now it was not possible to combine the high charge seen in traditional ionisation injection with the low energy spread characteristic to the STII process.

The tailored scheme presented in this chapter succeeds in combining short injection time with a high charge. In previous experiments, self-truncation in STII is achieved by focussing an unmatched spot, i.e. a laser spot size larger than the plasma wavelength, at the beginning of the gas target[109–111,157,158]. In this case the point of injection is determined mostly by the focussing geometry and as such occurs directly at the entrance of the gas target. In the work presented here, the STII scheme was tailored by combining the relativistic self-focussing effect[65] with the original laser focussing geometry to achieve injection and subsequent truncation. In this scenario the original laser vacuum focus is positioned about a Rayleigh length into the gas-jet target. Laser-plasma

interaction starts in the intermediate field where the laser spot size is considerably larger than the vacuum spot size. Ensuring that the critical laser power for self-guiding according to equation (2.14) is reached, i.e. $P \geq P_c$, relativistic self-focussing enhances the geometric focussing of the beam, tightening the focus. During this evolution process the wakefield is initially formed in the weakly non-linear regime with a large transverse size. As the laser beam focusses further, increasing the laser strength parameter a_0, the characteristic bubble shaped wakefield is formed several millimetres after initiation of the laser-plasma interaction while simultaneously the ionisation threshold for the dopant gas is reached, enabling electron injection into the wakefield. As the laser spot-size and bubble structure keeps developing, the pseudo-potential difference ($\Delta\Psi$) between the point of dopant ionisation and the rear of the bubble continuously evolves. The further increase of laser intensity shifts the point of ionisation forward in respect to the bubble, reducing $\Delta\Psi$ until the trapping condition is no longer fulfilled and injection self-terminates.

The main advantages of this tailored scheme are its ability to generate a large amount of charge with a low energy spread and very robust and stable accelerator operation. It enabled the first demonstration of a quasi-mono-energetic nanocoulomb-class laser plasma accelerator in the beam loading regime as presented in this chapter. Its stability and tunability allow for a systematic study of the beam loading regime, which will be presented in chapter 5.

In this chapter the prerequisites necessary to operate an accelerator in this tailored scheme as well as the injection dynamics are discussed in more detail. All results presented in this chapter are obtained using the 3 mm gas target as described in section 3.4.4. In section 4.1 the specific stringent laser requirements are considered. In section 4.2 the focus geometry and its influence on the accelerator's performance is discussed. A comparison with operation in pure helium is given in section 4.3 to experimentally exclude operation in the self-injection regime. An overview of the typical performance and stability of the accelerator in the nanocoulomb range is given in section 4.4. In section 4.5 the injection dynamics, specifically on the point of injection and truncation, are investigated using Particle-in-Cell simulations.

4.1. LASER OPTIMISATION FOR THE TAILORED STII SCHEME

In order for a laser-plasma accelerator to successfully operate in the tailored STII scheme, some stringent requirements on the laser beam quality exist. As the chirped pulse amplification (CPA) technique is used in order to achieve high-energy, ultra-short laser pulses (see section 3.3), extra care has to be given to properly control the spatio-temporal shape of the beam by the angular chirp (section 4.1.1) and the spectral phase (section 4.1.2). Furthermore, as the laser-plasma interaction starts before the laser vacuum focus is reached, a good laser beam quality is highly required not only at the focus, but also in the intermediate field, as is discussed in section 4.1.3.

4.1.1. ANGULAR CHIRP

Angular chirp is the effect where different spectral components of the laser propagate under slightly different directions, leading to a tilted pulse front in the near field and a reduction of intensity in the focus. Due to the complexity of a CPA laser system, an angular chirp can be easily obtained. Even a small misalignment in the parallelism of the compressor grating will cause the introduced angular dispersion required for bunch compression not to be fully compensated. Such an angular chirp will result in a spatial variation of the spectral shape across the near field of the beam. If, as in LWFA experiments, the beam is tightly focussed, an angular chirp will translate to a spectral separation in space. This has several consequences affecting the accelerator's performance.

The focal spot will become enlarged in the direction of the spectral separation. This leads to a non-ideal oval spot-size instead of the desired circular spot optimal for driving a bubble shaped wakefield. Additionally, the overall increase in spot size will lead to lower spatial peak intensity.

Another effect due to spectral separation at the focus is that at any specific point the spectral width is reduced, leading to a temporal pulse broadening. This decreases the temporal peak intensity and causes the laser to occupy a longer portion of the bubble, potentially no longer fulfilling the $c\tau_l \leq \lambda_p$ condition as discussed in section 2.5.

Although in some specific cases an angular chirp can be purposefully introduced[159,160], this is generally to be avoided. The non-ideal spot size can lead to an asymmetric unstable cavity while the temporal and spatial broadening lead to a lower peak intensity.

EXPERIMENTAL MINIMISATION OF THE ANGULAR CHIRP

For the experiments presented in this thesis, as the first step, the angular-chirp was minimised to less than 1 µrad per nm as measured by a spectrally-resolved inverted field interferometer[161,162] by adjusting the tip-tilt and grating's groove orientation of the compressor. However after optimisation a spectral separation was still observed in the laser focal plane as is shown in figure 4.1, indicating an error below the instrument resolution limit. Figure 4.1(a) shows that the laser spot at the focus is elongated in one direction. Using bandpass filters to select only a part of the spectrum, sub-figures 4.1(b)-4.1(d) show that for a limited spectral bandwidth circular intensity profiles are visible. The elliptical profile observed in figure 4.1(a) is therefore due to spectral separation caused by an angular chirp of the beam.

This remaining angular chirp can be eliminated by further manual fine-tuning of the compressor grating orientation resulting in a circular beam profile at the focus as is shown in figures 4.1(e)-4.1(h). Thus a vacuum focal spot size of 20 µm FWHM is reached, nearing the diffraction limit for a Gaussian beam distribution.

4.1.2. PERFORMANCE INFLUENCE OF THE LASER SPECTRAL PHASE

Before compression, during the amplification process, the laser pulse propagates long distances through air and through bulk material of optics. As different wavelengths have different group velocities in media and the the laser pulse has a non-zero bandwidth, the

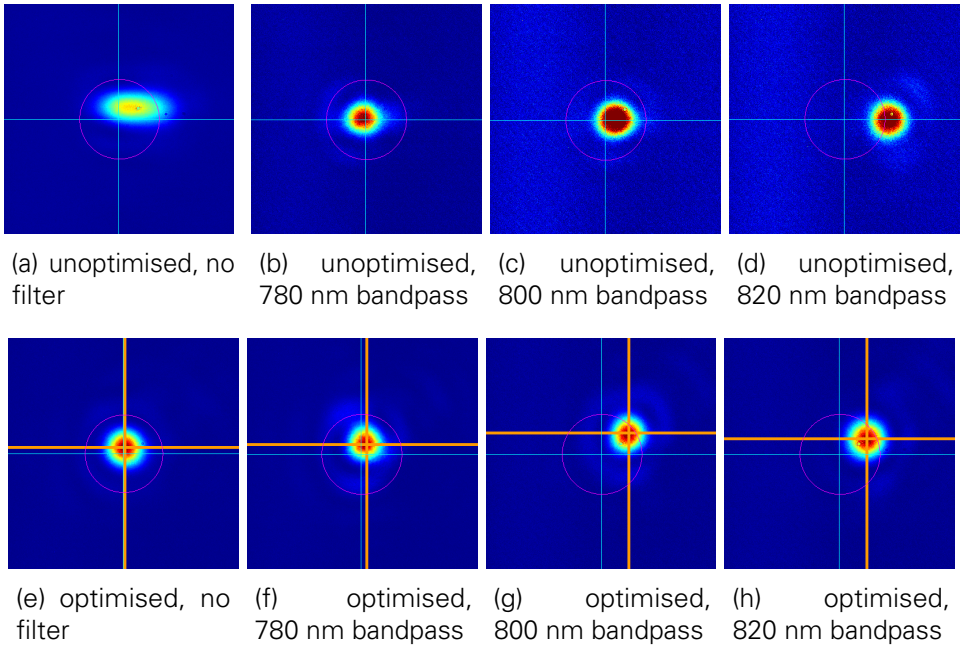

(a) unoptimised, no filter | (b) unoptimised, 780 nm bandpass | (c) unoptimised, 800 nm bandpass | (d) unoptimised, 820 nm bandpass

(e) optimised, no filter | (f) optimised, 780 nm bandpass | (g) optimised, 800 nm bandpass | (h) optimised, 820 nm bandpass

Figure 4.1.: **Effect of angular chirp on the laser intensity profile at the focus**. *(a)-(d)* show the laser profile after angular chirp optimisation with the spectrally-resolved inverted field interferometer. *(e)-(h)* show the laser profile after further fine tuning of the compressor grating alignment. Bandpass filters are used to select only a part of the laser spectrum and have a FWHM bandpass region of (10 ± 2) nm.

spectral phase is influenced, distorting the laser pulse. Although low order polynomial distortions can be compensated by compressor settings, non-linear contributions cannot.

In order to correct for these distortion the spectral phase is measured with a self-referenced spectral interferometry[163] (WIZZLER-Fastlite) and optimised in a closed-loop using an acousto-optic programmable dispersive filter[164] (DAZZLER-Fastlite). A spectral-phase interferometry for direct electric-field reconstruction[165] (SPIDER-A.P.E.) was used in parallel as an extra diagnostic.

However it was found that after this optimisation, additional manual adjustment of the spectral phase by tuning the dispersive filter was required for an optimal accelerator performance. Figure 4.2 shows the accelerator's performance for several adjustments of the group velocity delay introduced by the dispersive filter. Figure 4.2(e) shows the accelerator's performance after closed-loop optimisation without any additional manual adjustment. Although the accelerator produces mono-energetic high-charge beams, shot-to-shot reproducibility is poor. When the GVD is adjusted with a negative value, where the shorter wavelengths travel ahead of the longer wavelengths, the accelerator performance further deteriorates. As can be seen in figure 4.2(f) the energy spread increases with the extension of a low energy tail in the energy spectrum while simultaneously the maximum attained energy decreases. In contrast, adjusting the GVD to positive values leads to an improvement of both beam quality as well as shot-to-shot reliability with an optimum found at an adjustment of +200 fs^2 (figure 4.2(c)). Increasing the GVD beyond this optimum results in dispersion overcompensation, resulting in a deterioration of the accelerator performance (figures 4.2(a) - 4.2(b)). Tuning of the third-order dispersion (TOD) has also been explored, but shows a less significant effect.

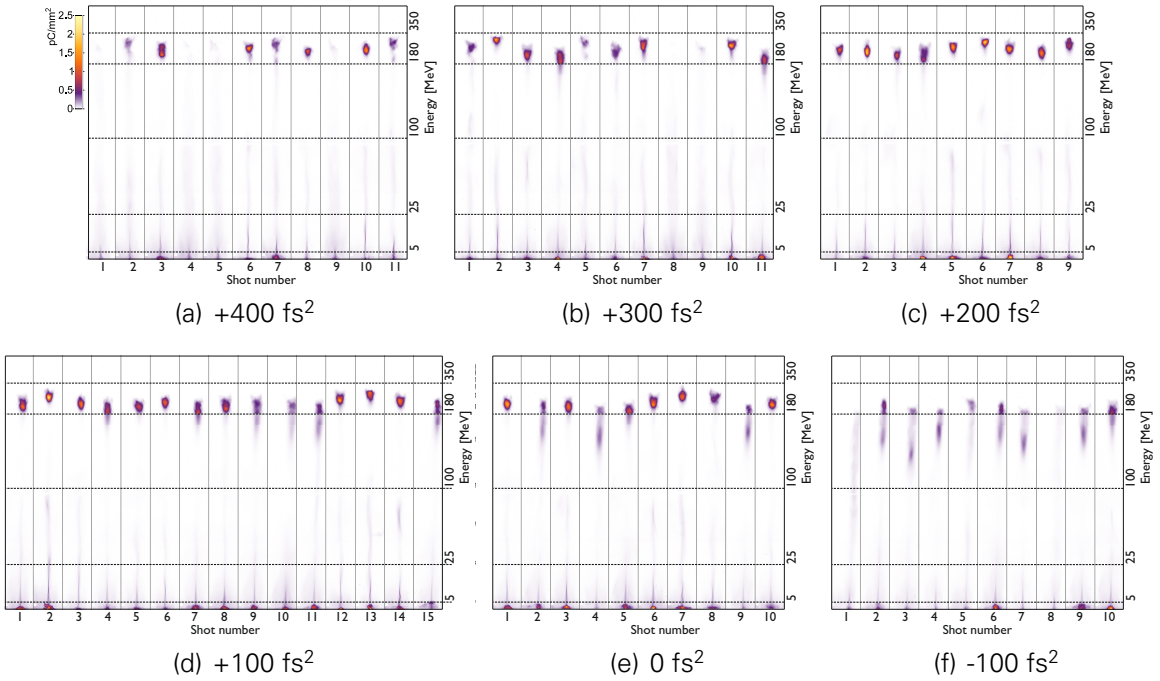

Figure 4.2.: **Influence of adjustment of the GVD on the accelerator performance.** *(e)* shows the performance after optimisation by the WIZZLER-DAZZLER loop and SPIDER-A.P.E. *(a)-(d) & (f)* show the accelerator performance after a manual adjustment of the GVD relative to (e) using the DAZZLER. Shown are consecutive shots obtained at a plasma density of 3.1 $\times 10^{18}$ cm^{-3}, 1% nitrogen doping, a laser energy of 2.5 J and the vacuum focus position located at 1 mm behind the gas jet entrance.

There are several effects which can play a role in the observed accelerator behaviour by influencing the GVD and/or the associated acceleration dynamics.

For example, the optimisation of the spectral phase measured by self-referenced spectral interferometry is done in the laser lab instead of at the experimental area, taking another optical pathway. After compression only reflective optics are used, which are generally equipped with a so-called 'ultrafast' coating. Such coatings are designed to minimise its influence on the spectral phase. The mirrors used in the experimental beamlines are generally specified to add (wavelength-dependent) a maximum of ±15 fs^2 GVD with the OAP coating not having a maximum influence on the GVD specifically specified, although generally intended for use with short laser pules. Cumulative, these small additions of GVD over multiple coatings require an additional manual adjustment.

This does not per se mean that the optimal performance of the acceleration process at +200 fs^2 constitutes the shortest vacuum laser pulse length. In the LWFA proces itself, the interaction with a plasma has a significant effect on the laser pulse, which can be considerably compressed while strong self-phase-modulation occurs[166–168]. Applying adjustments to the spectral phase, modifying the spectral shape of the laser pulse before the laser-plasma interaction, significantly affects the laser development and plasma wakefield dynamics, therefore influencing final electron beam parameters. A positively (negatively) chirped laser pulse tends to be compressed (stretched) during the laser-plasma interaction, thus increasing (decreasing) the maximum accelerating

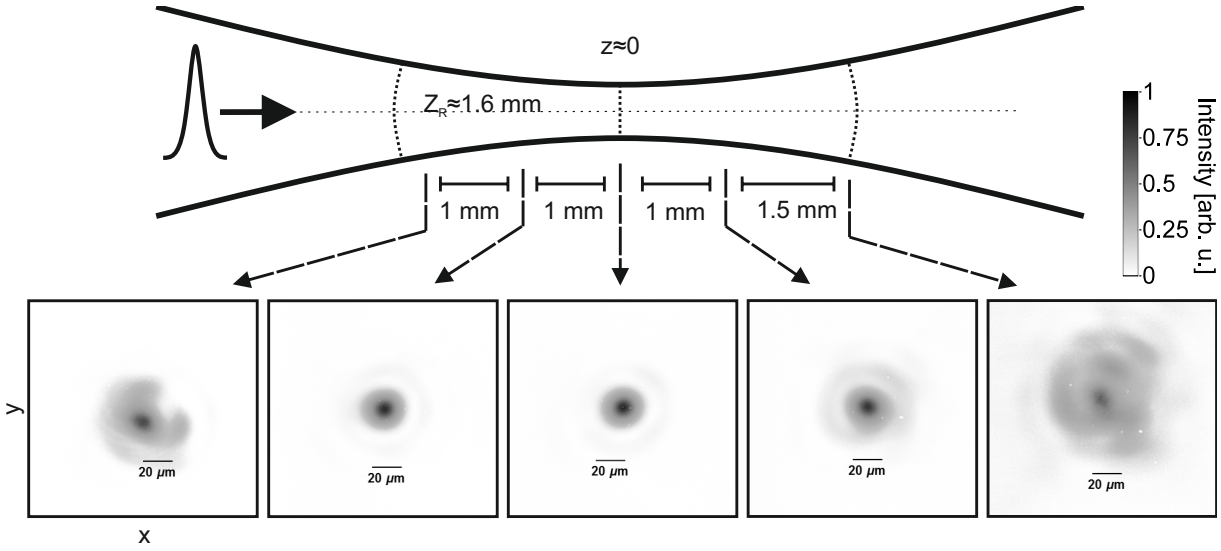

Figure 4.3.: **Laser beam profile in vacuum at various positions around the focus**. The profile was acquired with all laser amplifier stages fully pumped under experimental conditions and after phase optimization in a closed-loop using an acousto-optic programmable dispersive filter (DAZZLER-Fastlite). At the focus a spot size of 20 μm FWHM is reached. About 76% of the laser energy is within the beam waist ($1/e^2$ of peak intensity), corresponding to a strehl-ratio of 0.9.

field gradient of the wakefield[169,170]. The positive effect of a positive GVD adjustment on the acceleration is also observed in experiments performed in other regimes[171,172].

Furthermore, the required adjustment can also be explained by the spectral phase not being constant across the beam. This is strongly suspected, as auto-correlator measurements across the beam have revealed a longer pulse length at the beam edges compared to its centre. This is an effect which can be explained by transmissive optics within the laser beamline, e.g. lenses, having different optical path-lengths across the beam. Both the SPIDER and the WIZZLER evaluate the spectral phase at the centre fraction of the laser beam, which means that such optimisation does not guarantee a minimisation of the spectral phase over the entire laser beam. For the complex LWFA process it can be that optimisation of the spectral phase at the centre region of the beam does not lead to optimum performance, but instead an optimisation taking the entire near field into account, e.g. average spectral phase, is required for optimal accelerator performance.

Likely the observed sensitivity of the accelerator performance on spectral phase has its origin in a combination of above-mentioned aspects. Results presented here show the significance of this effect, which cannot be neglected in order to obtain optimal accelerator operation. Although the tuning described above currently suffices to optimise accelerator performance, these results do invite for further diagnostic improvement and research looking into the details of this effect.

4.1.3. LASER BEAM PROFILE

As the interaction with the gas target starts far before the laser focus is reached, in the intermediate field, this scheme requires a high quality of the laser beam profile. Not only the far field, but also the intermediate field of the laser beam needs to have a smooth, e.g. close to Gaussian, intensity distribution. The setup allows laser diagnostics on target while the laser system is running at full power. Using a wavefront sensor (PHASICS SID4[173]) in closed-loop with a deformable mirror, wavefront optimisation is performed, resulting to a vacuum focal spot size of 20 µm FWHM. About 76% of the laser energy is within the beam waist ($1/e^2$ of intensity), corresponding to a strehl-ratio of 0.9. Scanning around the focus, the laser beam profile evolution in vacuum is shown in figure 4.3. Although the energy fraction drops to 62% at 1.5 mm away from the focus position, a Gaussian beam profile is maintained.

4.2. INFLUENCE OF THE LASER FOCUS POSITION

In this tailored scheme of the STII mechanism, the vacuum focus is positioned inside the gas-target. The non-linear self-focussing effect enhances the focussing by geometry, causing the laser beam to reach its focus inside the gas jet, in front of the vacuum focus position. At this point the intensity of the laser becomes intense enough such that K-shell nitrogen electrons will be ionised and injected into the bubble (see section 2.6.1). Subsequent self-guiding of the laser enables acceleration for the remainder of the gas target.

Although the vacuum focal spot of 20 µm FWHM is close to the estimated bubble matched spot size condition (which is 19 µm at $3.1 \times 10^{18}\,\mathrm{cm}^{-3}$ and 15 µm at $5.0 \times 10^{18}\,\mathrm{cm}^{-3}$), the non-linear self-focussing effect leads to a significantly smaller focal spot size in the laser-plasma interaction, fulfilling the unmatched condition required for the self-truncation effect. Continuation of the laser self-focusing and related bubble evolution after the injection threshold inhibits injection of further electrons into the wakefield.

How the laser beam evolves is strongly dependent on the point in the laser intermediate field at which the laser-gas interaction is started. This subsequently influences both the injection mechanism as well as the acceleration process. These influences become clear in figure 4.4, showing the accelerator performance dependent on vacuum focus position. Figure 4.4(a) shows the position of the vacuum focus point overlaid with the gas-jet target. By adjusting the off-axis parabola position, the point where laser-gas interaction starts is adjusted. By positioning the laser vacuum focus ~1.5 mm past the entry of the gas jet as illustrated, the laser-gas interaction starts in the laser intermediate field at 1.5 mm before the vacuum focus position would have been reached.

Optimum performance is achieved at this point, as is shown in figure 4.4(e). Starting the interaction earlier in the intermediate field, i.e. moving the vacuum focus further behind the gas jet, causes a considerable decrease in injected charge. Starting the interaction later in the intermediate field, i.e. moving the vacuum focus back towards the gas jet, causes electron beams with a considerable larger energy spread. The attained electron energy in this case is considerable lower, which counter-intuitively indicates that injection occurs further inside the gas-jet, shortening the acceleration

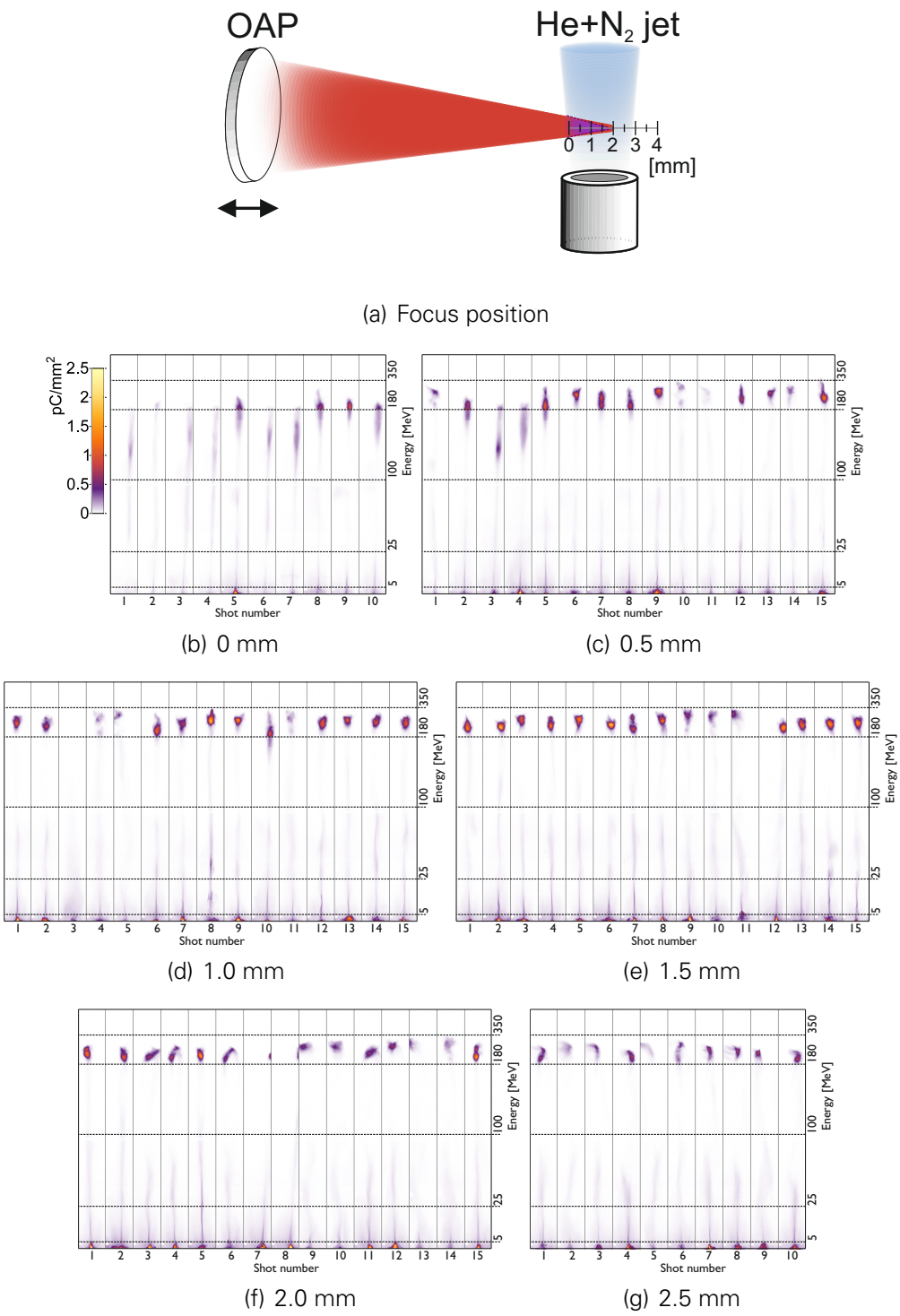

Figure 4.4.: **Influence of the focus position on the accelerator performance**. *(a)* shows the focussing geometry. By adjusting the position of the off axis parabola the position of the (vacuum) focus can be adjusted. The red laser path is the vacuum laser development not taking the self-focussing effect into account. The self-focussing effect is illustrated in purple. *(b)-(g)* show the accelerator performance for consecutive shots for different vacuum focus positions. Results were obtained at a plasma density of 3.7×10^{18} cm^{-3}, 1% nitrogen doping and a laser energy of 2.5 J.

length. However, effects such as beam loading, as will be discussed in chapter 5 or laser-evolution dependent wakefield formation affect the accelerating gradient, thus no decisive conclusion can be made based purely on the observation made here.

Self-focussing being a highly non-linear process, it is not possible to predict the laser evolution analytically. Besides effects in the acceleration dynamics suggested by attained electron energy, the results presented above show a focus position dependent energy spread. Although energy-spread also depends on the beam loading effect, the focus position will influence the laser beam evolution and corresponding bubble dynamics and injection volume, thus influencing energy spread. Specifically, positioning the vacuum focus closer towards the gas jet entrance a larger energy spread is observed, leading to the suspicion of a longer injection length.

Currently no diagnostic tools are implemented that are able to fully diagnose these effects, leaving this effect open to interpretation. Some experimental tools which would be beneficial for gaining more insight into the laser and wakefield dynamics will be discussed in section 4.6.

Meanwhile, particle-in-cell simulations presented in more detail in section 4.5 offer an alternative, giving an insight into laser and wakefield evolution and explaining the fingerprint characteristics of this tailored regime.

Altogether, results presented here are decisively important for the operation of LPAs. They show how a combination of geometric focussing enhanced with relativistic self-focussing leads to stable LPA operation, producing high-charge quasi-monoenergetic beams.

This new regime opens a previously inaccessible mode of operation, enabling systematic studies using reproducible high charge beams. Such a study will be presented in chapter 5, where the accelerator is further tuned using the plasma density and nitrogen doping concentration, as will be discussed in detail in section 5.1, to study the beam loading effect.

4.3. OPERATION AT PURE HELIUM

In order to verify that injection indeed occurs due to the ionisation injection process from the nitrogen dopant, the accelerator is operated at pure helium without a high-Z gas doping present.

Figure 4.5 and 4.6 show spectra obtained in pure helium for comparable experimental parameters (slightly higher laser energy, 3.3 J and slightly lower plasma density, 2.5×10^{18} cm^{-3}) as for the results presented before with the accelerator operating at nitrogen doped helium. A clearly different behaviour as in the STII process can be observed here. No high-energy electrons are present. This is because of the absence of ionisation injection, such that no electrons are injected at the density plateau of the gas target. The low energy tail can be attributed to density-downramp injection at the end of the gas target, leading to a continuous injection which does not reach high energies due to an insufficiency of remaining acceleration length.

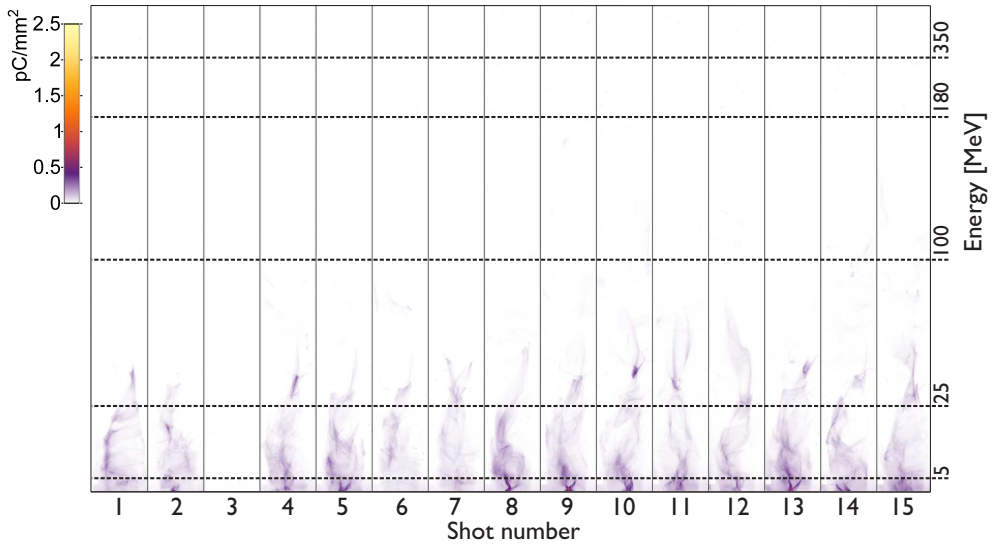

Figure 4.5.: **Energy spectra of 15 consecutive shots obtained in pure helium**. No nitrogen doping is present. Results were obtained at a plasma density of 3.1 × 10^{18} cm^{-3}, a laser energy of 3.3 J and the vacuum position located 1.5 mm behind the gas jet entrance.

4.4. TYPICAL PERFORMANCE OF THE ACCELERATOR

Taking the necessary steps for performance optimisation as described in the previous sections, the typical performance of the accelerator is shown in figure 4.7(a). Depicted is raw data from the electron spectrometer for fifteen consecutive shots. This specific set was obtained with a plasma density of 3.1 × 10^{18} cm^{-3}, 1% nitrogen doping, 2.5 J laser energy in 30 fs FWHM) duration, +200 fs^2 GVD correction and the vacuum focus positioned 1.5 mm behind the gas target entrance.

Figure 4.7(b) shows a line-out of shot number 1 from figure 4.7(a) and illustrates some important parameters which are extracted from each shot. Of each shot the mean peak energy, the maximum attained energy (E_{max}), the FWHM energy spread and the charge within the FWHM of the peak is determined. To determine the E_{max} a lower threshold of 0.1 pC/MeV is used, which is sufficiently above the detector noise level. These values extracted from each individual shot are key parameters required for the systematic study which will be presented in chapter 5. A line-out of all shots shown in figure 4.7(a) can be found in figure 4.8.

At these specific experimental parameters the average mean peak energy of the electron beam is 250 MeV with a mean absolute energy spread (FWHM) of 36 MeV yielding a relative energy spread of 14%. The accelerator delivers an unprecedented average charge within the peak (FWHM) of ∼220 pC with a rms-divergence of this peak of 7 mrad. The low energy tail, which was also observed in pure nitrogen, is attributed to down-ramp injection at the end of the gas jet target. Besides these impressive operational parameters, distinctive of this operational regime is the excellent shot-to-shot stability. The mean peak energy shows only a 9% shot-to-shot standard deviation (SD) and charge is stable with only a 40 pC shot-to-shot SD. This reproducibility gives the ability to perform statistical analysis over multiple shots for each dataset belonging to a specific experimental parameter as will be used for the systematic study of the beam loading effect in chapter 5.

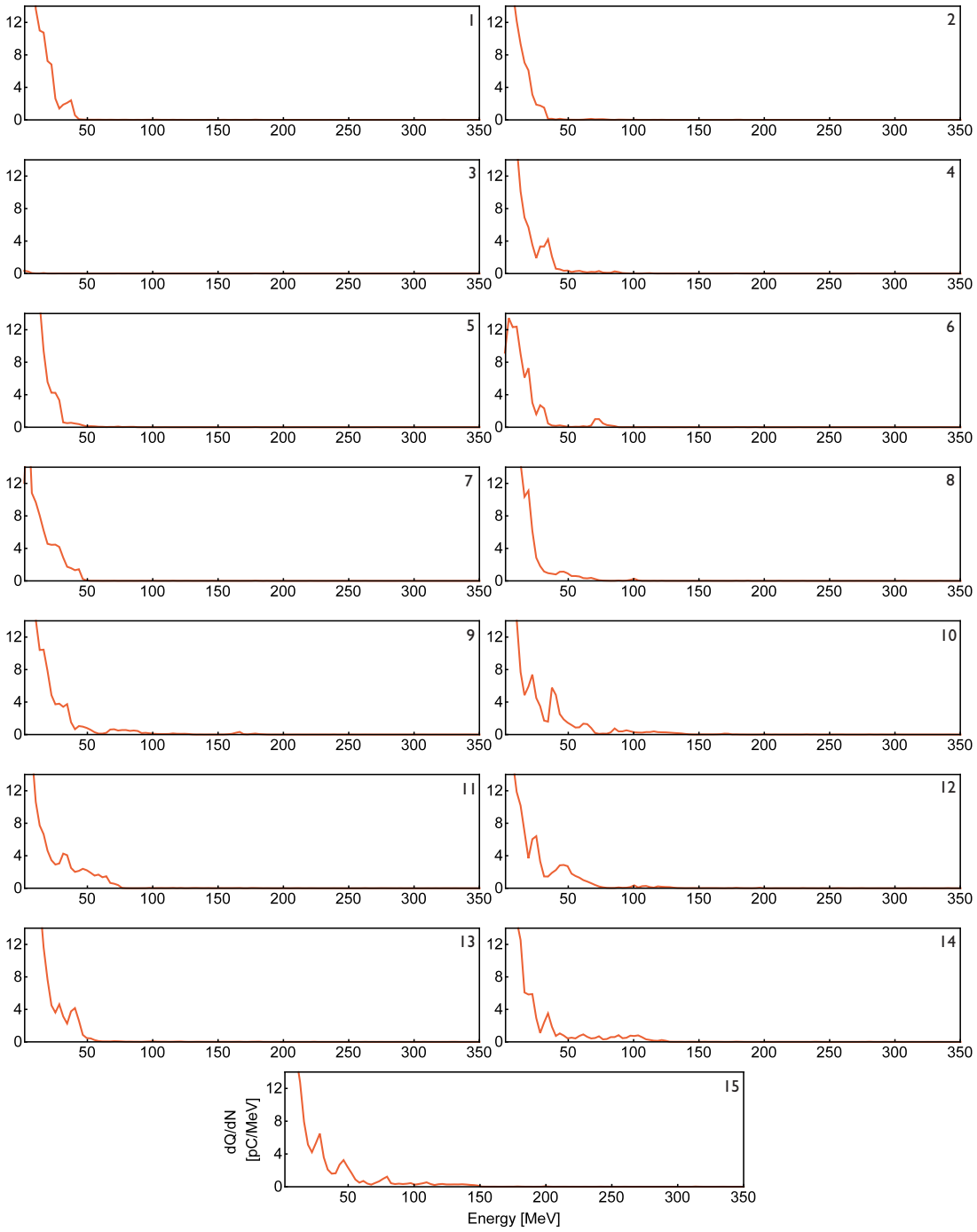

Figure 4.6.: **Energy spectra of all 15 consecutive shots shown in figure 4.5.** Axes labels are equal for all graphs and are shown only in the bottom graph. Shot numbers are shown in the top right of each graph and correspond to the shot numbers found in figure 4.5. Results were obtained at a plasma density of 3.1×10^{18} cm^{-3}, pure helium (no nitrogen doping present), a laser energy of 3.3 J and the vacuum position located 1.5 mm behind the gas jet entrance.

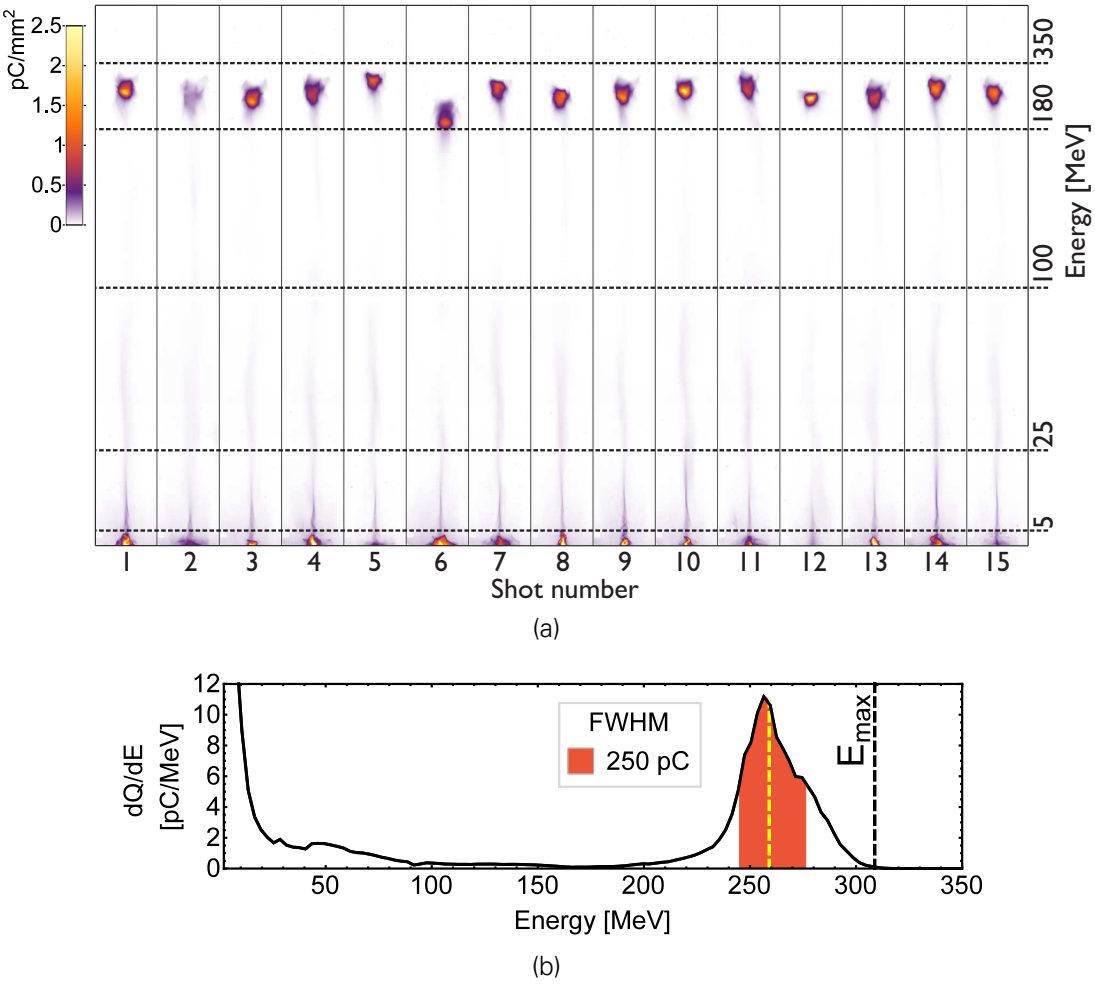

Figure 4.7.: **Energy spectra of fifteen consecutive shots.** *(a)*, raw energy electron spectra. The color map represents the charge density (pC/mm^2) on the detector. *(b)*, Energy spectrum of the first shot from figure (a). The filled area represents the charge within the FWHM, the yellow dashed line represents the mean peak energy, the black dashed line represents the maximum attained energy (E_{max}) at 0.1 pC/MeV. Obtained with super-sonic gas-jet with a 1.6-mm-long plasma density plateau of 3.1×10^{18} cm^{-3}, 1% nitrogen doping, 2.5 J laser energy in 30 fs FWHM duration and the vacuum focus position located 1.5 mm behind the gas jet entrance.

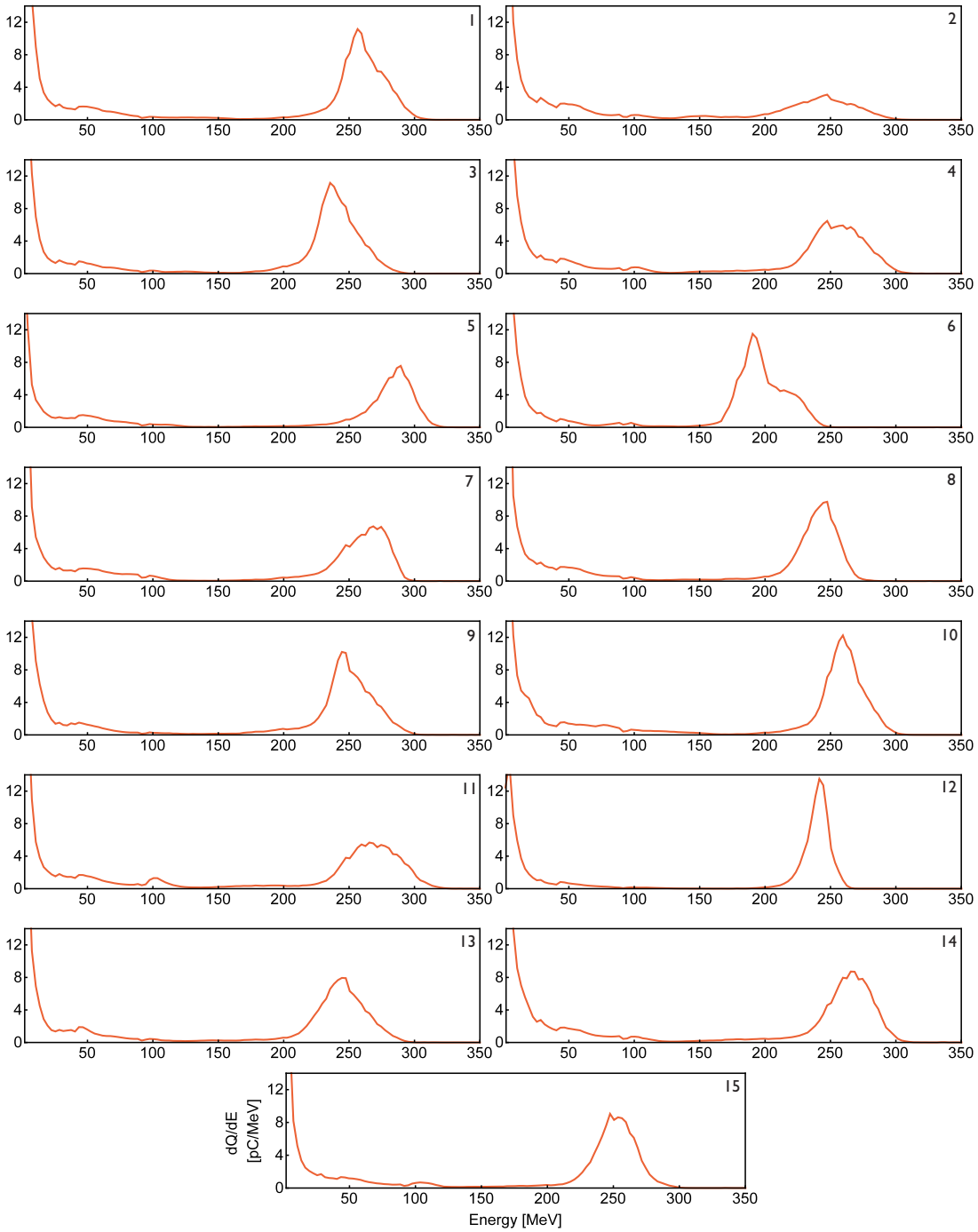

Figure 4.8.: **Energy spectra of all 15 consecutive shots shown in figure 4.7(a)**. Axes labels are equal for all graphs and are shown only in the bottom graph. Shot numbers are shown in the top right of each graph and correspond to the shot numbers found in figure 4.7(a). Obtained with supersonic gas-jet with a 1.6-mm-long plasma density plateau of 3.1×10^{18} cm^{-3}, 1% nitrogen doping, 2.5 J laser energy in 30 fs FWHM duration and the vacuum focus position located 1.5 mm behind the gas jet entrance.

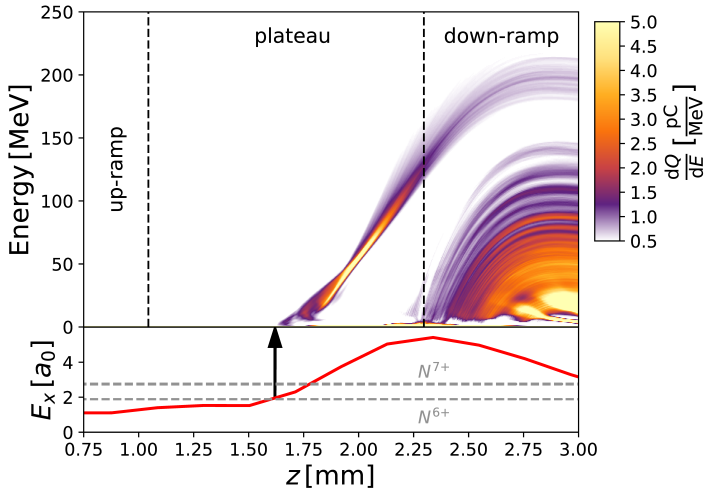

Figure 4.9.: **PIC simulation showing energy evolution during the acceleration process.** The histogram (*top*) shows the evolution of the electron energy throughout the acceleration process. The *bottom* graph shows the evolution of the maximum normalised laser potential with the required potential for barrier suppression ionisation of the nitrogen K-shell electrons. Final injected charge in the peak is 60 pC. Additional injection of both helium and nitrogen electrons occurs in the density down-ramp of the gas-jet, resulting to a low-energy background in the final energy spectrum.

4.5. ACCELERATION DYNAMICS

The experimental results presented in this chapter clearly demonstrate the scheme's potential. However, to gain a full insight into the dynamics of the acceleration process, diagnostic challenges still remain in order to achieve the required spatially small and temporally short resolution.

In the absence of experimental diagnostics with sufficiently high resolution, Particle-in-Cell (PIC) simulations offer an insight into the accelerator dynamics, supplementing experimental results and enabling an insight inside the acceleration process at the required resolution.

Specifically of interest for the tailored STII scheme is to gain insight into the mechanism responsible for the onset and truncation of injection which will be discussed in this section.

Figure 4.9 shows the energy evolution extracted from a PIC simulation[1] set up to closely represent experimental conditions. As input parameters a Gaussian laser pulse was used with a vacuum spot size of $w_0 = 19$ µm and a pulse duration $\tau = 30$ fs (both FWHM of intensity), reaching a vacuum peak intensity with $a_0 = 2.8$. The electron density was modelled according to the measured gas density profile (see section 3.4.4) and was set to reach an electron density after ionisation of $n_e = 2.62 \times 10^{18}\,\mathrm{cm}^{-3}$ at the density plateau. The vacuum focus is positioned at the nozzle exit corresponding to $z = 3$ mm in both figure 4.4(a) and 4.9.

The non-linear self-focussing effect on the laser pulse can be clearly seen in the

[1] More information on the PIC simulations can be found in appendix B

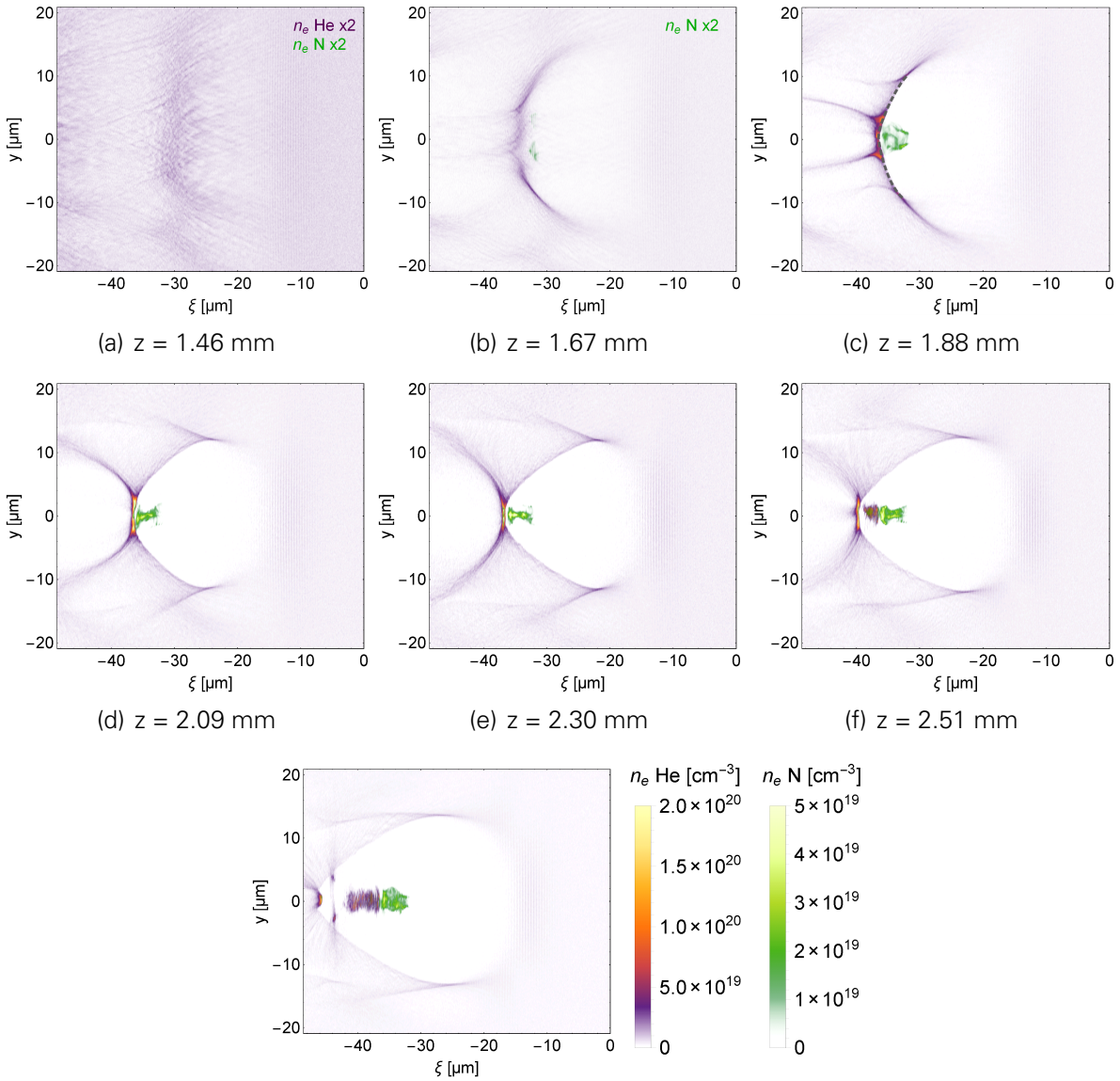

Figure 4.10.: **Electron density distributions.** Results from the same 3-D PIC simulation as shown in figure 4.9, shown are sliced planes through the centre of the bubble perpendicular to the laser polarisation at different time-steps. Separate colour-scales are used for electrons originating from helium *(h)* and from the nitrogen K-shell *(i)*. The dashed curve in figure (c) serves as a guideline in figure 4.11.

evolution of the normalised laser potential shown in the bottom graph of figure 4.9. The focus position shifts forward to around z = 2.3 mm while at the same time a tighter focus is reached resulting in an a_0 = 5 compared to an a_0 = 2.8 reached without the gas target present.

The shift of focus position and increase of a_0 causes the laser intensity to become high enough to cause barrier suppression ionisation (see section 2.1) even before the focus position is reached. This occurs roughly in the centre of the gas-jet, where the laser intensity surpasses the BSI threshold of the nitrogen K-shell electrons (N^{6+} & N^{7+}) at a_0 = 2.21 and a_0 = 2.77 respectively. From the energy histogram shown in the top of figure 4.9 it can be observed that no injection occurs before the ionisation threshold of the nitrogen K-shell is reached. Thus, the point where the ionisation threshold is surpassed coincides with the onset of electron injection into the wakefield as can be seen by the first appearance of relativistic electrons.

After this initial injection, the laser spot evolution continues as indicated by the further increase of the laser field. This process causes truncation of the injection process, resulting in injection to occur only over a short distance. Only as the density down-ramp is reached a secondary continuous injection occurs due to a shallow down-ramp injection as also seen in experiment (section 4.3).

In correspondence to observed experimental results, electrons injected in the initial injection process are accelerated to high energies forming a quasi-monoenergetic peak, while the density down-ramp injection forms a broadband low energy background. The point of injection within the gas-target found in simulation fits well with the experimentally determined effective acceleration length of 0.8 mm as will be discussed in more detail in section 5.2.2.

A more intuitive insight of the bubble formation, its evolution and electron injection can be obtained from the electron density distribution shown in figure 4.10. Here the density distribution is given at different time-steps of the simulation, corresponding to the same z-positions within the gas-target as in figure 4.9. In order to discriminate electrons originating from the nitrogen K-shell and helium originating electrons, separate colour scales are used overlaid on top of each other to show the density distributions. Initially, at z = 1.46 mm, the onset of the wakefield is visible, but no blowout is seen as the required intensity for blowout to occur, $a_0 > 2$, is not yet reached. As a_0 increases by the self-focussing of the laser beam for positions further in the gas-target, a blow-out wakefield forms as a_0 exceeds 2 around z = 1.67 mm. A near-spherical cavity is reached when $a_0 \sim 4$ at z = 2.09 mm.

In figure 4.10(b) the first weak occurrence of electron capturing in the wakefield is observed at two symmetrical off-axis positions. At the next time-step at z = 1.88 mm shown in figure 4.10(c), a large amount of electrons has been injected into the wakefield for acceleration. From figure 4.9 can be extracted that the electrons at this point already exhibit a quasi-monoenergetic energy distribution[2] around 30 MeV, while injection has already been truncated. Electrons injected at this point are exclusively from the nitrogen K-shell, thus confirming the ionisation injection mechanism.

During further propagation the electrons are longitudinally accelerated, while the bunch

[2] A lineout of the energy distribution at z = 1.88 mm is shown in figure 5.9(a) of section 5.5, in which the energy spread directly after injection is discussed.

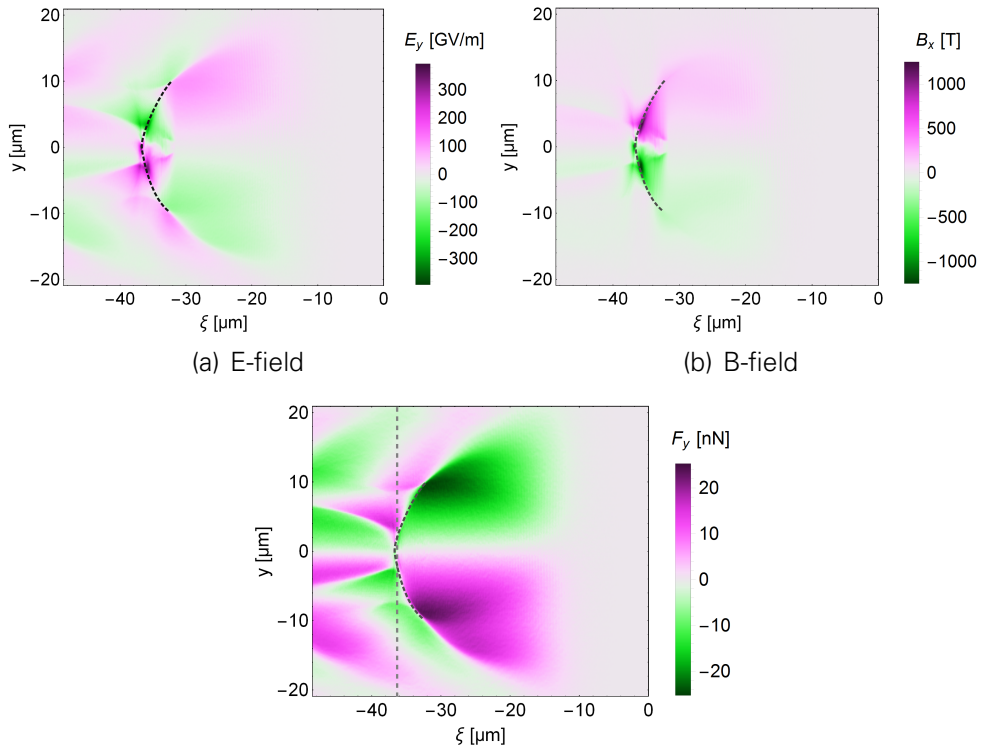

(a) E-field

(b) B-field

(c) Effective focussing force

Figure 4.11.: **Transverse wakefield properties.** Data extracted from PIC simulation in the plane perpendicular to the laser polarisation at z = 1.88 mm. The dashed curve indicates the border of the bubble's electron sheath as shown in figure 4.10(c). *(a)* shows the transversal component of the electric field. *(b)* shows the magnetic field component perpendicular to the shown plane. *(c)* gives the transversal focussing field $F_y = -e\left(E_y \times v_\phi B_x\right)$, assuming an electron moving close to the speed of light in positive z direction. The dashed vertical line indicates the border of the focussing region.

initial large transversal distribution at z = 1.88 mm is compressed by the transversal fields to a small bunch around the propagation axis at the centre of the bubble. After z = 2.30 mm the gas-density down-ramp is reached, where the lower electron density results in an elongation of the bubble. At this point the secondary down-ramp injection occurs. Electrons trapped during this injection originate both from helium and the nitrogen K-shell, with the majority originating from helium due to the helium/nitrogen ratio.

4.5.1. INJECTION & TRUNCATION

Although the data presented above clearly shows injection of electrons originating from nitrogen over a limited period of time, it does not show the physical process behind the self-termination of the injection mechanism. In this section this process is studied in more detail.

As described in section 2.6.1, two conditions have to be fulfilled in order for ionisation injection to occur. Firstly, the longitudinal trapping condition has to be reached. That is, electrons need to gain enough momentum between the point of ionisation and a point

at the backside of the bubble such that its velocity is at least the same as the wake's velocity, i.e. $v_{z,\mathrm{e}} \geq v_\phi$. Equation (2.39) expresses this trapping condition in terms of the wake potential. Secondly, the longitudinal trapping condition has to be fulfilled within a region where a transversal focussing field is present, constituting the transversal trapping condition.

Thus, in order to assess the trapping conditions, one first has to determine the region within the bubble where a focussing force exists. Both the electric and the magnetic field contribute to the transversal force experienced by relativistic electrons according to the Lorentz equation (equation (2.3)). Figure 4.11 shows the transverse wakefield properties extracted from the PIC-simulation at z = 1.88 mm, corresponding to figure 4.10(c). The transverse component of the electric field relative to the direction of propagation is shown in sub-figure 4.11(a). Here, for electrons above the bubble's central axis in the top half region of the figure, the pink region gives a focussing contribution towards the propagation-axis while the green region gives a defocussing contribution and vice versa for the bottom half of the figure. As expected, for the main part of the bubble, a focussing electric field is present. However, in this loaded case the Coulomb electric field of the injected bunch is sufficiently strong such that at the back of the bubble the electric field contributes towards a defocussing force.

In figure 4.11(b) the magnetic field perpendicular to the plane is shown, which is the relevant contribution due to the $\vec{v} \times \vec{B}$ cross-product in equation (2.3). Contrary to the electrical field contribution, the contribution of the magnetic field to the force experienced by an electron depends both on its own propagation velocity and direction. Thus, certain assumptions have to be made at this point in order to evaluate the transversal force exerted on an electron. At the moment that the longitudinal trapping condition is being fulfilled, the electrons have a velocity equal to wake velocity, i.e., $v_\mathrm{e} = v_\phi \rightarrow c$. Furthermore, the assumption is made that the transversal velocity of the electron is neglectable compared to its longitudinal velocity ($v_{y,\mathrm{e}} \ll v_{z,\mathrm{e}}$). Under these assumptions, i.e. for an electron with $v_{y,\mathrm{e}} \simeq 0$ & $v_{z,\mathrm{e}} \rightarrow c$, equation (2.3) is applied resulting in the force field shown in figure 4.11(c).

Therefore, it can be identified that electrons co-travelling with the wakefield close to the speed of light experience a focussing field, even in the presence of a high charge injected bunch. Besides the relevance for fulfilling the injection conditions, this also accounts for the transversal compression of the injected bunch as observed in figure 4.10, overcoming the repulsive forces originating from the bunch's Coulomb self-field.

The border of the focussing region overlaps with the electron density sheath at the backside of the bubble. This is illustrated in figure 4.12, where line-outs of several relevant parameters through the bubble centre along the propagation axis are shown. Note that the wakefield potential minimum can be located further backward, inside the electron sheath, where the transversal trapping condition is not fulfilled.

Concentrating first at z = 1.88 mm in sub-figure 4.12(b), where line-outs show the electron density distributions from figure 4.10(c) with electrons originating from helium represented by the black line and from the nitrogen K-shell by the olive line. The border of the focussing region indicated by the dashed line in figure 4.11(c), is represented by the blue point in figure 4.12(b). The blue line itself representing the wake potential. It can be seen that the ξ position of the focussing region border overlaps with the bubble sheath border represented by the step increase of helium originating electron density. However, the minimum wake potential is located behind this point, within the

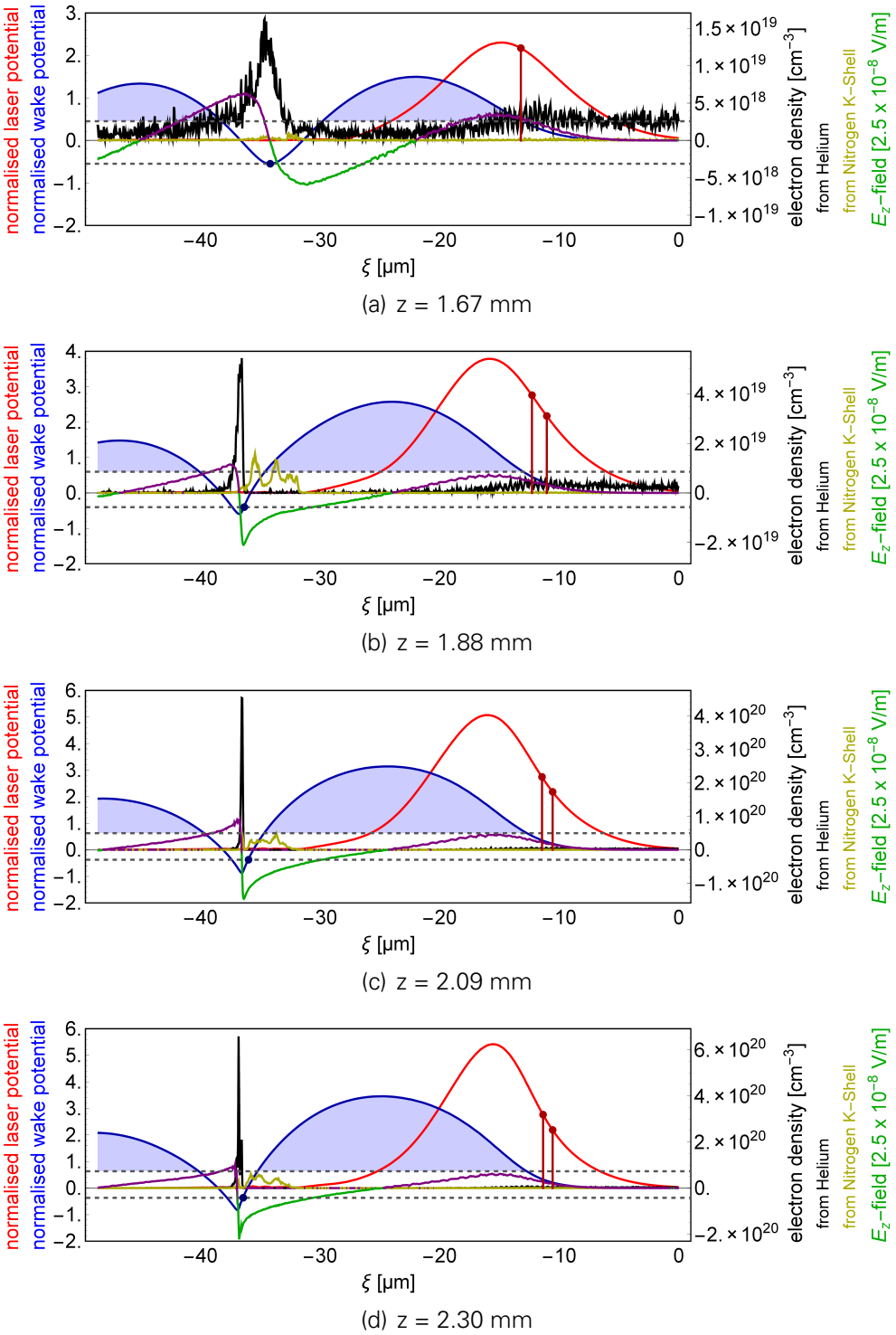

Figure 4.12.: **Wakefield properties.** Data extracted from PIC simulation. Shown is the normalised laser potential a_0 (red line), the wake potential normalised to $e/(m_e c^2)$ (blue line) and the longitudinal accelerating electric field E_z (green/purple line) along the wakefield's central axis. The local electron density is shown both for electrons originating from helium (black line) and from the nitrogen K-shell (olive line). The red points indicate the ionisation positions for the nitrogen K-shell electrons at $a_0 = 2.21$ for N^{6+} and $a_0 = 2.77$ for N^{7+}. The blue point indicates the minimum wake potential within the focussing region of the wake. The region where the wake's potential is high enough for the the longitudinal trapping condition ($\Delta\Psi \geqslant 1$) to be fulfilled is indicated by the blue shaded region.

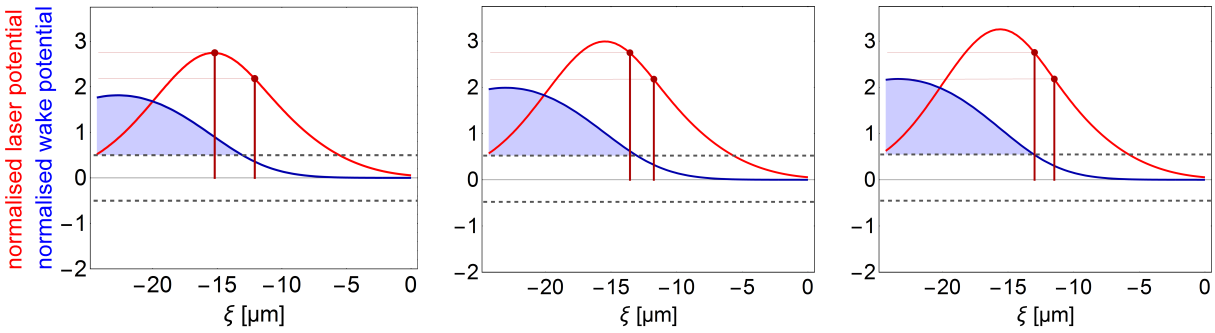

(a) z = 1.73 mm (b) z = 1.77 mm (c) z = 1.81 mm

Figure 4.13.: **Wakefield properties.** Interpolated from PIC data at z = 1.67 and z = 1.88 mm. Shown is the normalised laser potential a_0 (red line), the wake potential normalised to $e/(m_e c^2)$ (blue line) along the wakefield's central axis. The red points indicate the ionisation positions for the nitrogen K-shell electrons at $a_0 = 2.21$ for N^{6+} and $a_0 = 2.77$ for N^{7+}. The region where the wake's potential is high enough for the the longitudinal trapping condition ($\Delta\Psi \geqslant 1$) to be fulfilled is indicated by the blue shaded region.

sheath and within a defocussing region. Thus, the transversal trapping condition is not met at the point where the wake potential is at its minimum. Instead, the longitudinal trapping condition must be evaluated at the lowest potential value still within the bubble focussing region, indicated by the lower dashed line in figure 4.12(b).

From $\Delta\Psi \geq 1$ (equation (2.39)) we can now determine the required lower limit of the wake potential for an electron born at a random ionisation point to become trapped. This lower limit is indicated by the upper dashed line. The region in which the trapping conditions are fulfilled is indicated by the blue shading. Any electron born in this region can potentially be trapped.

From figure 4.12 it can be seen that after injection (figures 4.12(b) - 4.12(d)) ionisation positions of additional nitrogen electrons occur before the trapping region. This is indicated by the red line, which represents the normalised laser potential a_0 and the two points indicating the nitrogen K-shell ionisation thresholds. The first point represents the BSI threshold for N^{6+} at $a_0 = 2.21$ and the second point N^{7+} at $a_0 = 2.77$. As these are the BSI thresholds, the probability of electrons to be ionised is practically one once this threshold is reached. As a consequence, there are no more electrons available for ionisation in the region where the trapping conditions are met. Thus it explains why ionisation injection does not occur over the entire interaction, even though the ionisation threshold is reached.

4.5.2. POINT OF INJECTION

The exact point of initial injection is not captured in figure 4.12. Figure 4.12(a) at z = 1.67 mm, is just at the onset of injection as can also be extracted from figures 4.9 and 4.10. At this point only the ionisation threshold for N^{6+} is reached and located such that the trapping condition is just still fulfilled, while the threshold for N^{7+} ionisation has not yet been reached. At the next timestep at z = 1.88 mm a large amount of charge has already been injected and no further injection occurs. In-between timesteps are

not available, due to computational limits, i.e. high disc-space required to store the full information (so-called "dumps") of simulation snapshots. For this reason snapshots are only available at the presented relative large interval. Thus the exact moment of injection, located in between both time-steps, could not be captured.

Nevertheless, the information extracted at z = 1.67 and z = 1.88 mm gives enough information to deduce the injection mechanism. In-between both time-steps the ionisation threshold for N^{7+} will be reached first at the laser peak intensity. As the laser intensity peak is located within the trapping region, injection will occur at this point. As the laser intensity increases, the position of the ionisation will move towards the front of the laser pulse, leaving the trapping region and terminating injection. This process is indicated in figure 4.13, where the PIC data is interpolated between both data-points from figure 4.12(a) & 4.12(b). From this interpolation it can be estimated that the ionisation threshold for N^{7+} is reached around z = 1.73 mm, at which point injection is started. Injection is expected to occur over a distance of roughly 80 µm before injection self-terminates at z = 1.81 mm.

4.6. DISCUSSION

In this chapter a new scheme of the STII process has been presented. This new scheme has considerable advantages over results previously obtained with the STII process, greatly increasing injected charge while retaining a low energy spread from the truncation mechanism. The performance is found to be very robust, giving high shot-to-shot reproducibility over a large tuning range for both operating density as well as injected charge.

Characteristic of this scheme is the long laser-plasma interaction before injection occurs several millimetres inside the gas jet. This is achieved by placing the vacuum focus several millimetres behind the gas jet entrance. The non-linear self-focussing effect influences the laser evolution and strongly enhances focussing given by the experimental geometry, causing injection to occur under unmatched conditions and fulfilling the truncation condition. This in contrast to previously established operation of the STII process, where an unmatched spot is focussed at the start of the gas jet. In that case, self-focussing is not utilised to reach the point of injection and only ensures laser confinement for the remainder of the acceleration.

This new scheme places stringent conditions on the laser quality due to the long non-linear interaction before injection occurs. Specifically the laser beam profile in both the far- and intermediate field, the angular chirp and the spectral phase require detailed optimisation.

Results from PIC simulations give a good insight into the physical dynamics attributing to this mechanism. They show the effect of non-linear self-focussing and explain the injection mechanism and its self-termination, thus clarifying the fingerprint features of this tuned STII scheme. However, many questions regarding the accelerator, both from simulation as well as from an experimental view, are still open for further research.

Evaluation of PIC results regarding the injection and self-termination mechanism presented here has been done on 1-D outlines under specific assumptions. Although this is a good approximation and gives a good insight into the mechanism, the full

three-dimensional problem is more complex. Furthermore, the current state-of-the-art PIC simulations of LWFA rely on a number of approximative models, with currently no code having exact predictive modelling in existence. Improvement of such codes, including the implementation of the non-ideal higher-order Gaussian laser beam profile is challenging and at this moment still an ongoing effort.

Meanwhile, the resource-intensive nature of PIC simulations has prevented large parameter scans. Increasing resources or optimising the simulation process would allow for detailed investigation of further parameters, gaining further insight into for example the focussing dynamics discussed in section 4.2.

Additionally, further development of simulations in the form of the addition of several tools are desirable in order to avoid certain assumptions made in this chapter. Initially the ability to pinpoint the ionisation point of injected electrons, and ultimately the ability to fully trace trajectories of injected and, after truncation, rejected electrons would be a valuable tool. This would eliminate the need of determining the focussing region under the assumption that electrons are born at rest and gain no transverse momentum. Instead, all transverse and longitudinal dynamic effects, originating both from E- and B-fields over the entire trajectory traversed by an electron from the point of ionisation to trapping would be included, thus leading to a more accurate determination of the injection region.

From the experimental side further investigation on the influence of the spectral phase, to which the accelerator's performance was found to be strongly sensitive, would be of interest. These influences are currently not assessed in PIC simulations, but have a big impact on the acceleration process, as is discussed in section 4.1.2. The group velocity delay can be easily tuned for performance optimisation, but its physical influence will be the subject for further investigation. There are strong indications for a spatial variation of the the spectral phase across the beam. Currently the spectral phase is assessed and tuned only for the centre of the laser beam. The spatial variation of the spectral phase across the beam should be studied in more detail to gain a better insight into the mechanism. With the gained knowledge it might subsequently be possible to increase the accelerator's performance further by applying a position dependent spectral phase correction across the laser beam.

To further understand the bunch and bubble dynamics, it would be beneficial to increase the quality of the wakefield diagnostics. Specifically valuable would be the ability to probe the evolution of the wakefield and injected bunch. This is a challenging task, seen the stringent conditions on spatial (∼µm) and temporal (∼fs) resolution in a bright broad-bandwidth background environment from laser scattering mechanisms and plasma recombination afterglow.

There are several techniques that are able to provide such a desired diagnostic. Using a combination of time-resolved polarimetry with plasma shadowgraphy as has been shown by Buck et al.[35], it is possible to probe the magnetic field created by both the wakefield and the bunch. A technique introduced by Li et al.[174] uses a stretched pulse probing the wakefield under an oblique angle imaged to an optical frequency-domain streak camera which enables single shot time-resolved diagnostics of the wakefield. A recently proposed and demonstrated technique by Zhang et al.[175,176] uses a femtosecond relativistic electron probe to reach higher spatial resolution and signal sensitivity as before-mentioned methods.

Implementation of these techniques would allow for the visualisation of the injected bunch and its influence on the wakefield. This would enable further studies and strongly contribute towards the understanding of the working mechanisms of the new STII scheme presented in this chapter.

As discussed earlier in chapter 1, peak current is a decisive aspect for the application of LPA electron bunches. In order to determine the peak current of the accelerator it is necessary to know, besides the bunch charge, the bunch length. However, due to the ultra-short nature of these bunches, to measure them is a non-trivial task.

One method is to measure the longitudinal extend of the bunch magnetic field by a combination of polarimetry and shadowgraphy.[35,177] This method allows for direct observation of the bunch within the wakefield, however relies on averaging over many shot for bunch length determination. This method has been demonstrated, measuring ~6 fs FWMH bunches[35], but does not have the resolution to reveal in sub-structures within the electron bunch.

A second method is using transition radiation. For this method a dielectric foil is positioned in the electron bunch path (see section 3.2, figure 3.3). As the electron bunch traverses the boundary between the foil and vacuum, it emits transition radiation with a wavelength distribution dependent on its time-structure. For wavelengths much larger than the longitudinal bunch distribution, contributions from individual electrons are emitted in phase and add up coherently, whereas wavelengths shorter than the bunch length add up incoherently. This results in the coherent (longer wavelengths) radiation being more intense than the incoherent (shorter wavelengths) radiation. By measuring the emitted spectrum the longitudinal bunch distribution can be reconstructed[178]. A large bandwidth spectrometer, covering both the coherent and incoherent part of the spectrum, is required to achieve a sufficiently high temporal resolution, such that both bunch envelope as well as bunch fine structures can be resolved. CTR has been demonstrated at terahertz frequencies to diagnose electron bunches longer than 30 fs[179,180], while at the other end of the spectrum at near-infrared to visible wavelengths bunch structures of 4.4 fs have been measured[36].

Parallel to the PhD project reported in this thesis, a broadband transition radiation spectrometer for single shot longitudinal electron bunch diagnostic is being implemented by Omid Zarini as part of his PhD project. This spectrometer is able to resolve both the short and long time-structure of electron bunches within a single shot, covering the visible and mid-IR range (200 nm - 12 µm), i.e. a frequency range of 5.9 octaves[181]. This enables an associated time-resolution down to ~0.4 fs for resolving bunch fine structures, while still being able to resolve bunch envelopes up to 30 fs. Some initial findings from this diagnostic will be discussed in chapter 6.

The results presented in this chapter, comprising the introduction and experimental demonstration of a tailored STII scheme with a broad tuning range, high quality beams and excellent reproducibility marks a transition point: from investigating the laser plasma wakefield acceleration process to operation of a laser plasma accelerator. This scheme opens a previously inaccessible mode of operation, which for the first time enables statistical research using results collected over many shots from a stable and tunable nanocoulomb-class laser plasma accelerator. This enables the beam loading study as will be presented in chapter 5, but also further research on subjects such as bunch length

and substructure studies using transition radiation or betatron source size measurement. Furthermore it paves the way for LPAs to be employed as drivers for secondary radiation sources such as Compton backscattering X-ray sources, compact FELs or laboratory size electron beam driven plasma accelerators.

5. INVESTIGATION OF BEAM LOADING

In LWFA, the wakefield formed by a driver laser delivers the accelerating forces responsible for acceleration of an injected electron bunch. Simultaneously, such an electron bunch also induces a self-field which superimposes onto the wakefield. If the total captured charge becomes large enough, the bunch self-fields will significantly influence the wakefield. As a consequence the plasma cavity structure will be reshaped and the effective accelerating field along the bunch length will be modified affecting the final beam parameters, i.e. maximum energy and energy spread. This phenomenon is known as beam loading and was discussed in more detail in section 2.7.

In the ongoing effort to employ laser plasma accelerators as drivers for the next generation radiation sources, they are being scaled to increasingly higher peak currents. This is done by increasing the charge of injected and accelerated bunches, leading to beam loading effects becoming increasingly pronounced. In order to successfully scale the peak output current of LPAs, it is vital to gain insight into beam loading effects, to control the beam loading process and finally to employ it in order to gain the best possible beam quality.

Although indications of beam loading have been reported earlier[112,182], no experimental studies exist for the case of a quasi-monoenergetic bunch in a heavily loaded wakefield. Now, operating a LPA in the tailored STII scheme as discussed in chapter 4 facilitates the possibility to conduct such a study for the first time. For this purpose, the amount of charge injected into the bubble cavity is varied in a controlled manner while retaining a narrow energy spread at various plasma densities. The work presented in this chapter is the first investigation that systematically explores the beam loading effect in the bubble regime and its consequence to the final beam quality over a large and well-controlled parameter range.

In order to study the beam-loading effect, the number of injected electrons is tuned by varying the nitrogen doping concentration at sets of equal plasma density as is discussed in section 5.1. By tuning the injected charge at equal plasma density, the injection volume can be kept equal for various loaded charges. This enables, in contrary to the work in ref.[182], to decouple the interplay between the beam loading effect and the initial injection volume to the evolution of energy spread.

From equation (2.49) an optimal load is expected where the energy spread of the

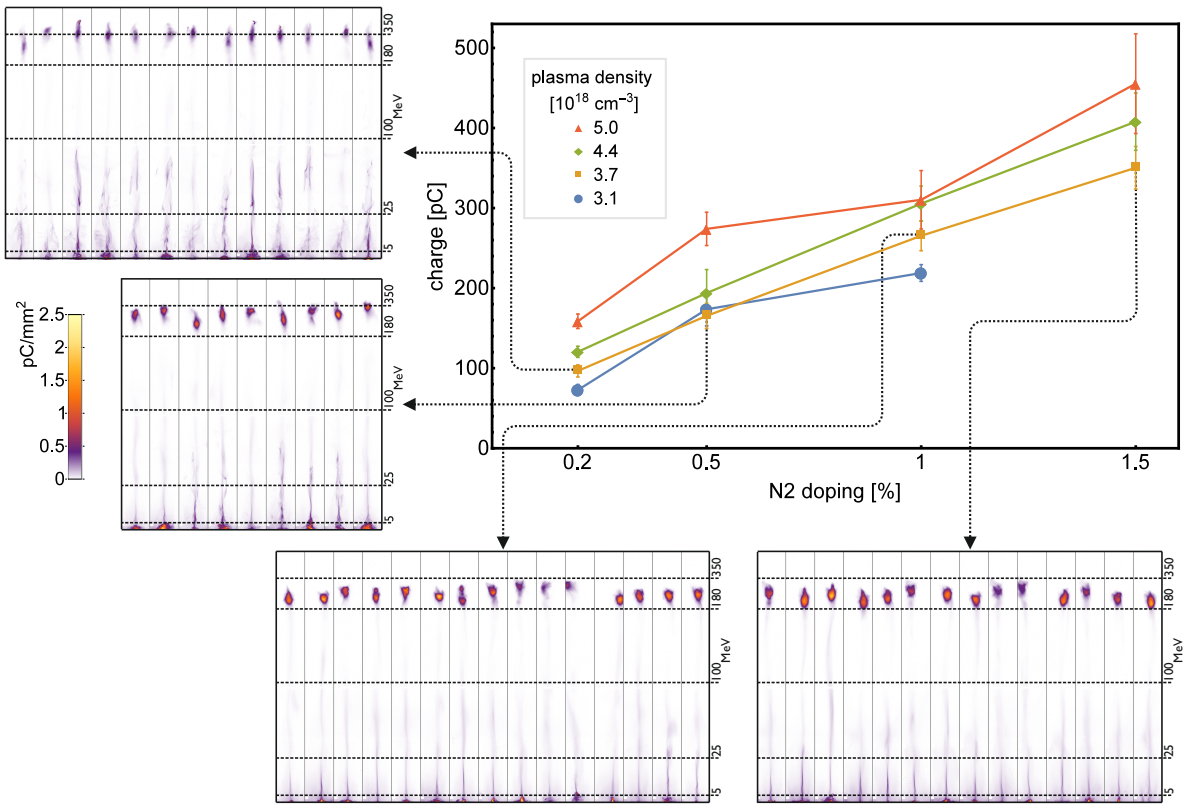

Figure 5.1.: **Charge within the FWHM of the energy peak for different nitrogen doping concentrations and plasma densities.** Data points represent the mean value from a set of shots (sample size between seven to twenty) at equal experimental parameters (2.5 J laser energy in 30 fs, vacuum focus position 1.5 mm behind the nozzle entrance). Connected data points show a set of equal plasma density. The error bars represent the standard error of the mean.

accelerator will be minimised. Taking sets at different plasma densities this value is expected to remain constant as the optimal load condition shows no dependency on plasma density, only an increase of attained energy is expected for higher plasma densities. Experimental results on the beam loading effects are presented in section 5.2.1. Considerations regarding the the acceleration length are discussed in section 5.2.2. In section 5.2.3 particle-in-cell results supporting observed experimental beam loading effects are presented. Section 5.3 discusses the charge density, which is relevant for future applications. Finally, section 5.4 discussed the accelerator's conversion efficiency.

5.1. TUNING THE INJECTED CHARGE

In order to study the beam loading effect, one should be able to tune the injected charge while keeping other parameters constant, thus avoiding changes in plasma dynamics before injection. The tailored STII scheme introduced in chapter 4 is used for this purpose. Here a mixture gas is used with the largest fraction consisting of helium, providing the background plasma due to its low ionisation threshold (see section 2.1). A small fraction of nitrogen, between 0.2% and 1.5%, provides electrons for STII injection

as explained in more detail in the previous chapter.

There are two key parameters that enable tuning of the injected charge which are experimentally explored here. Firstly, for a fixed doping, the injected charge increases with higher plasma densities. Secondly, for equal plasma densities the injected charge scales with the nitrogen doping. These dependencies are shown in figure 5.1.

The increase of injected charge with higher plasma densities follows from an interplay between both the increase of available electrons as well as the laser non-linear self-focussing dynamics. Changing the plasma density affects the laser beam dynamics even before injection occurs, thus potentially changing the injection volume.

This is not the case if the injected charge is tuned using the doping concentration. For a set of equal plasma density the initial phase-space volume for trapping can be kept equal for various loaded charges. Thus, injected charge is purely determined by the number of available nitrogen atoms.

Therefore, the beam loading effect is studied at datasets of equal plasma densities while controlling injected charge only with the nitrogen doping. Connected data points in figure 5.1 represent such sets. Changing the nitrogen doping influences the injected charge linearly. The beam loading effect is studied in this chapter at four different plasma densities.

To illustrate the tuning of injected charge, the raw data electron spectra at a plasma density of 3.7×10^{18} cm^{-3} (squares, yellow line) are shown in figure 5.1 next to the dependency graph. Injected charge influences beam parameters such as mean peak energy, charge, energy spread & cut-off energy. These parameters, relevant for the beam loading study in section 5.2, are extracted from every individual shot as illustrated in figure 4.7(b). For each data point up to twenty shots determine the mean parameter values and corresponding shot-to-shot fluctuations.

The results presented in figure 5.1 experimentally exclude beam loading as inducer of injection truncation. If beam loading were the main contributor to truncation this would lead to continuous injection till a critical load of the bubble inhibiting further injection would be reached. Instead truncation also occurs for lower injected charges (i.e. mono-energetic feature, low dark-current/background) which indicates that the injection volume does not depend on the injected charge.

5.2. EXPERIMENTAL OBSERVATION OF THE BEAM LOADING EFFECT

Using the tunability of the accelerator as discussed in section 5.1, the beam loading effect is studied over a large parameter range. From equation (2.49) an optimal load is expected where the energy spread of the accelerator will be minimised. Taking sets at different plasma densities this value is expected to remain constant. The optimal load shows no dependency on plasma density and only an increase of attained energy is expected for higher plasma densities.

Studied are four data-sets acquired at plasma densities between 3.1×10^{18} cm^{-3} and 5.0×10^{18} cm^{-3}. The injection volume can be considered to be constant within a data-set acquired at equal plasma density, which we will look into in more detail

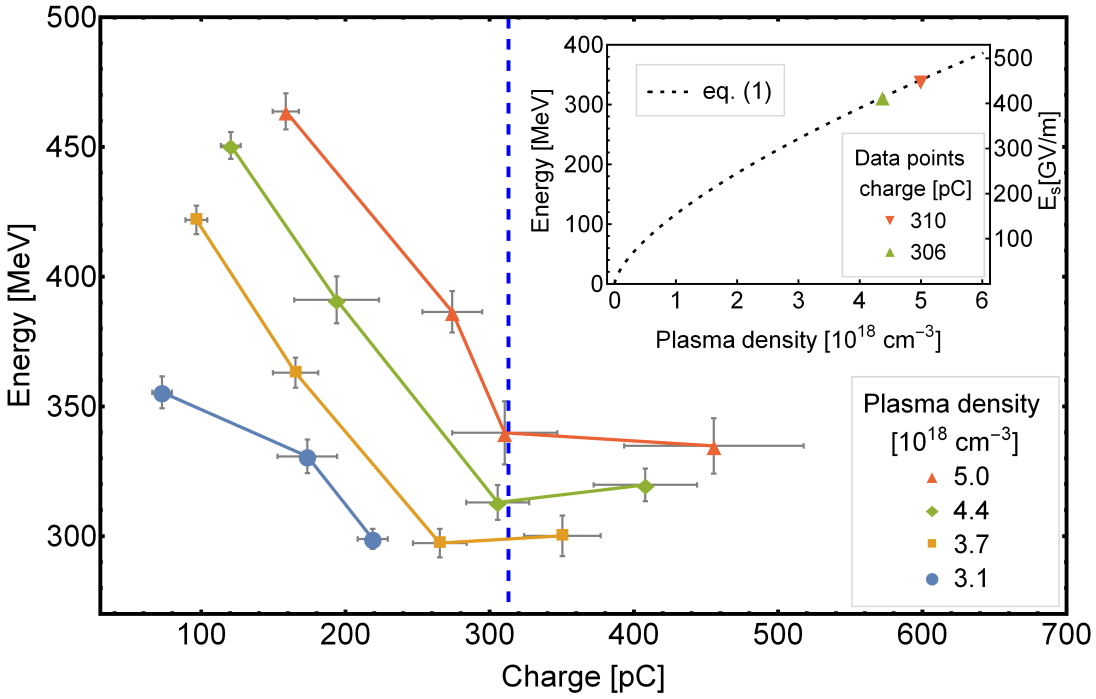

Figure 5.2.: **Electron energy dependency on both charge and plasma density.** Connected data points show a set of equal plasma density, increasing charge with increasing nitrogen doping (see figure 5.1). Electron energy is the E_{max} and charge within the FWHM of the energy peak is displayed. The error bars represent the standard error of the mean. The estimated optimal loaded charge according to equation (2.49) of 313 pC is indicated by the dashed vertical line. The peak mean electron energy dependency on charge and plasma density can be found in figure A.1. *The inset* shows the predicted acceleration gradient (right axis) according to equation (2.45) (dotted line) for a laser peak power P = 64 TW (equivalent to the experiment) under optimal loading conditions. The left axis shows the predicted electron energy, taking 0.76 mm effective acceleration distance. Data points represent measured data points at the predicted optimum.

in section 5.5. Varying the nitrogen doping from 0.2% to 1.5% allows tuning of the injected charge between roughly 100 pC to 500 pC. After accelerator performance is optimised as described in chapter 4, experimental parameters, i.e. laser energy, GVD, focus position and focus geometry, are kept constant apart from the plasma density and nitrogen doping. As in chapter 4, the target provider for this experiment is a Mach 10.4 supersonic de-Laval nozzle with a 0.35 mm throat and a 3 mm exit diameter which is described in section 3.4.4.

All results related to the beam loading study presented here are acquired within the same day in order to exclude potential experimental day-to-day fluctuations in laser operation. Online diagnostics situated at the experimental area are used to monitor the laser's near- and far-field and its temporal stability to verify stable operation during data acquisition.

5.2.1. BEAM LOADING EFFECTS

Figure 5.2 shows the maximum attained energy (E_{max}) for the parameter scan. Each data point represents the mean value from a set of up to twenty consecutive shots,

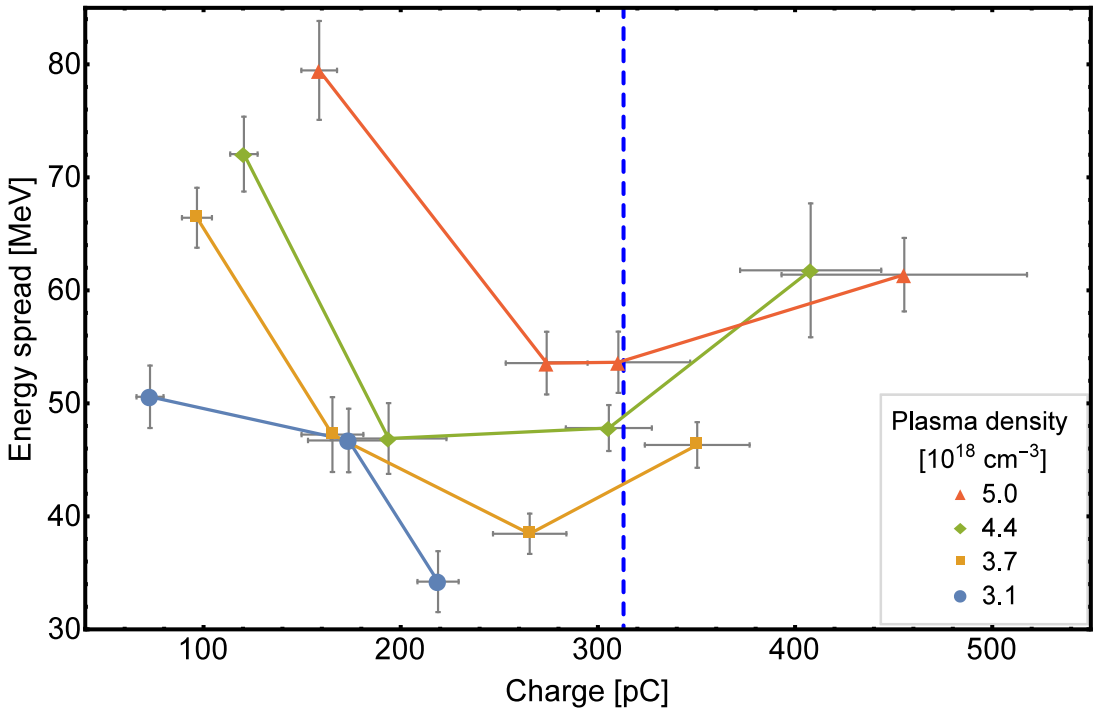

Figure 5.3.: **Beam absolute energy spread dependency on charge.** Shown is the FWHM energy spread. The dashed vertical line represents the optimal load expected from equation (2.49). The error bars represent the standard error of the mean. A graph showing the relative energy spread can be found in figure A.2.

with the error bars indicating the standard error of the mean. These results clearly indicate the influence of both injected charge and plasma density.

A consistently higher E_{max} is found for sets at a higher plasma density. This follows from the increased accelerating field E_z associated with higher plasma densities from equation (2.27). A beam loading effect can clearly be seen within the sets of equal plasma density. For increasing injected charge, a decrease in maximum electron energy (E_{max}) is observed. Since the injection dynamics, i.e., the position and volume of injection, does not change, this energy reduction can be attributed to the accelerating field suppression due to the load.

As discussed in section 2.7, beam loading perturbs the wakefield such that the accelerating field strength experienced by the trailing electrons is reduced. Resulting from this, the decrease in mean peak energy is smaller than the decrease observed in the E_{max} (See figure A.1). Consequently, the beam energy spread narrows for higher injected charges, as is shown in figure 5.3. A minimum of the energy spread, indicating the optimum load leading to a flattening of the accelerating field is seen at a charge of about 300 pC in FWHM for all sets of plasma densities. Beyond this optimum load, an increase of energy spread for loads is seen, originating from the beam loading effect overcompensating the field gradient for trailing electrons, leading to a non-constant gradient along the bunch.

The experimentally observed optimum is in agreement with the theoretically predicted optimum loading condition of 313 pC for the specific experimental parameters according to equation (2.49). This value is indicated in figures 5.2 & 5.3 by the dashed vertical line. As predicted, a deviation from the optimum, either by loading less or more charge into

the wakefield, leads to an increase in energy spread.

5.2.2. ACCELERATION LENGTH

As discussed in section 2.7.2, electron energy is expected to scale with $n_p^{2/3}$ for a given laser power under the optimal loading condition and a set acceleration length. The inset of figure 5.2 shows the accelerating gradient E_s from equation (2.48) plotted (right axis) as the dashed line. Related experimental data points, represented by triangles (left axis), confirm the expected dependency.

From this the effective acceleration length of the accelerator can be deduced to be around 0.8 mm (0.757 mm at 4.4×10^{18} cm^{-3} and 0.752 mm at 5.0×10^{18} cm^{-3}). This is shorter than the dephasing length, the propagation distance where the injected bunch enters the decelerating region of the bubble. From equation (2.32) this is $L_{deph} \approx 2.3$ mm (at 5.0×10^{18} cm^{-3}). Thus it can be excluded that the beam loading effects discussed above, i.e. the reduction in attained energy and energy spread, are related to dephasing.

As the scheme relies on non-linear self-focussing for the laser spot to evolve, it could be expected that the injection point and thus acceleration length has a dependency on the plasma density. However, no relevant difference in acceleration length was found.

Only the two experimental data points shown in the inset overlap by chance exactly with the optimal loading condition, as can be seen in figure 5.2. This is due to the incremental increase in nitrogen doping used in experiment (section 5.1), not allowing precision tuning of the injected charge. It would be desirable to upgrade the accelerator to allow for fine tuning of the nitrogen doping such that the validation of this dependency can be expanded with more data points at other densities.

For the study of the beam loading effect presented here, the acceleration length has been specifically chosen such that acceleration is stopped before dephasing occurs. If the acceleration length would reach the dephasing length where the injected bunch reaches the decelerating region of the bubble, consequent effects would mix with beam loading effects. Furthermore, if the laser driver becomes depleted, it becomes possible for a transition to PWFA (plasma wakefield acceleration, electron beam driven) to occur. Here, the laser driver starts to diverge once the non-linear self-guiding condition no longer being fulfilled. Subsequently, the electron beam will act as a driver, forming its own wakefield. To avoid this, the laser-plasma interaction length is around 3 mm, which is chosen below the laser depletion length of 3.2 mm at given laser parameters and a plasma density of 5.0×10^{18} cm^{-3} according to equation (2.31). If a transition to PWFA were to occur, the electron beam would give back its energy to the plasma as it drives the wake, increasing the energy spread[183]. Such behaviour is not observed in presented experiments and instead the energy spread keeps decreasing toward the optimum loading condition. This experimental observation further confirms the expectation that the acceleration length is below the dephasing length. Thus a transition to PWFA in the results presented here can be excluded.

It should be noted that consequently the full potential of the accelerator has not been reached in the results presented in this chapter. Higher electron energies while still

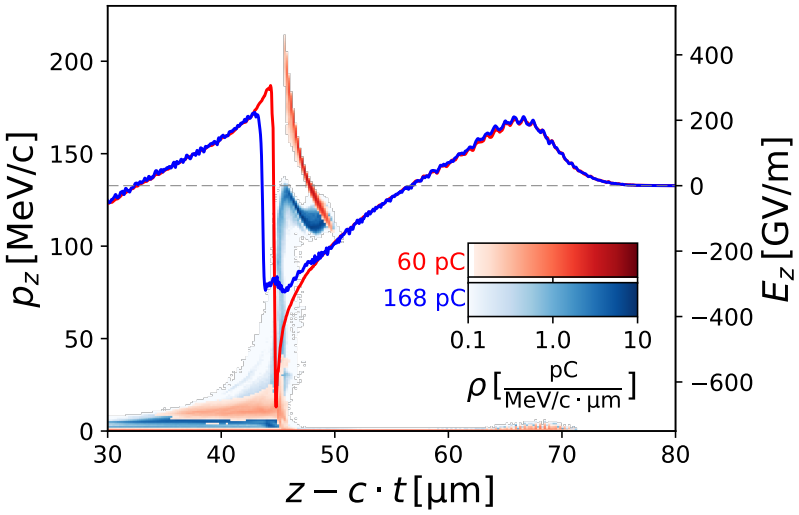

Figure 5.4.: **PIC simulation results showing the beam loading effect.** The injected bunch charge influences the accelerating field E_z (line graphs, right axis) and electron phase space (colour scale, left axis) for 60 pC load in the peak (red) and 168 pC load (blue). Corresponding to z = 2.3 mm in figure 4.9.

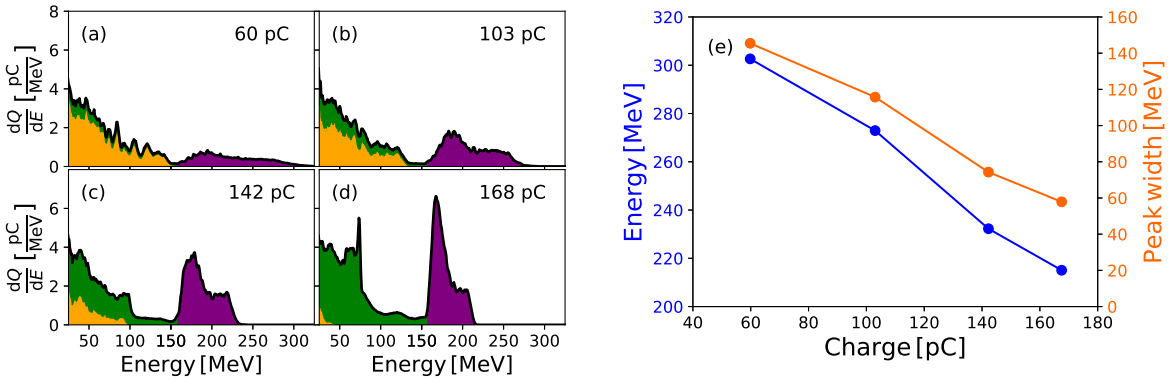

Figure 5.5.: **PIC simulation results illustrating beam loading effects.** *(a)-(d)* show electron energy histograms for increasing injected charges within the energy peak (purple area). The green and purple shaded area is the contribution from electrons originating from nitrogen, the orange shaded area from helium electrons. The black line indicates the cumulative spectrum. Figure *(a)* corresponds to the histogram seen in figure 4.9. *(e)* shows how maximum attained energy (left axis) and beam energy spread (right axis) depend on injected charge.

operating in the optimal loading condition can be reached by extending the accelerator to approach the dephasing length.

5.2.3. PARTICLE-IN-CELL SIMULATIONS

In order to support the observations discussed above, 3D Particle-In-Cell (PIC) simulations using the PIConGPU code[184,185] were performed.[1] The simulations were set up such to take realistic experimental parameters in order to study the beam loading effect

[1] More information on the PIC simulations can be found in appendix B

under realistic laser-plasma dynamics. However, with the current implementation of the both the BSI and ADK ionisation scheme in PIConGPU it is not possible to match the charge observed in experiment. Therefore, the nitrogen doping concentration was artificially increased in the simulation in order to trap a higher charge. This way the plasma and injection dynamics are kept constant at experimental conditions. This would not be the case if the laser strength parameter a_0 would be increased and/or the laser spot size would be artificially decreased, as is often done in simulations to artificially trap a higher charge.

Although the simulated injected charge does not reach the optimal loading condition, qualitatively the beam loading effects can be observed until this point. Figure 4.9, already discussed before in section 4.5, shows the temporal evolution of the injected electron energy. The driver laser beam requires the first half of the jet for focusing before ionisation injection occurs. Injection is terminated due to the self-truncation effect and is followed by acceleration along approximately 0.8 mm distance. This value matches the estimate from experimental data made in section 5.2.2.

The beam loading effect becomes clearly visible in figure 5.4. Increasing injected charge, a clear effect on the accelerating field E_z is observed. For the case where a 168 pC bunch is injected a suppression of the accelerating field E_z by approximately 50 GV/m occurs together with an easing of the accelerating field slope along the bunch compared to the weakly loaded case where a 60 pC bunch is injected. Trailing electrons being affected strongest, this field change subsequently results to a compression of the electron momentum phase-space distribution resulting in both a reduction in E_{max} as well as a reduction of energy spread. These effects are further illustrated in figure 5.5 where the final electron energy distribution is investigated for loads between 60 and 168 pC. In agreement with experimental results a decrease of both maximum electron energy and energy spread with increasing charge is observed.

5.3. CHARGE DENSITY

For certain applications, e.g. FELS, an even smaller energy spread than observed here can be required. For such cases, one could select only a limited energy range, making only a part of the electron bunch charge usable. Thus the charge density, i.e. charge per energy bin, becomes relevant. Figure 5.6 shows how the charge density within the peak FWHM depends on injected charge. Here the beam divergence measured in the spectrometer non-bending plane is also taken into account, giving the charge density in pC MeV^{-1} $mrad^{-1}$. A steady increase with injected charge till the optimum loading condition is observed, there reaching an optimum charge density of 1 pC MeV^{-1} $mrad^{-1}$. Sets of lower plasma densities show a higher charge density compared than sets at higher plasma densities due to the higher energy spread present at higher plasma densities (see figure 5.3).

5.4. ACCELERATOR EFFICIENCY

For an accelerator to work efficiently, an as large as possible fraction of the driver energy has to be transferred to the accelerated beam. Theoretically a correctly tailored electron

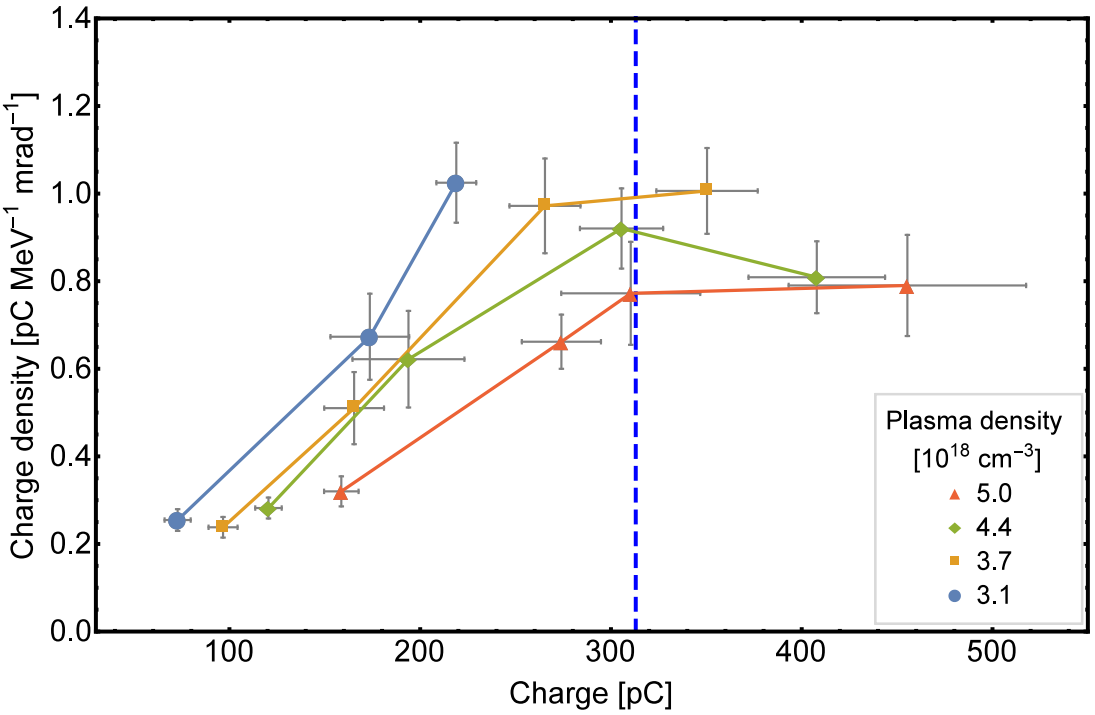

Figure 5.6.: **Charge density within the peak FWHM dependency on injected charge.** The beam divergence (measured in the spectrometer non-bending plane) is also taken into account, giving the charge density in pC MeV^{-1} mrad^{-1}. The error bars represent the standard error of the mean. The estimated optimal load according to equation (2.49) of 313 pC is indicated by the dashed vertical line. The charge density in pC MeV^{-1}, not taking beam divergence into account can be found in figure A.3.

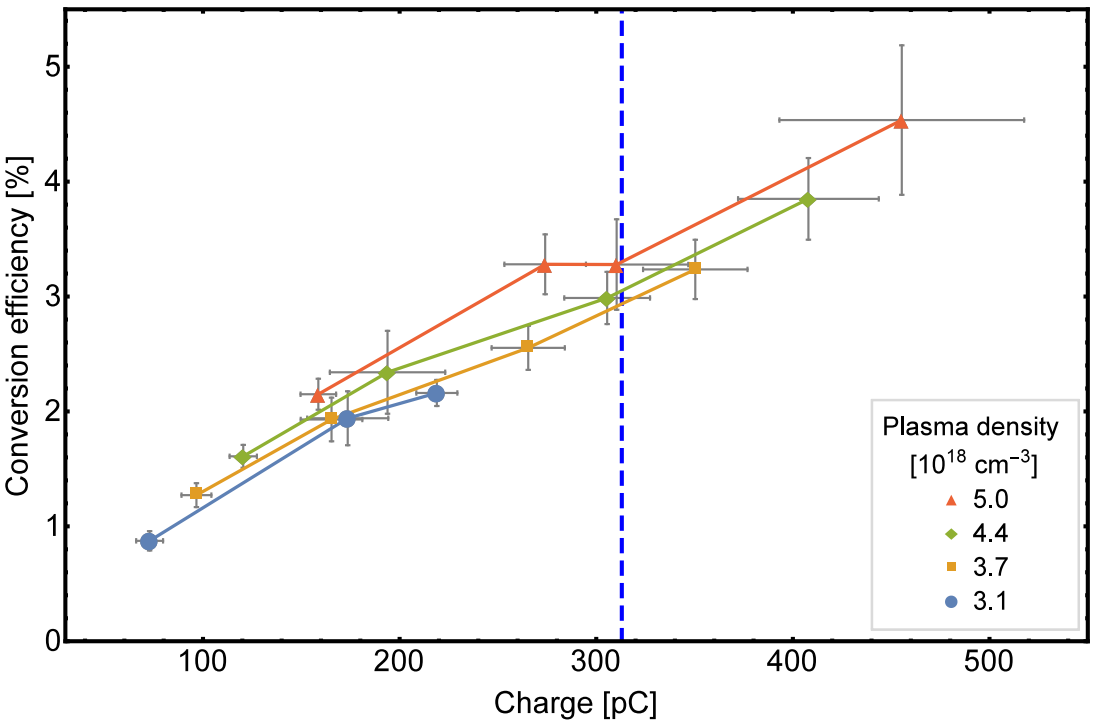

Figure 5.7.: **Accelerator conversion efficiency.** Efficiency from laser energy within the beam waist to kinetic energy of electrons within the energy peak FWHM.

bunch can very efficiently extract energy from the wakefield, with theoretical efficiencies close to 90%[54,55,114]. Nonetheless, LPAs traditionally have low conversion efficiencies, especially in comparison with conventional accelerators. The foremost limitation is that, if driven in the non-linear bubble regime, the driver laser needs to remain above a certain threshold power in order to be confined over the entire interaction length (see section 2.3). As the laser beam is generally dumped after the accelerator, remaining energy cannot be recycled. Further energy is lost in the requirement for ionisation of the medium and to energy located outside of the laser focus (section 4.1.3). For the LPA presented here, the conversion efficiency is plotted in figure 5.7. This plot shows the energy conversion efficiency from the laser energy within the beam waist to kinetic energy of electrons within the peak FWHM, i.e. $\eta = E_{\text{bunch}}/E_{\text{laser}}$. The conversion efficiency is mostly dependent on the injected charge and only weakly dependent on the plasma density. At the optimal loading condition a laser to electron beam conversion efficiency of around 3% is reached.

5.5. DISCUSSION

The results in this chapter represent the first investigation that systematically explores beam loading effects in the bubble regime over a large and well-controlled parameter range. This is enabled by a new robust STII scheme with the ability to keep the injection volume close to constant for various charges, eliminating significant injection influences on the final beam parameters.

The condition that the injection volume is constant for different quantities of injected charge is crucial for this study. In this way, the change on beam parameters can be directly attributed to the modification of the wakefield by beam loading. In section 5.1 it has already been established that beam loading is not responsible for the truncation mechanism, indicating that the injection volume does not depend on the injected charge. However, from experimental observations alone it cannot be completely excluded that there is a small load dependent influence on the injection volume and associated energy spread present directly after injection.

The injection volume, determined by the longitudinal and transversal trapping condition as discussed in section 4.5.1, is located at the front-side of the bubble. Electrons being trapped, slip to the backside of the bubble after being ionised around the laser peak intensity. There they subsequently load the plasma bubble. An injected load can cause a small cavity deformation, changing the trapping conditions, which in effect can influence the injection volume. As this effect cannot be decoupled from the beam loading effect in experiments, this effect is investigated with the help of PIC simulations.

Figure 5.8 shows that at equal plasma density and laser parameters the ionisation region radius and length are independent of nitrogen doping . However, ionisation volume and injection volume are not the same thing. Although ionisation happens within a large region, injection occurs only over a limited length as is discussed in section 4.5 (see figure 4.9). Due to the resolution limit the exact injection volume cannot be extracted from the simulation, but the beam dynamics can be assessed directly after injection. Figure 5.9 shows the electron energy distribution in the bubble evaluated right after

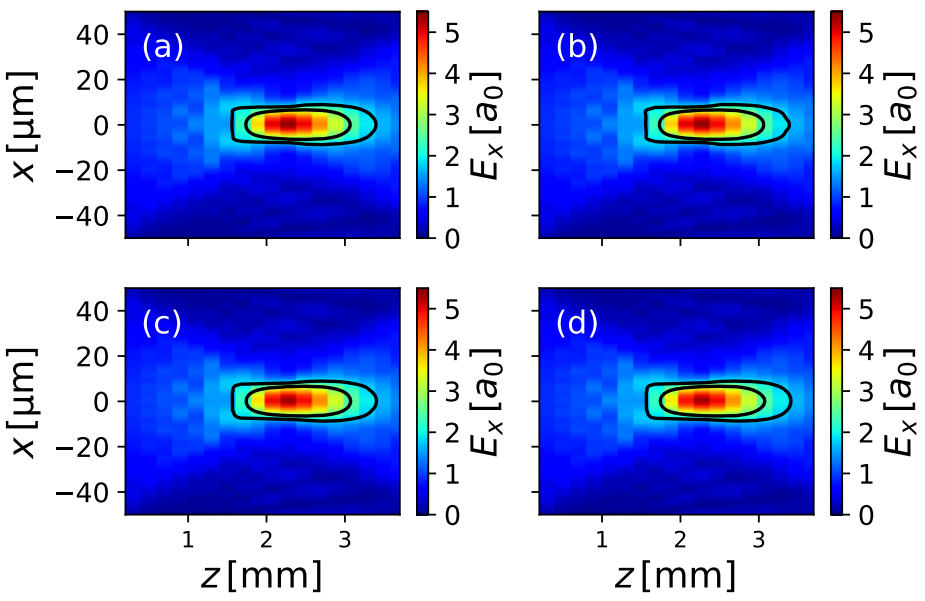

Figure 5.8.: **Laser field strength evolution from PIConGPU simulations.** Evolutions for different nitrogen doping concentrations are shown. The inner and outer region, indicated by black lines, represent the regions where the field is sufficiently high to ionise the two nitrogen K-shell electrons. Subfigure *(a)* corresponds to figure 4.9. All subfigures correspond to the subfigures of figure 5.5, with the following charges injected in the peak due to different nitrogen dopings: *(a)* 60 pC *(b)* 103 pC, *(c)* 142 pC *(d)* 168 pC.

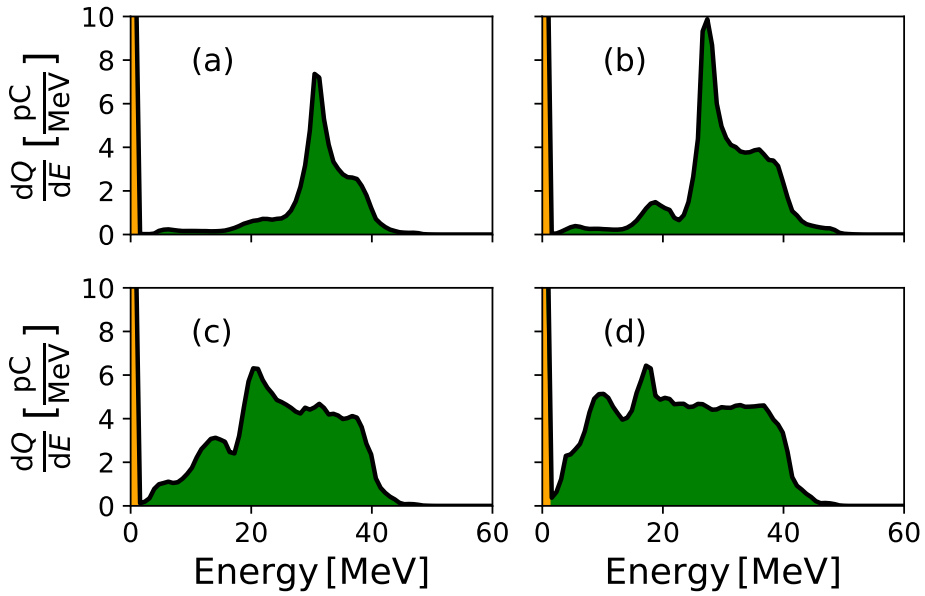

Figure 5.9.: **Electron energy histograms from PIConGPU simulations.** Histograms are assessed right after injection at z = 1.8 mm. Subfigure *(a)* corresponds to figure 4.9 and contains a charge of 60 pC in the main peak after acceleration. All subfigures correspond to the subfigures of figure 5.5, with the following charges in the peak: *(a)* 60 pC *(b)* 103 pC, *(c)* 142 pC *(d)* 168 pC.

injection (z = 1.9 mm in figure 4.9) for different amounts of injected charge. It can be seen that injection of more charge contributes to an additional energy spread right after injection, pointing to a suspected increase of injection volume.
Comparing the energy spread right after injection and at the end of the acceleration process (figure 5.5, section 5.2.3), it is found that the contribution of energy spread from injection is small compared to the contribution of the acceleration process.

At 60 pC injected charge one finds an absolute energy spread of ∼10 MeV right after injection, which in this weakly loaded case grows strongly to 150 MeV during the acceleration process. In contrast, at 168 pC of injected charge the accelerating field is altered further due to beam loading, leading to only a slight increase of the absolute energy spread during the acceleration process, from ∼35 MeV right after injection to 60 MeV after acceleration.

Thus, although the injection volume might vary depending on the injected charge, this effect is negligible compared to the effect from the acceleration process itself. Therefore decoupling the interplay between the beam loading effect and the initial injection volume to the evolution of energy spread.

To conclude, presented in this chapter is the first beam loading study performed on a nanocoulomb-class laser plasma accelerator with quasi-monoenergetic bunches in a heavily loaded wakefield. The results presented here are a significant improvement over previously reported beam loading studies.

Shown is that the beam loading effect causes a suppression of the accelerating field, causing a reduction of achieved electron energy at larger loads. The optimal loading condition is expressed in a minimisation of energy spread, which was found to occur at the theoretically predicted load[54,55]. These finding will have a profound influence on future development of LPAs. The results presented in this chapter show that in order to generate higher charge beams with a small energy spread, plasma accelerators have to be operated at the optimum loading condition.

6. SUMMARY & OUTLOOK

The work presented in this thesis represents the first systematic experimental study of beam loading by a quasi-monoenergetic bunch in the bubble regime. This study is enabled by the implementation of a tailored scheme of the self-truncation ionisation injection process resulting in a laser wakefield accelerator in the nanocoulomb-class.

This tailored scheme gives stable operation of the accelerator over a large tunable range of injected charge. Contrary to other injection schemes, large amounts of charge can be injected into the wakefield in a controlled manner while still retaining a small energy spread due to a limited injection time. This is a significant improvement over previous existing results at LPAs, where a high charge could only be injected at the cost of high energy spread.

This new mode of operation enabled the verification of the beam loading theory developed by Tzoufras et al.[54]. Loading charges up to 0.5 nC (within FWHM) into the wakefield, it is shown that high charge beams with a low energy spread can only be generated if a accelerator is operated in the optimal loading condition. This finding will influence how future plasma accelerators in the bubble regime will be operated. Specifically for implementing near-future LPAs aimed at applications, where the primary goal will be to generate high quality electron beams at a high peak current.

An important next step will be to precisely determine the bunch length. As this, together with the bunch charge, directly relates to the peak current. The use of a broadband (UV-FIR) spectrometer to measure bunch length dependent transition radiation (TR) has already been discussed to some extend in section 4.6. In parallel to the PhD project presented in this thesis, such a diagnostic with a temporal resolution down to 400 attoseconds is being implemented by Omid Zarini in the framework of his PhD project. This diagnostic was not available at the time of the main work presented here, but recently some preliminary results have been acquired. Figure 6.1 shows a preliminary bunch length reconstruction. A bunch envelope of ~25 fs is found, while strong femtosecond sub-structures exist. The origin of these substructures is currently being investigated and could be related to the injection mechanism or to direct laser interaction of the injected bunch with the driver laser.

Further research into the LPA, aiming both at understanding the origin of the longitudinal bunch structures as well as the influence of accelerator parameters on the

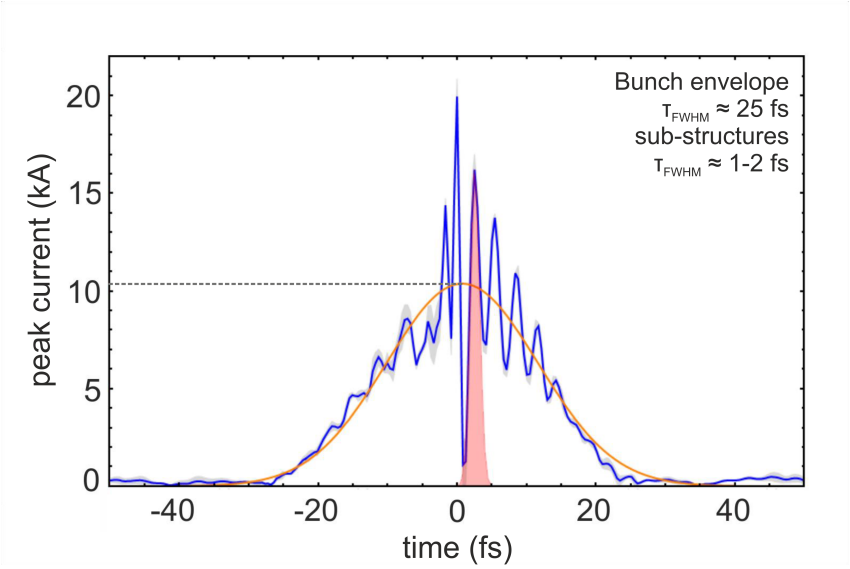

Figure 6.1.: **Longitudinal bunch profile.** Reconstructed from as single-shot measurement by a transition radiation spectrometer. Beam parameters: E_{mean} = 300 MeV, $\Delta E/E_{mean}$ = 15%, Q_{FWHM} = 170 pC. Courtesy of Omid Zarini.

bunch substructures and overall length, is now possible with the use of the single shot TR pulse length diagnostic. Its final implementation will allow to further optimise the accelerator performance, specifically its bunch length and peak current.

To further gain insight into the dynamics of the acceleration process further diagnostics are required which are able to probe inside the accelerator. However, to determine beam properties within the accelerator or directly at its exit is an especially difficult task in LPAs.

One method capable of this is by measuring the spectral shape of betatron radiation. This radiation arises from injected electrons performing transverse (betatron) oscillations around the central propagation axis due to the strong transversal focussing fields present in a wakefield. The resulting emission is related to these oscillation and can be used to extract parameters such as electron trajectories, beam emittance and bunch size at the exit of the wakefield[186–189]. In a PhD project by Alexander Köhler, betatron radiation measurements are being used for source size measurements at the accelerator presented here[7] and an ongoing effort is being made to further diagnose the beam divergence and emittance.

Another diagnostic tool is inverse Compton scattering (ICS), which can be used as a non-destructive diagnostic tool to diagnose beam energy, energy spread, divergence and beam direction directly at the accelerator exit without the need for free-space propagation[2,9,183,190].

Implementing these tools will lead to a deeper understanding of the accelerator dynamics as well as to measure and improve further beam parameters. Specifically beam emittance can be vital for certain applications. Laser-plasma accelerator-driven FELs are one example of next-generation radiation sources which require low-emittance electron beams. Due to strong space charge effects and their still relatively large energy spread, bright LPA electron beams generally undergo a quick emittance growth once allowed to

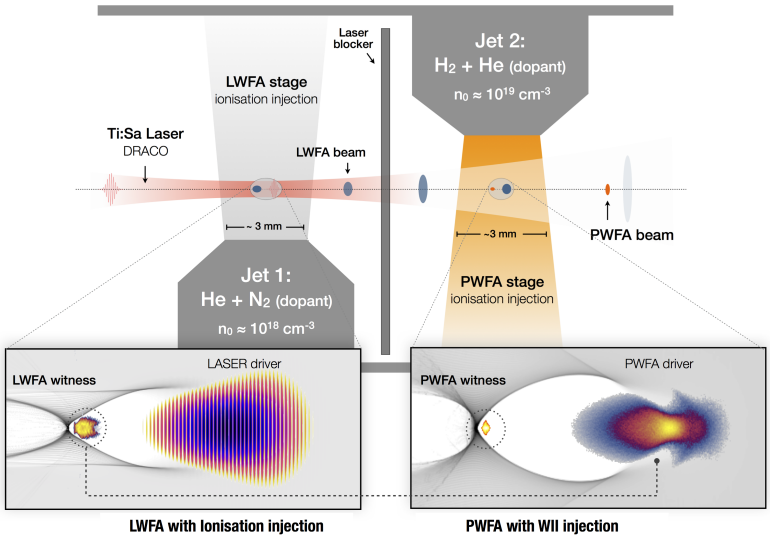

Figure 6.2.: **LWFA driven PWFA.** Schematic of a proof-of-principle experiment. Here the accelerator presented in chapter 4 is used to produce a electron bunch driver for a second beam driven accelerator. Figure from ref.[5]

freely propagate in vacuum[191–195]. Therefore, beam diagnostic at the accelerator exit and special beam transport is required to capture the beam directly after the accelerator in order to preserve the phase-space quality.

Notwithstanding future accelerator improvements, the high charge given by the LPA presented in this thesis already opens the possibility for multiple applications.

Direct access to an x-ray source, besides diagnostic purposes, is given by betratron radiation. This provides a femtoseconds, high-brightness, broadband source up to a few keV[7] which can be used for x-ray phase contrast imaging[196] or as a synchronised probe in high-energy-density pump-probe experiments.

For harder x-rays and γ-rays the LPA can be used as a driver for an all-optical ICS source. In this case, the LPA electron beam interacts with a second counter-propagating laser beam to create ultra-high peak brilliance beams in the MeV range[42–44]. Even higher brilliance can be reached by expanding this scheme to an optical FEL scheme, such as travelling-wave Thomson-scattering[49,197,198].

To further develop plasma acceleration technology for the highest demand of electron beam brightness, it is sensible to investigate charged particle beams as an alternative wakefield driver. Beam-driven plasma wakefield acceleration (PWFA)[78,199] has several advantages over laser driven wakefield acceleration, most notably the mitigation of dephasing between the driver and the injected bunch, leading to much higher energy gain potential from a single stage. In the bubble regime, PWFA has the promise to create high quality electron beams with very low emittance and low energy spread[50]. The high current required to drive a PWFA accelerator in the bubble regime has now become available with the demonstrated bunch charge of the LPA in this thesis. This opens the possibility to combine both techniques, utilising each scheme's unique advantages. The PWFA stage can act as an energy and beam brightness booster of the LWFA stage

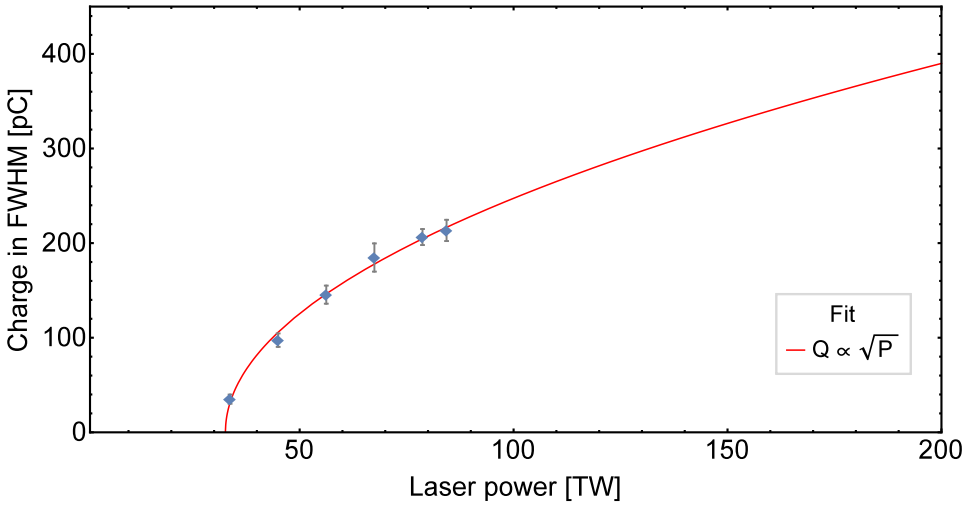

Figure 6.3.: **Scaling of charge within FWHM with laser power.** Circles represent measured data points taken with a nitrogen doping of 1% at a plasma density of $3.1 \times 10^{18}\text{cm}^{-3}$. The error bars represent the standard error of the mean. The red curve represents a fit following the expected $Q \propto \sqrt{P}$ dependency. The relative energy spread measured to be between 15% for all measurement points.

output, increasing beam quality for applications and secondary light sources.

A proof-of-principle experiment proposal is being made to demonstrate the feasibility of laser to beam driven plasma wakefield acceleration (LPWFA)[5]. The concept of this experiment is shown in figure 6.2, where the LWFA beam presented in this thesis is utilised to create a higher brightness in a second PWFA stage. Currently this scheme is being explored. Initial results clearly show that the LWFA bunch can drive a wakefield in the second stage and strong indications exist of injection and acceleration of a witness bunch in the PWFA stage.

An even higher bunch charge will be beneficial for LPWFA , as will be the case for many other application. The optimal loading condition required for a low energy spread is linked to the laser power with $Q \propto \sqrt{P}$ from equation (2.49). To increase the bunch charge, the accelerator has to be driven by a stronger laser.

Figure 6.3 shows the experimental correlation of the total charge to the laser peak power measured at a fixed plasma density and nitrogen doping. For this the laser peak power was adjusted from 40 TW to 90 TW. The data exhibits the $Q \propto \sqrt{P}$ dependency as originally predicted by Lu *et al.*[38], Gordienko and Pukhov[37] and by equation (2.49). The intersection at zero charge for a laser power of 33 TW corresponds to the injection threshold for the given experimental parameters. Expanding this scaling and operating in the optimum loading condition, it is expected that a LPA driven by a petawatt laser will result in high-quality electron beams with peak currents close to 100 kA. This is two to three orders of magnitude larger than can be achieved in state-of-the art large-scale accelerator facilities.

To reach the full potential at a given laser power, the acceleration length should be extended to the dephasing limit as a further improvement step. In this thesis, the acceleration length was purposefully kept below this limit in order to demonstrate the beam loading effect. Expanding the acceleration length will increase the beam energy. The

absolute energy spread should be retained in the optimal loading condition, effectively decreasing the relative energy spread at higher beam energies.

To conclude, boosting a LPA to the nanocoulomb-class while attaining a low energy spread has lead to a previously inaccessible operation range. Previously not performable secondary experiments now become accessible, with a laser- to beam-driven scheme now under investigation. Even further improvements of accelerator performance are expected by future research steps.

The fundamental results presented in this thesis are anticipated to have a strong impact on the parameter design of future plasma accelerators. The tailored STII injection mechanism gives a good control over injected charge, with a limited injection time and correlated energy spread. The findings on beam loading, where the optimal loading condition keeps the energy spread at a minimum, will have to be kept in consideration for any accelerator, laser- or beam-driven, operated in the bubble regime.

BIBLIOGRAPHY

[1] A. Irman et al., "Improved performance of laser wakefield acceleration by tailored self-truncated ionization injection", Plasma Physics and Controlled Fusion **60**, 044015 (2018) 10.1088/1361-6587/aaaef1.

[2] J. M. Krämer et al., "Making spectral shape measurements in inverse Compton scattering a tool for advanced diagnostic applications", Scientific Reports **8**, 1398 (2018) 10.1038/s41598-018-19546-0.

[3] J. P. Couperus et al., "Demonstration of a beam loaded nanocoulomb-class laser wakefield accelerator", Nature Communications **8**, 487 (2017) 10.1038/s41467-017-00592-7.

[4] U. Schramm et al., "First results with the novel petawatt laser acceleration facility in Dresden", Journal of Physics: Conference Series **874**, 012028 (2017) 10.1088/1742-6596/874/1/012028.

[5] T. Heinemann et al., "Investigating the key parameters of a staged laser- and particle driven plasma wakefield accelerator experiment", Proceeding of IPAC2017 (2017) 10.18429/JACoW-IPAC2017-TUPIK010.

[6] J. P. Couperus et al., "Tomographic characterisation of gas-jet targets for laser wakefield acceleration", Nuclear Instruments and Methods in Physics Research, Section A: Accelerators, Spectrometers, Detectors and Associated Equipment **830**, 504–509 (2016) 10.1016/j.nima.2016.02.099.

[7] A. Köhler et al., "Single-shot betatron source size measurement from a laser-wakefield accelerator", Nuclear Instruments and Methods in Physics Research Section A: Accelerators, Spectrometers, Detectors and Associated Equipment **829**, 265–269 (2016) 10.1016/j.nima.2016.02.031.

[8] U. Schramm et al., "Bright X-ray pulse generation by laser Thomson-backscattering and traveling wave optical undulators", in Frontiers in optics 2014 (2014), FTu4G.2, 10.1364/FIO.2014.FTu4G.2.

[9] A. Jochmann et al., "High resolution energy-angle correlation measurement of hard x rays from laser-Thomson backscattering", Physical Review Letters **111**, 114803 (2013) 10.1103/PhysRevLett.111.114803.

[10] A. Jochmann et al., "Operation of a picosecond narrow-bandwidth laser-Thomson-backscattering X-ray source", Nuclear Instruments and Methods in Physics Research Section B: Beam Interactions with Materials and Atoms **309**, 214–217 (2013) 10.1016/j.nimb.2013.01.065.

[11] T. Kurz et al., "Calibration and cross-laboratory implementation of scintillating screens for electron bunch charge determination", Review of scientific instruments, in press (2018) 10.1063/1.5041755.

[12] J. D. Cockcroft and E. T. S. Walton, "Experiments with high velocity positive ions", Proceedings of the Royal Society A: Mathematical, Physical and Engineering Sciences **129**, 477–489 (1930) 10.1098/rspa.1930.0169.

[13] G. R. Werner, "Probing and modeling voltage breakdown in vacuum", PhD thesis (Cornell University, 2004).

[14] S. Doebert, *Gradient limitations for high-frequency accelerators*, tech. rep. September (SLAC National Accelerator Laboratory (SLAC), Menlo Park, CA (United States), Sept. 2004), 10.2172/833031.

[15] T. Tajima and J. M. Dawson, "Laser electron accelerator", Physical Review Letters **43**, 267–270 (1979) 10.1103/PhysRevLett.43.267.

[16] D. Strickland and G. Mourou, "Compression of amplified chirped optical pulses", Optics Communications **55**, 447–449 (1985) 10.1016/0030-4018(85)90151-8.

[17] P. Maine et al., "Generation of ultrahigh peak power pulses by chirped pulse amplification", IEEE Journal of Quantum Electronics **24**, 398–403 (1988) 10.1109/3.137.

[18] C. E. Clayton et al., "Ultrahigh-gradient acceleration of injected electrons by laser-excited relativistic electron plasma waves", Physical Review Letters **70**, 37–40 (1993) 10.1103/PhysRevLett.70.37.

[19] Y. Kitagawa et al., "Beat-wave excitation of plasma wave and observation of accelerated electrons", Physical Review Letters **68**, 48–51 (1992) 10.1103/PhysRevLett.68.48.

[20] K. Nakajima et al., "A proof-of-principle experiment of laser wakefield acceleration", Physica Scripta **T52**, 61–64 (1994) 10.1088/0031-8949/1994/T52/009.

[21] M. C. Downer et al., "Diagnostics for plasma-based electron accelerators", Reviews of modern physics, in review (2018).

[22] A. Pukhov and J. Meyer-ter-Vehn, "Laser wake field acceleration: the highly non-linear broken-wave regime", Applied Physics B: Lasers and Optics **74**, 355–361 (2002) 10.1007/s003400200795.

[23] C. G. R. Geddes et al., "High-quality electron beams from a laser wakefield accelerator using plasma-channel guiding", Nature **431**, 538–541 (2004) 10.1038/nature02900.

[24] S. P. D. Mangles et al., "Monoenergetic beams of relativistic electrons from intense laser–plasma interactions", Nature **431**, 535–538 (2004) 10.1038/nature02939.

[25] J. Faure et al., "A laser–plasma accelerator producing monoenergetic electron beams", Nature **431**, 541–544 (2004) 10.1038/nature02963.

[26] W. P. Leemans et al., "Multi-GeV electron beams from capillary-discharge-guided subpetawatt laser pulses in the self-trapping regime", Phys. Rev. Lett. **245002**, 1–5 (2014) 10.1103/physrevlett.113.245002.

[27] A. J. Gonsalves et al., "Generation and pointing stabilization of multi-GeV electron beams from a laser plasma accelerator driven in a pre-formed plasma waveguidea)", Physics of Plasmas **22**, 056703 (2015) 10.1063/1.4919278.

[28] X. Wang et al., "Quasi-monoenergetic laser-plasma acceleration of electrons to 2 GeV", Nature Communications **4** (2013) 10.1038/ncomms2988.

[29] S. Steinke et al., "Staging of independent laser plasma accelerators", in Aip conference proceedings, Vol. 1812 (2017), p. 020003, 10.1063/1.4975839.

[30] C. B. Schroeder et al., "Physics considerations for laser-plasma linear colliders", Physical Review Special Topics - Accelerators and Beams **13**, 101301 (2010) 10.1103/PhysRevSTAB.13.101301.

[31] A. Debus et al., "Breaking the dephasing and depletion limits of laser-wakefield acceleration", in review (2018).

[32] M. Litos et al., "High-efficiency acceleration of an electron beam in a plasma wakefield accelerator", Nature **515**, 92–95 (2014) 10.1038/nature13882.

[33] S. Corde et al., "Multi-gigaelectronvolt acceleration of positrons in a self-loaded plasma wakefield", Nature **524**, 442–445 (2015) 10.1038/nature14890.

[34] E. Gschwendtner et al., "AWAKE, the advanced proton driven plasma wakefield acceleration experiment at CERN", Nuclear Instruments and Methods in Physics Research Section A: Accelerators, Spectrometers, Detectors and Associated Equipment **829**, 76–82 (2016) 10.1016/j.nima.2016.02.026.

[35] A. Buck et al., "Real-time observation of laser-driven electron acceleration", Nature Physics **7**, 543–548 (2011) 10.1038/nphys1942.

[36] O. Lundh et al., "Few femtosecond, few kiloampere electron bunch produced by a laser–plasma accelerator", Nature Physics **7**, 219–222 (2011) 10.1038/nphys1872.

[37] S. Gordienko and a. Pukhov, "Scalings for ultrarelativistic laser plasmas and quasimonoenergetic electrons", Physics of Plasmas **12**, 043109 (2005) 10.1063/1.1884126.

[38] W. Lu et al., "Generating multi-GeV electron bunches using single stage laser wakefield acceleration in a 3D nonlinear regime", Physical Review Special Topics - Accelerators and Beams **10**, 1–12 (2007) 10.1103/PhysRevSTAB.10.061301.

[39] Y. F. Li et al., "Generation of 20 kA electron beam from a laser wakefield accelerator", Physics of Plasmas **24**, 023108 (2017) 10.1063/1.4975613.

[40] W. P. Leemans et al., "Observation of terahertz emission from a laser-plasma accelerated electron bunch crossing a plasma-vacuum boundary", Physical Review Letters **91**, 074802 (2003) 10.1103/PhysRevLett.91.074802.

[41] B. Green et al., "High-field high-repetition-rate sources for the coherent THz control of matter", Scientific Reports **6**, 22256 (2016) 10.1038/srep22256.

[42] N. D. Powers et al., "Quasi-monoenergetic and tunable X-rays from a laser-driven compton light source", Nature Photonics **8**, 28–31 (2014) 10.1038/nphoton.2013.314.

[43] K. Ta Phuoc et al., "All-optical compton gamma-ray source", Nature Photonics **6**, 308–311 (2012) 10.1038/nphoton.2012.82.

[44] G. Sarri et al., "Ultrahigh brilliance multi-MeV gamma-ray beams from nonlinear relativistic Thomson scattering", Physical Review Letters **113**, 224801 (2014) 10.1103/PhysRevLett.113.224801.

[45] H.-P. Schlenvoigt et al., "A compact synchrotron radiation source driven by a laser-plasma wakefield accelerator", Nature Physics **4**, 130–133 (2007) 10.1038/nphys811.

[46] M. Fuchs et al., "Laser-driven soft-X-ray undulator source", Nature Physics **5**, 826–829 (2009) 10.1038/nphys1404.

[47] A. R. Maier et al., "Demonstration scheme for a laser-plasma-driven free-electron laser", Physical Review X **2**, 031019 (2012) 10.1103/PhysRevX.2.031019.

[48] Z. Huang, Y. Ding, and C. B. Schroeder, "Compact x-ray free-electron laser from a laser-plasma accelerator using a transverse-gradient undulator", Physical Review Letters **109**, 204801 (2012) 10.1103/PhysRevLett.109.204801.

[49] K. Steiniger et al., "Optical free-electron lasers with traveling-wave Thomson-scattering", Journal of Physics B: Atomic, Molecular and Optical Physics **47**, 234011 (2014) 10.1088/0953-4075/47/23/234011.

[50] A. Martinez de la Ossa et al., "High-quality electron beams from beam-driven plasma accelerators by wakefield-induced ionization injection", Physical Review Letters **111** (2013) 10.1103/PhysRevLett.111.245003.

[51] A. Martinez de la Ossa et al., "Wakefield-induced ionization injection in beam-driven plasma accelerators", Physics of Plasmas **22**, 093107 (2015) 10.1063/1.4929921.

[52] S. van der Meer, "Improving the power efficiency of the plasma wakefield accelerator", in Clic note no. 3 (1985), CM–P00058040.

[53] T. Katsouleas et al., "Beam loading in plasma accelerators", Particle Accelerators **22**, 81–99 (1987).

[54] M. Tzoufras et al., "Beam loading in the nonlinear regime of plasma-based acceleration", Physical Review Letters **101**, 145002 (2008) 10.1103/PhysRevLett.101.145002.

[55] M. Tzoufras et al., "Beam loading by electrons in nonlinear plasma wakes", Physics of Plasmas **16**, 056705 (2009) 10.1063/1.3118628.

[56] P. Gibbon, *Short pulse laser interactions with matter: an introduction* (Imperial College Press, 2005).

[57] D. R. Lide, "CRC handbook of chemistry and physics, 84th edition", CRC Press (2003).

[58] L. V. Keldysh, "Ionization in the field of a strong electromagnetic wave", Soviet Physics JETP **20**, 1307–1314 (1965).

[59] M. V. Ammosov, N. B. Delone, and V. P. Krainov, "Tunnel ionization of complex atoms and of atomic ions in an alternating electromagnetic field", Soviet Physics JETP **64**, edited by J. A. Alcock, 1191–1194 (1986).

[60] N. B. Delone and V. P. Krainov, "Tunneling and barrier-suppression ionization of atoms and ions in a laser radiation field", Physics-Uspekhi **41**, 469–485 (1998) 10.1070/PU1998v041n05ABEH000393.

[61] E. Esarey et al., "Self-focusing and guiding of short laser pulses in ionizing gases and plasmas", IEEE Journal of Quantum Electronics **33**, 1879–1914 (1997) 10.1109/3.641305.

[62] B. Quesnel and P. Mora, "Theory and simulation of the interaction of ultraintense laser pulses with electrons in vacuum", Physical Review E **58**, 3719–3732 (1998) 10.1103/PhysRevE.58.3719.

[63] E. A. Startsev and C. J. McKinstrie, "Multiple scale derivation of the relativistic ponderomotive force", Physical Review E **55**, 7527–7535 (1997) 10.1103/PhysRevE.55.7527.

[64] M. Messmer, "Führung von laserstrahlen hoher intensität in plasmakanälen", MSc Thesis (Technische Universität Dresden, Nov. 2014).

[65] G.-Z. Sun et al., "Self-focusing of short intense pulses in plasmas", Physics of Fluids **30**, 526 (1987) 10.1063/1.866349.

[66] J. E. Ralph et al., "Self-guiding of ultrashort, relativistically intense laser pulses through underdense plasmas in the blowout regime", Physical Review Letters **102**, 1–4 (2009) 10.1103/PhysRevLett.102.175003.

[67] E. Esarey, C. Schroeder, and W. Leemans, "Physics of laser-driven plasma-based electron accelerators", Reviews of Modern Physics **81**, 1229–1285 (2009) 10.1103/RevModPhys.81.1229.

[68] C. D. Decker and W. B. Mori, "Group velocity of large-amplitude electromagnetic waves in a plasma", Physical Review E **51**, 1364–1375 (1995) 10.1103/PhysRevE.51.1364.

[69] P. Sprangle, E. Esarey, and A. Ting, "Nonlinear theory of intense laser-plasma interactions", Physical Review Letters **64**, 2011–2014 (1990) 10.1103/PhysRevLett.64.2011.

[70] P. Sprangle, E. Esarey, and A. Ting, "Nonlinear interaction of intense laser pulses in plasmas", Physical Review A **41**, 4463–4469 (1990) 10.1103/PhysRevA.41.4463.

[71] J. B. Rosenzweig et al., "Acceleration and focusing of electrons in two-dimensional nonlinear plasma wake fields", Physical Review A **44**, R6189–R6192 (1991) 10.1103/PhysRevA.44.R6189.

[72] W. Lu et al., "Nonlinear theory for relativistic plasma wakefields in the blowout regime", Physical Review Letters **96**, 1–4 (2006) 10.1103/PhysRevLett.96.165002.

[73] A. G. R. Thomas et al., "Effect of laser-focusing conditions on propagation and monoenergetic electron production in laser-wakefield accelerators", Physical Review Letters **98**, 2–5 (2007) 10.1103/PhysRevLett.98.095004.

[74] I. Kostyukov, A. Pukhov, and S. Kiselev, "Phenomenological theory of laser-plasma interaction in "bubble" regime", Physics of Plasmas **11**, 5256–5264 (2004) 10.1063/1.1799371.

[75] C. E. Clayton et al., "Self-mapping the longitudinal field structure of a nonlinear plasma accelerator cavity", Nature Communications **7**, 12483 (2016) 10.1038/ncomms12483.

[76] W. K. H. Panofsky and W. A. Wenzel, "Some considerations concerning the transverse deflection of charged particles in radio-frequency fields", Review of Scientific Instruments **27**, 967–967 (1956) 10.1063/1.1715427.

[77] X. L. Xu et al., "Phase-space dynamics of ionization injection in plasma-based accelerators", Physical Review Letters **112**, 035003 (2014) 10.1103/PhysRevLett.112.035003.

[78] P. Chen et al., "Acceleration of electrons by the interaction of a bunched electron beam with a plasma", Physical Review Letters **54**, 693–696 (1985) 10.1103/PhysRevLett.54.693.

[79] J. M. Dawson, "Nonlinear electron oscillations in a cold plasma", Physical Review **113**, 383–387 (1959) 10.1103/PhysRev.113.383.

[80] A. I. Akhiezer and R. V. Polovin, "Theory of wave motion of an electron plasma", JETP Letters **3**, 696–705 (1959).

[81] R. J. Kingham and A. R. Bell, "Enhanced wakefields for the 1D laser wakefield accelerator", Physical Review Letters **79**, 4810–4813 (1997) 10.1103/PhysRevLett.79.4810.

[82] W. Lu et al., "A nonlinear theory for multidimensional relativistic plasma wave wakefields", Physics of Plasmas **13**, 056709 (2006) 10.1063/1.2203364.

[83] M. Everett et al., "Trapped electron acceleration by a laser-driven relativistic plasma wave", Nature **368**, 527–529 (1994) 10.1038/368527a0.

[84] F. Amiranoff et al., "Observation of laser wakefield acceleration of electrons", Physical Review Letters **81**, 995–998 (1998) 10.1103/PhysRevLett.81.995.

[85] M. Kando et al., "Experimental results of laser wakefield acceleration using a femtosecond terawatt laser pulse", Japanese Journal of Applied Physics **38**, L967–L969 (1999) 10.1143/JJAP.38.L967.

[86] A. Irman et al., "Design and simulation of laser wakefield acceleration with external electron bunch injection in front of the laser pulse", Journal of Applied Physics **102**, 024513 (2007) 10.1063/1.2759878.

[87] A. G. Khachatryan et al., "Conceptual design of a laser wakefield acceleration experiment with external bunch injection", Nuclear Instruments and Methods in Physics Research, Section A: Accelerators, Spectrometers, Detectors and Associated Equipment **566**, 244–249 (2006) 10.1016/j.nima.2006.07.007.

[88] A. G. Khachatryan et al., "Extremely short relativistic-electron-bunch generation in the laser wakefield via novel bunch injection scheme", Physical Review Special Topics - Accelerators and Beams **7**, 121301 (2004) 10.1103/PhysRevSTAB.7.121301.

[89] A. Irman, "Integral design of a laser wakefield accelerator with external bunch injection", PhD thesis (University of Twente, 2009), 10.3990/1.9789036528061.

[90] M. Luttikhof et al., "Electron bunch injection at an angle into a laser wakefield", Laser and Particle Beams **27**, 69 (2009) 10.1017/S0263034609000093.

[91] M. Luttikhof, "Theoretical investigation of external injection schemes for laser wakefield acceleration", PhD thesis (University of Twente, Enschede, The Netherlands, Sept. 2010), 10.3990/1.9789036530712.

[92] S. Bulanov et al., "Particle injection into the wave acceleration phase due to nonlinear wake wave breaking", Physical Review E **58**, R5257–R5260 (1998) 10.1103/PhysRevE.58.R5257.

[93] F. S. Tsung et al., "Near-GeV-energy laser-wakefield acceleration of self-injected electrons in a centimeter-scale plasma channel", Physical Review Letters **93**, 185002 (2004) 10.1103/PhysRevLett.93.185002.

[94] S. Kneip et al., "Near-GeV acceleration of electrons by a nonlinear plasma wave driven by a self-guided laser pulse", Physical Review Letters **103**, 8–11 (2009) 10.1103/PhysRevLett.103.035002.

[95] H. Suk et al., "Plasma electron trapping and acceleration in a plasma wake field using a density transition", Physical Review Letters **86**, 1011–1014 (2001) 10.1103/PhysRevLett.86.1011.

[96] C. G. R. Geddes et al., "Plasma-density-gradient injection of low absolute-momentum-spread electron bunches", Physical Review Letters **100**, 215004 (2008) 10.1103/PhysRevLett.100.215004.

[97] J. Faure et al., "Injection and acceleration of quasimonoenergetic relativistic electron beams using density gradients at the edges of a plasma channel", Physics of Plasmas **17**, 083107 (2010) 10.1063/1.3469581.

[98] K. Schmid et al., "Density-transition based electron injector for laser driven wakefield accelerators", Physical Review Special Topics - Accelerators and Beams **13**, 1–5 (2010) 10.1103/PhysRevSTAB.13.091301.

[99] A. Buck et al., "Shock-front injector for high-quality laser-plasma acceleration", Physical Review Letters **110**, 185006 (2013) 10.1103/PhysRevLett.110.185006.

[100] K. K. Swanson et al., "Control of tunable, monoenergetic laser-plasma-accelerated electron beams using a shock-induced density downramp injector", Physical Review Accelerators and Beams **20**, 051301 (2017) 10.1103/PhysRevAccelBeams.20.051301.

[101] E. Esarey et al., "Electron injection into plasma wakefields by colliding laser pulses", Physical Review Letters **79**, 2682–2685 (1997) 10.1103/PhysRevLett.79.2682.

[102] J. Faure et al., "Controlled injection and acceleration of electrons in plasma wakefields by colliding laser pulses", Nature **444**, 737–739 (2006) 10.1038/nature05393.

[103] H. Kotaki et al., "Head-on injection of a high quality electron beam by the interaction of two laser pulses", Physics of Plasmas **11**, 3296–3302 (2004) 10.1063/1.1751171.

[104] A. Pak et al., "Injection and trapping of tunnel-ionized electrons into laser-produced wakes", Physical Review Letters **104**, 025003 (2010) 10.1103/PhysRevLett.104.025003.

[105] C. McGuffey et al., "Ionization induced trapping in a laser wakefield accelerator", Physical Review Letters **104**, 025004 (2010) 10.1103/PhysRevLett.104.025004.

[106] M. Chen et al., "Theory of ionization-induced trapping in laser-plasma accelerators", Physics of Plasmas **19**, 033101 (2012) 10.1063/1.3689922.

[107] C. E. Clayton et al., "Self-guided laser wakefield acceleration beyond 1 gev using ionization-induced injection", Physical Review Letters **105**, 105003 (2010) 10.1103/PhysRevLett.105.105003.

[108] T. L. Audet et al., "Investigation of ionization-induced electron injection in a wakefield driven by laser inside a gas cell", Physics of Plasmas **23** (2016) 10.1063/1.4942033.

[109] M. Zeng et al., "Self-truncated ionization injection and consequent monoenergetic electron bunches in laser wakefield acceleration", Physics of Plasmas **21**, 030701 (2014) 10.1063/1.4868404.

[110] M. Mirzaie et al., "Demonstration of self-truncated ionization injection for GeV electron beams", Scientific Reports **5**, 14659 (2015) 10.1038/srep14659.

[111] N. A. Hafz et al., "Generation of high-quality electron beams by ionization injection in a single acceleration stage", High Power Laser Science and Engineering **4**, e24 (2016) 10.1017/hpl.2016.25.

[112] E. Guillaume et al., "Physics of fully-loaded laser-plasma accelerators", Physical Review Special Topics - Accelerators and Beams **18**, 061301 (2015) 10.1103/PhysRevSTAB.18.061301.

[113] E. Oz et al., "Ionization-induced electron trapping in ultrarelativistic plasma wakes", Physical Review Letters **98**, 084801 (2007) 10.1103/PhysRevLett.98.084801.

[114] M. Tzoufras, "Generation of multi-giga-electron-volt monoenergetic electron beams via laser wakefield acceleration", PhD thesis (University of California, 2008).

[115] F. Gabriel et al., "The Rossendorf radiation source ELBE and its FEL projects", Nuclear Instruments and Methods in Physics Research Section B: Beam Interactions with Materials and Atoms **161-163**, 1143–1147 (2000) 10.1016/S0168-583X(99)00909-X.

[116] M. Siebold et al., "PEnELOPE: a high peak-power diode-pumped laser system for laser-plasma experiments", in Proceedings of SPIE, Vol. 8780, 3049 (May 2013), p. 878005, 10.1117/12.2017522.

[117] A. Jochmann, "Development and characterization of a tunable ultrafast x-ray source via inverse-compton-scattering", PhD thesis (Technische Universität Dresden, 2014).

[118] A. Jullien et al., "10^(-10)temporal contrast for femtosecond ultraintense lasers by cross-polarized wave generation", Optics Letters **30**, 920 (2005) 10.1364/OL.30.000920.

[119] Y. Petit et al., "1-J white-light continuum from 100-TW laser pulses", Physical Review A **83**, 013805 (2011) 10.1103/PhysRevA.83.013805.

[120] K. Schmid and L. Veisz, "Supersonic gas jets for laser-plasma experiments", Review of Scientific Instruments **83**, 053304 (2012) 10.1063/1.4719915.

[121] V. Malka et al., "Characterization of neutral density profile in a wide range of pressure of cylindrical pulsed gas jets", Review of Scientific Instruments **71**, 2329 (2000) 10.1063/1.1150619.

[122] N. Lemos et al., "Design and characterization of supersonic nozzles for wide focus laser-plasma interactions.", The Review of scientific instruments **80**, 103301 (2009) 10.1063/1.3233895.

[123] B. E. A. Saleh and M. C. Teich, *Fundamentals of photonics* (Wiley-Interscience Publication, 1991).

[124] G. Pretzier, H. Jager, and T. Neger, "High-accuracy differential interferometry for the investigation of phase objects", Measurement Science and Technology **4**, 649–658 (1993) 10.1088/0957-0233/4/6/003.

[125] M. Takeda, H. Ina, and S. Kobayashi, "Fourier-transform method of fringe-pattern analysis for computer-based topography and interferometry", Journal of the Optical Society of America **72**, 156 (1982) 10.1364/JOSA.72.000156.

[126] M. Hipp and P. Reiterer, *User manual for IDEA 1.7*, Chapter 3.6; Abel Inversion, Institut fur Experimental Physik, Technische Universitat Graz (July 2003).

[127] *IDEA - interferometric data evaluation algorithms, software for fringe analysis and phase data reduction*, http://www.optics.tugraz.at/idea/idea.html, Accessed: 2015-09-22.

[128] A. C. Kak and M. Slaney, *Principles of computerized tomographic imaging* (Society of Industrial and Applied Mathematics, 2001).

[129] F. Harris, "On the use of windows for harmonic analysis with the discrete fourier transform", Proceedings of the IEEE **66**, 51–83 (1978) 10.1109/PROC.1978.10837.

[130] E. Wolf, ed., *Progress in optics*, Vol. 43 (Elsevier Science, 2002).

[131] L. Lorenz, "Über die refractionsconstante", Ann. Phys. **11**, 70–103 (1880) 10.1002/andp.18802470905.

[132] H. A. Lorentz, "Über die beziehung zwischen der fortpflanzungsgeschwindigkeit des lichtes und der körperdichte", Ann. Phys. **9**, 641–645 (1880) 10.1002/andp.18802450406.

[133] M. J. Weber, *Handbook of optical materials* (CRC Press, 2002).

[134] T. A. W. Wolterink, "High-gradient gas-jet targets for laser wakefield acceleration", MSc Thesis (University of Twente, Apr. 2011).

[135] J. P. Couperus, "Laser wakefield acceleration in the nonlinear bubble regime and gas-jet target characterization", MSc Thesis (University of Twente, 2011).

[136] A. Köhler, "Charakterisierung von plasmatargets für laser wakefield experimente", Diplom Thesis (Technische Universität Dresden, Feb. 2013).

[137] B. Landgraf et al., "High resolution 3D gas-jet characterization", Review of Scientific Instruments **82**, 083106 (2011) 10.1063/1.3624694.

[138] K. Schmid, "Supersonic micro-jets and their application to few-cycle laser-driven electron acceleration", PhD thesis (Ludwig Maximilians Universität München, 2009).

[139] *Vacuumschmelze VACODUM 764 TP*, http://www.vacuumschmelze.com/en/products/permanent-magnets-assemblies/permanent-magnets/nd-fe-b/vacodym/vacodym-764-tp.html, accessed 15-Februar-2017.

[140] K. Brown, *A first and second order matrix theory for the design of beam transport systems and charged particle spectrometers*, tech. rep. SLAC-75 (Stanford University, California, May 1982), pp. 71–134.

[141] *Pulsar Physics, General Particle Tracer, version 3.01*, http://www.pulsar.nl/gpt.

[142] R. Morlotti et al., "Intrinsic conversion efficiency of X-rays to light in Gd2O2S : Tb3+ powder phosphors", Journal of Luminescence **72-74**, 772–774 (1997) 10.1016/S0022-2313(96)00330-4.

[143] K. A. Tanaka et al., "Calibration of imaging plate for high energy electron spectrometer", Review of Scientific Instruments **76**, 013507 (2005) 10.1063/1.1824371.

[144] K. Zeil et al., "Absolute response of Fuji imaging plate detectors to picosecond-electron bunches", Review of Scientific Instruments **81**, 013307 (2010) 10.1063/1.3284524.

[145] T. Bonnet et al., "Response functions of imaging plates to photons, electrons and 4He particles", Review of Scientific Instruments **84**, 103510 (2013) 10.1063/1.4826084.

[146] Y. Glinec et al., "Absolute calibration for a broad range single shot electron spectrometer", Review of Scientific Instruments **77**, 103301 (2006) 10.1063/1.2360988.

[147] A. Buck et al., "Absolute charge calibration of scintillating screens for relativistic electron detection", Review of Scientific Instruments **81**, 033301 (2010) 10.1063/1.3310275.

[148] K. Nakamura et al., "Electron beam charge diagnostics for laser plasma accelerators", Physical Review Special Topics - Accelerators and Beams **14**, 062801 (2011) 10.1103/PhysRevSTAB.14.062801.

[149] S. Masuda et al., "Absolute calibration of an electron spectrometer using high energy electrons produced by the laser-plasma interaction", Review of Scientific Instruments **79** (2008) 10.1063/1.2969655.

[150] B. Yang, *A design report for the optical transition radiation imager for the LCLS undulator*, tech. rep. LCLS Note, LCLS-TN-05-21 (2005), pp. 1–19.

[151] B. Hidding et al., "Novel method for characterizing relativistic electron beams in a harsh laser-plasma environment", Review of Scientific Instruments **78** (2007) 10.1063/1.2775668.

[152] Y. C. Wu et al., "Note: absolute calibration of two DRZ phosphor screens using ultrashort electron bunch", Review of Scientific Instruments **83**, 026101 (2012) 10.1063/1.3681442.

[153] G. E. Giakoumakis and D. M. Miliotis, "Light angular distribution of fluorescent screens excited by x-rays", Physics in Medicine and Biology **30**, 21–29 (1985) 10.1088/0031-9155/30/1/003.

[154] B. B. Pollock et al., "Demonstration of a narrow energy spread, ˜0.5 GeV electron beam from a two-stage laser wakefield accelerator.", Physical review letters **107**, 045001 (2011) 10.1103/PhysRevLett.107.045001.

[155] J. S. Liu et al., "All-optical cascaded laser wakefield accelerator using ionization-induced injection", Physical Review Letters **107**, 035001 (2011) 10.1103/PhysRevLett.107.035001.

[156] C. Thaury et al., "Shock assisted ionization injection in laser-plasma accelerators.", Scientific reports **5**, 16310 (2015) 10.1038/srep16310.

[157] S. Li et al., "Enhanced single-stage laser-driven electron acceleration by self-controlled ionization injection", Optics Express **22**, 29578 (2014) 10.1364/OE.22.029578.

[158] C. Xia et al., "Effects of self-focusing on tunnel-ionization-induced injection in a laser wakefield accelerator", Physics of Plasmas **18**, 113101 (2011) 10.1063/1.3656958.

[159] A. Popp et al., "All-optical steering of laser-wakefield-accelerated electron beams", Physical Review Letters **105** (2010) 10.1103/PhysRevLett.105.215001.

[160] M. Schnell et al., "Optical control of hard X-ray polarization by electron injection in a laser wakefield accelerator.", Nature communications **4**, 2421 (2013) 10.1038/ncomms3421.

[161] N. Dimitrov et al., "Pulse front tilt measurement of femtosecond laser pulses", Optics Communications **371**, 51–58 (2016) 10.1016/j.optcom.2016.03.054.

[162] F. Grasbon et al., "Femtosecond interferometric autocorrelations in the presence of pulse-front distortions", in Proceedings of spie - the international society for optical engineering, Vol. 3571, edited by P. A. Atanasov and D. V. Stoyanov (May 1999), p. 164, 10.1117/12.347610.

[163] A. Trisorio et al., "Self-referenced spectral interferometry for ultrashort infrared pulse characterization", Optics Letters **37**, 2892 (2012) 10.1364/OL.37.002892.

[164] P. Tournois, "Acousto-optic programmable dispersive filter for adaptive compensation of group delay time dispersion in laser systems", Optics Communications **140**, 245–249 (1997) 10.1016/S0030-4018(97)00153-3.

[165] C. Iaconis and I. A. Walmsley, "Spectral phase interferometry for direct electric-field reconstruction of ultrashort optical pulses.", Optics letters **23**, 792–794 (1998) 10.1109/CLEO.1998.676573.

[166] J. Schreiber et al., "Complete temporal characterization of asymmetric pulse compression in a laser wakefield", Physical Review Letters **105**, 235003 (2010) 10.1103/PhysRevLett.105.235003.

[167] J. Faure et al., "Observation of laser-pulse shortening in nonlinear plasma waves", Physical Review Letters **95**, 205003 (2005) 10.1103/PhysRevLett.95.205003.

[168] D. F. Gordon et al., "Asymmetric self-phase modulation and compression of short laser pulses in plasma channels", Physical Review Letters **90**, 215001 (2003) 10.1103/PhysRevLett.90.215001.

[169] X. Zhang et al., "Effect of pulse profile and chirp on a laser wakefield generation", Physics of Plasmas **19**, 053103 (2012) 10.1063/1.4714610.

[170] V. B. Pathak et al., "Effect of the frequency chirp on laser wakefield acceleration", New Journal of Physics **14**, 023057 (2012) 10.1088/1367-2630/14/2/023057.

[171] C. Liu et al., "Adaptive-feedback spectral-phase control for interactions with transform-limited ultrashort high-power laser pulses", Optics Letters **39**, 80 (2014) 10.1364/OL.39.000080.

[172] H. T. Kim et al., "Stable multi-GeV electron accelerator driven by waveform-controlled PW laser pulses", Scientific Reports **7**, 10203 (2017) 10.1038/s41598-017-09267-1.

[173] J. Primot and N. Guérineau, "Extended hartmann test based on the pseudoguiding property of a hartmann mask completed by a phase chessboard.", Applied optics **39**, 5715–5720 (2000) 10.1364/AO.39.005715.

[174] Z. Li et al., "Single-shot visualization of evolving laser wakefields using an all-optical streak camera", Physical Review Letters **113**, 1–5 (2014) 10.1103/PhysRevLett.113.085001.

[175] C. J. Zhang et al., "Capturing relativistic wakefield structures in plasmas using ultrashort high-energy electrons as a probe", Scientific Reports **6**, 29485 (2016) 10.1038/srep29485.

[176] C. J. Zhang et al., "Femtosecond probing of plasma wakefields and observation of the plasma wake reversal using a relativistic electron bunch", Physical Review Letters **119**, 064801 (2017) 10.1103/PhysRevLett.119.064801.

[177] A. Buck, "Advanced characterization and control of laser wakefield acceleration", PhD thesis (Ludwig–Maximilians–Universität Munich, 2011).

[178] S. I. Bajlekov et al., "Longitudinal electron bunch profile reconstruction by performing phase retrieval on coherent transition radiation spectra", Physical Review Special Topics - Accelerators and Beams **16**, 040701 (2013) 10.1103/PhysRevSTAB.16.040701.

[179] J. van Tilborg et al., "Temporal characterization of femtosecond laser-plasma-accelerated electron bunches using terahertz radiation", Physical Review Letters **96**, 014801 (2006) 10.1103/PhysRevLett.96.014801.

[180] A. D. Debus et al., "Electron bunch length measurements from laser-accelerated electrons using single-shot THz time-domain interferometry", Physical Review Letters **104**, 084802 (2010) 10.1103/PhysRevLett.104.084802.

[181] O. Zarini, "Entwicklung eines breitbandigen optischen spektrometers zur pulsdauermessung ultrakurzer elektronenpulse", Diplom Thesis (Technische Universität Dresden, 2013).

[182] C. Rechatin et al., "Observation of beam loading in a laser-plasma accelerator", Physical Review Letters **103**, 194804 (2009) 10.1103/PhysRevLett.103.194804.

[183] K. Chouffani et al., "Determination of electron beam parameters by means of laser-compton scattering", Physical Review Special Topics - Accelerators and Beams **9**, 050701 (2006) 10.1103/PhysRevSTAB.9.050701.

[184] H. Burau et al., "PIConGPU: a fully relativistic particle-in-cell code for a GPU cluster", IEEE Transactions on Plasma Science **38**, 2831–2839 (2010) 10.1109/TPS.2010.2064310.

[185] M. Bussmann et al., "Radiative signatures of the relativistic Kelvin-Helmholtz instability", in Proceedings of the international conference for high performance computing, networking, storage and analysis on - sc '13 (2013), pp. 1–12, 10.1145/2503210.2504564.

[186] K. T. Phuoc et al., "Imaging electron trajectories in a laser-wakefield cavity using betatron X-ray radiation", Physical Review Letters **97**, 225002 (2006) 10.1103/PhysRevLett.97.225002.

[187] G. R. Plateau et al., "Low-emittance electron bunches from a laser-plasma accelerator measured using single-shot X-ray spectroscopy", Physical Review Letters **109**, 064802 (2012) 10.1103/PhysRevLett.109.064802.

[188] S. Kneip et al., "Characterization of transverse beam emittance of electrons from a laser-plasma wakefield accelerator in the bubble regime using betatron x-ray radiation", Physical Review Special Topics - Accelerators and Beams **15**, 2–6 (2012) 10.1103/PhysRevSTAB.15.021302.

[189] M. Schnell et al., "Deducing the electron-beam diameter in a laser-plasma accelerator using X-ray betatron radiation", Physical Review Letters **108**, 075001 (2012) 10.1103/PhysRevLett.108.075001.

[190] G. Golovin et al., "Intrinsic beam emittance of laser-accelerated electrons measured by x-ray spectroscopic imaging", Scientific Reports **6**, 24622 (2016) 10.1038/srep24622.

[191] X. L. Xu et al., "Physics of phase space matching for staging plasma and traditional accelerator components using longitudinally tailored plasma profiles", Physical Review Letters **116**, 124801 (2016) 10.1103/PhysRevLett.116.124801.

[192] M. Migliorati et al., "Intrinsic normalized emittance growth in laser-driven electron accelerators", Physical Review Special Topics - Accelerators and Beams **16**, 011302 (2013) 10.1103/PhysRevSTAB.16.011302.

[193] E. Brunetti et al., "Low emittance, high brilliance relativistic electron beams from a laser-plasma accelerator", Physical Review Letters **105**, 3–6 (2010) 10.1103/PhysRevLett.105.215007.

[194] A. G. Khachatryan et al., "Femtosecond electron-bunch dynamics in laser wakefields and vacuum", Physical Review Special Topics - Accelerators and Beams **10**, 1–13 (2007) 10.1103/PhysRevSTAB.10.121301.

[195] A. W. Chao et al., "Space charge dynamics of bright electron beams", Physical Review Special Topics - Accelerators and Beams **6**, 19–32 (2003) 10.1103/PhysRevSTAB.6.024201.

[196] J. Wenz et al., "Quantitative X-ray phase-contrast microtomography from a compact laser-driven betatron source", Nature Communications **6**, 7568 (2015) 10.1038/ncomms8568.

[197] K. Steiniger et al., "Wave optical description of the traveling-wave Thomson-scattering optical undulator field and its application to the TWTS-FEL", Nuclear Instruments and Methods in Physics Research Section A: Accelerators, Spectrometers, Detectors and Associated Equipment **740**, 147–152 (2014) 10.1016/j.nima.2013.10.091.

[198] K. Steiniger, "High-yield optical undulators scalable to optical free-electron laser operation by traveling-wave Thomson-scattering", PhD thesis (Technische Universität Dresden, 2018), 10.5281/zenodo.439523.

[199] A. Martinez de la Ossa et al., "High-quality electron beams from field-induced ionization injection in the strong blow-out regime of beam-driven plasma accelerators", Nuclear Instruments and Methods in Physics Research, Section A: Accelerators, Spectrometers, Detectors and Associated Equipment **740**, 231–235 (2014) 10.1016/j.nima.2013.10.016.

[200] A. Huebl et al., *PIConGPU 0.2.0: Beta Release - Full Multiple Species Support & openPMD*, Nov. 2016, 10.5281/zenodo.168390.

[201] Kane Yee, "Numerical solution of initial boundary value problems involving maxwell's equations in isotropic media", IEEE Transactions on Antennas and Propagation **14**, 302–307 (1966) 10.1109/TAP.1966.1138693.

[202] J.-L. Vay et al., "Novel methods in the particle-in-cell accelerator code-framework warp", Computational Science & Discovery **5**, 014019 (2012) 10.1088/1749-4699/5/1/014019.

[203] T. Esirkepov, "Exact charge conservation scheme for particle-in-cell simulation with an arbitrary form-factor", Computer Physics Communications **135**, 144–153 (2001) 10.1016/S0010-4655(00)00228-9.

[204] R. W. Hockney and J. W. Eastwood, *Computer simulation using particles* (CRC Press, 1988).

[205] P. Mulser and D. Bauer, *High power laser-matter interaction*, Vol. 238 (Springer Science & Business Media, 2010).

APPENDIX A.

SUPPLEMENTARY FIGURES

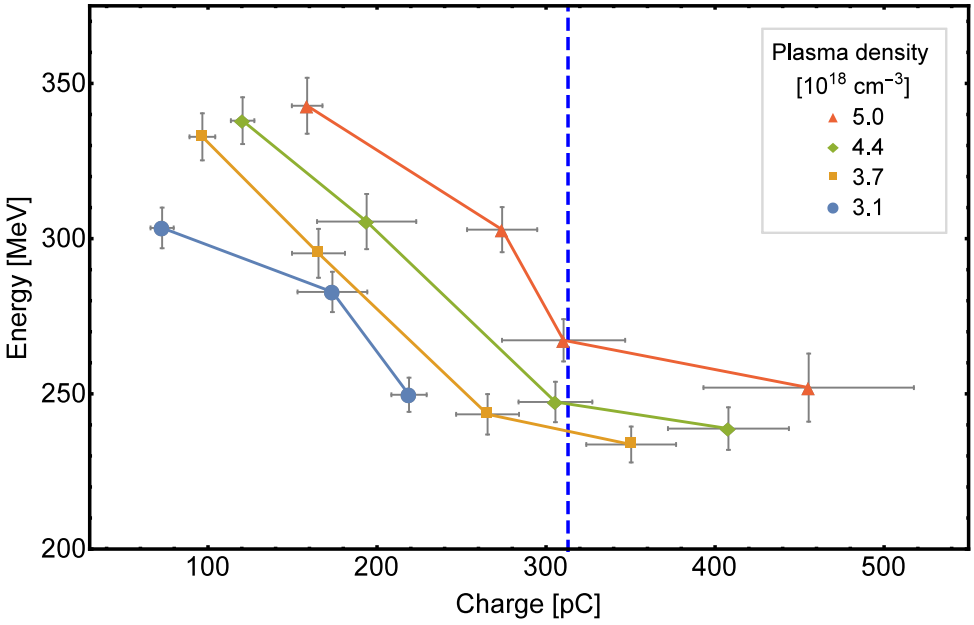

Figure A.1.: **Mean peak electron energy dependency.** Supplementary to figure 5.2. Dependency with respect to both charge within the FWHM of the energy peak as well as plasma density is shown. This figure is similar to figure 5.2 except that it shows the mean peak electron energy instead of E_{max}. Data points represent the mean value from a set of shots (sample size between seven to twenty) at equal experimental parameters. Connected data points show a set of equal plasma density. The error bars represent the standard error of the mean. The estimated optimal load according to equation (2.49) of 313 pC is indicated by the dashed vertical line.

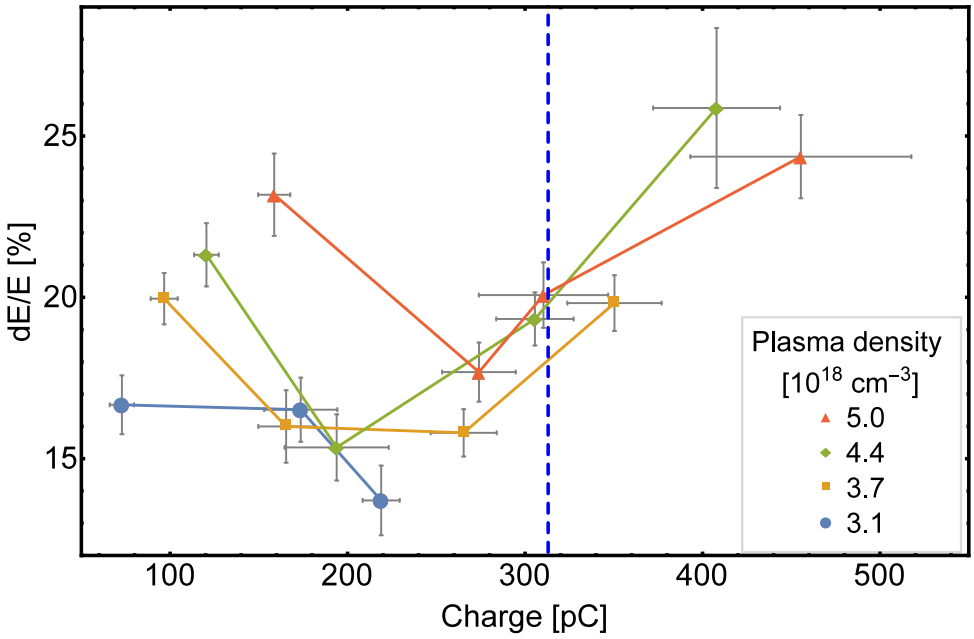

Figure A.2.: **Beam energy spread relative to the mean peak energy.** Supplementary to figure 5.3 Dependency with respect to both charge within the FWHM of the energy peak as well as plasma density is shown. Data points represent the mean value from a set of shots (sample size between seven to twenty) at equal experimental parameters. Connected data points show a set of equal plasma density. The error bars represent the standard error of the mean. The estimated optimal load according to equation (2.49) of 313 pC is indicated by the dashed vertical line.

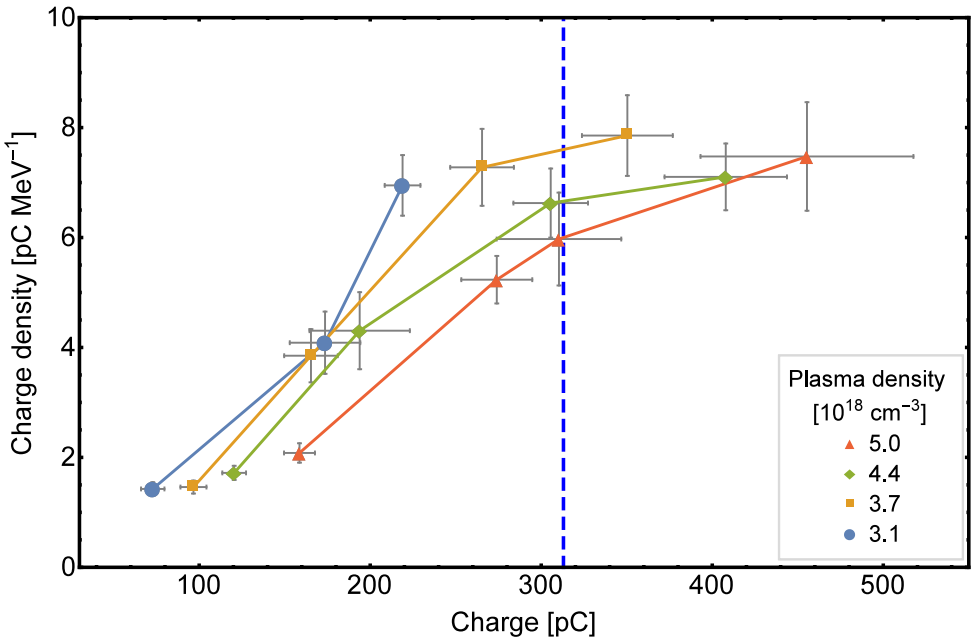

Figure A.3.: **Charge density within the peak FWHM dependency on injected charge.** Supplementary to figure 5.6. The error bars represent the standard error of the mean. The estimated optimal load according to equation (2.49) of 313 pC is indicated by the dashed vertical line.

APPENDIX B.

PARTICLE-IN-CELL SIMULATIONS

Particle-in-cell simulations were set-up and intitialised by Richard Pausch and Alexander Debus on the PIConGPU code[184,185] using a 0.2.0 pre-release[200]. Analysis of the PIC results was partially performed by Richard Pausch, specifically results shown in figures 4.9, 5.8, 5.9, 5.4 & 5.5.

The simulation box used consists of 704×704×2352 cells with a transversal resolution of $\Delta x = \Delta y = 177\,\text{nm}$ and longitudinal resolution of $\Delta z = 44.3\,\text{nm}$ thus resulting in a temporal resolution of $\Delta t = 0.1393\,\text{fs}$. The electric and magnetic field evolution is computed via the field solver by Yee[201] while macro particles are propagated using the particle pusher by Vay[202]. The current is calculated using the Esirkepov current deposition scheme[203] with a triangular-shaped density cloud (TSC) interpolation[204]. In order to incorporate ionization into the particle-in-cell cycle, similar simulations were performed using the BSI[205] and ADK[60] ionization methods. The results of the both ionization methods show good agreement for our setup, thus BSI was selected for performance reasons. By artificially increasing the doping concentration in simulations, we were able to study beam loading effects up to 168 pC of injected charge in the peak. The plasma density was modelled according to the experimentally determined density profile of the gas target used. For the simulations presented in this thesis, the electron density was set to reach $n_e = 2.62\times10^{18}\,\text{cm}^{-3}$ after ionization, independent of the doping used. The laser with wavelength $\lambda = 800\,\text{nm}$ was modelled using a Gaussian envelope both transversally and temporally and reached a vacuum peak intensity of $a_0 = 2.8$ in focus. The pulse duration was set to $\tau = 30\,\text{fs}$ and the spot size to $w_0 = 19\,\mu\text{m}$ (both FWHM of intensity).

APPENDIX C.

CHARGE REQUIRED FOR OPTIMAL LOADING

Taking equation (2.45):

$$Q_s\,[\mathrm{nC}]\,\frac{eE_s}{m_e c\omega_p} \simeq 0.047\sqrt{\frac{10^{16}}{n_p\,[\mathrm{cm}^{-3}]}}(k_p R_b)^4, \tag{C.1}$$

and choosing

$$E_s = E_{max} \tag{C.2}$$

we can rewrite equation (2.27) to

$$\frac{eE_s}{m_e c\omega_p} = \frac{k_p R_b}{2} \simeq \sqrt{a_0}. \tag{C.3}$$

Which assumes the matched spot size condition from equation (2.25)

$$k_p w_0 \simeq k_p R_b = 2\sqrt{a_0}. \tag{C.4}$$

Now combining these equations gives:

$$Q_s\,[\mathrm{nC}] \simeq \frac{0.047}{\sqrt{a_0}} \cdot \sqrt{\frac{10^{16}}{n_p\,[\mathrm{cm}^{-3}]}} \cdot \left(2\sqrt{a_0}\right)^4 \tag{C.5}$$

$$Q_s\,[\mathrm{nC}] \simeq 0.752 \cdot (a_0)^{1.5} \cdot \sqrt{\frac{10^{16}}{n_p\,[\mathrm{cm}^{-3}]}} \tag{C.6}$$

from ref.[38]:

$$a_0 \simeq 2\left(P/P_c\right)^{(1/3)}, \tag{C.7}$$

follows

$$Q_s\,[\mathrm{nC}] \simeq 1.504 \cdot \sqrt{2} \cdot \sqrt{P/P_c} \cdot \sqrt{\frac{10^{16}}{n_p\,[\mathrm{cm}^{-3}]}}. \tag{C.8}$$

Taking equation (2.14):

$$P_c[\mathrm{GW}] = 17\left(\omega_0/\omega_p\right)^2, \tag{C.9}$$

gives

$$Q_s\left[\mathrm{nC}\right] \simeq 1.504 \cdot \sqrt{2} \cdot \sqrt{\frac{P\left[\mathrm{GW}\right]}{17\left(\omega_0/\omega_p\right)^2}} \cdot \sqrt{\frac{10^{16}}{n_p\left[\mathrm{cm}^{-3}\right]}} \tag{C.10}$$

The plasma frequency is given by equation (2.13):

$$\omega_p = \sqrt{\frac{n_p\left[\mathrm{m}^{-3}\right] e^2}{m_e \epsilon_0}} \tag{C.11}$$

leading to

$$Q_s\left[\mathrm{nC}\right] \simeq \frac{1.504}{\omega_0} \cdot \sqrt{\frac{2 n_p\left[\mathrm{m}^{-3}\right] e^2 10^{16}}{17 m_e \epsilon_0 n_p\left[\mathrm{cm}^{-3}\right]}} \cdot \sqrt{P\left[\mathrm{GW}\right]} \tag{C.12}$$

or

$$Q_s\left[\mathrm{nC}\right] \simeq \frac{1.504}{\omega_0} \cdot \sqrt{\frac{2 \cdot 10^{22} \cdot e^2}{17 m_e \epsilon_0}} \cdot \sqrt{P\left[\mathrm{GW}\right]} \tag{C.13}$$

Or in Gaussian units:

$$Q_s\left[\mathrm{nC}\right] \simeq \frac{1.504}{\omega_0} \cdot \sqrt{\frac{8 \cdot \pi \cdot 10^{16} \cdot e^2}{17 m_e}} \cdot \sqrt{P\left[\mathrm{GW}\right]} \tag{C.14}$$

APPENDIX D.

NOZZLE DESIGN

The nozzle for providing the accelerating medium for the LPA presented in this thesis was designed by Tom Wolterink as part of his MSc thesis "*High-gradient gas-jet targets for laser wakefield acceleration*"[134].

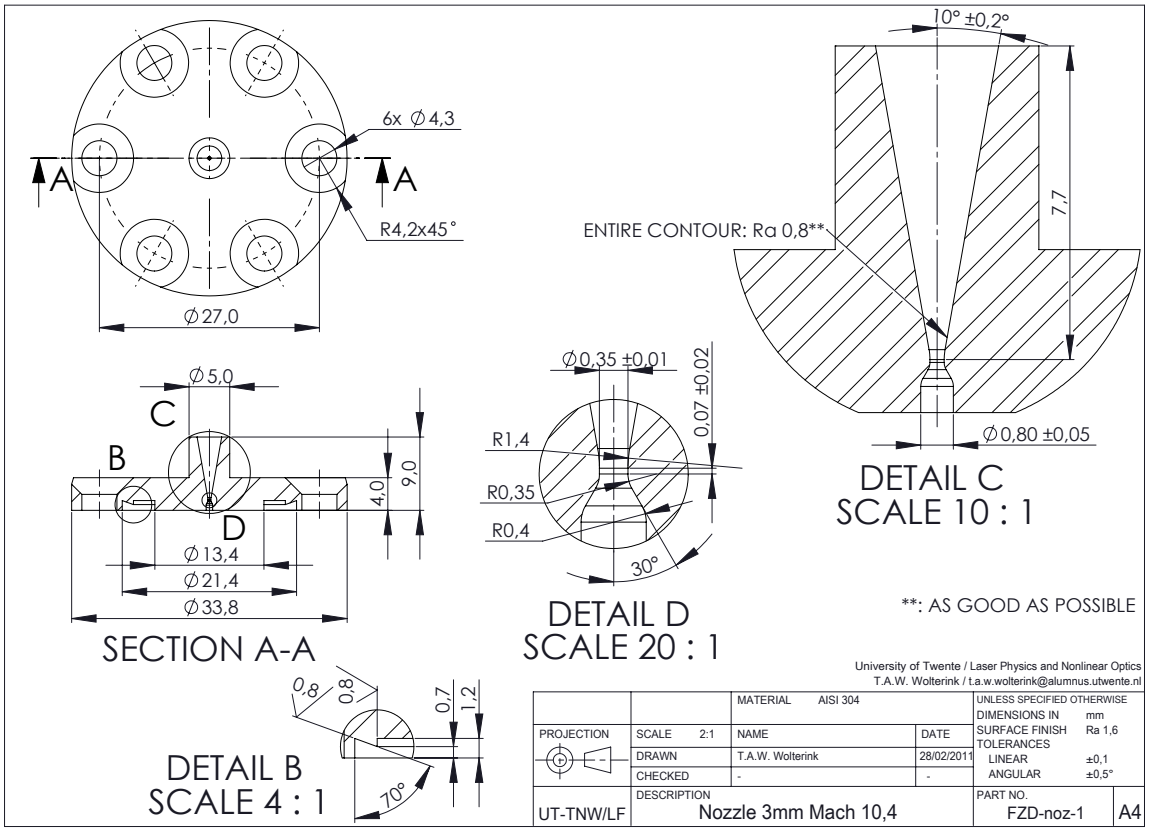

ACKNOWLEDGEMENTS

It has been a long road from starting the graduation process to the finalisation of this thesis. Looking back, I think I was not fully aware of all the challenges on the way when I started it. The road has taken a couple of unexpected turns, some detours and partially went over bumpy unpaved roads. But all together is has been a great and enlightening experience, mostly because of all the people who have supported me in so many different ways along the road. Without their help I would not have been able to come this far and I would like to thank everyone for their support.

First I would like to thank all the members of *team electrons*. I am grateful that I can work in such a wonderful team. If it weren't for Arie, Alex & Omid we would have never managed to go from an empty lab to the cool experiments we're doing now. Thank you for the collaboration, the hard work and long beam-times which have enabled me to write this work to begin with. Arie, you are the hardest working post-doc I know and I would have been lost without all the help and guidance you gave me over these years. Thank you also for reading and correcting this thesis. Much appreciated! I also want to thank the members of team electrons who joined us later on. Jakob, thank you for all the discussions and insights, both at work and beside it, the beam-times and for showing that sleep is for the weak. Thomas I have to thank for all the effort he put in the scintillator screen calibration, which seemed to be an easy task in the beginning, but in the end turned out to be not that simple. Thank you for all the work there, which has been vital for this thesis. Axel, now emeritus member of team electrons, gave me guidance, showed me around and got me started when I came as a young scientist to Dresden. Without your help and friendship I would not have started on this path. Thank you!

I want to thank both directors of the institute of radiation physics, Thomas Cowan and Ulrich Schramm for enabling me to do my PhD work at the HZDR. Thank you for setting up such a wonderful institute where such exciting science takes place. Thank you Tom for showing such passion for science, the parties and the fireworks. Thank you Uli for always keeping your door open, for all the advice and all the hard work that made these experiments possible.

Many thanks go to the PIConGPU team, their work contributed so much to understanding my experiments. So many people work on this that I can not name them all here. But special thanks go to Richard and Alexander, who relentlessly made the computer clusters work such that we could make sense of what happened in experiment. Thank you so much for all the work, insights and discussions.

The infrastructure behind the experiments in this thesis is huge and many people have played a role in setting these up, keeping them running or supporting it in any other way. René, Uwe, Stefan and also Karl, many thanks for all the work on the DRACO laser system, this thesis wouldn't be here if it weren't for you.

Simon, Christoph and Manfred did so much work in design, electronics, construction and many other things. Without their help, 111c would still be half-empty and I would still be clueless in many things. Thank you.

The in-house workshop made many things happen and my life so much easier. Without them everything would have lasted much much longer. Thank you Matthias, Mathias, Robert, Rolf and Marco. Thank you Armin, Olaf and Annett for all the work on designing

the experimental vacuum chamber.
I thank the League for all the love, peace and happiness they provided. Special thanks to Thomas for his dedication.
Sometimes I almost forget about the entire IT-structure, which is a sign that it works well. Jens, Daniela and Paul, thank you for this.
Special thanks go to Petra, Katrin and Anne, who are able to make things just happen. I cannot even imaging all the things they probably have handled in the background without me even realising it.
Many more colleagues have supported me in the process of completing this project. Not only professionally, but also socially. I have been lucky to work in such a wonderful department with so many nice people. I had many interesting discussions, had fun and learned a lot, not only at but also outside of work. To all my colleagues: thank you for this.

I had the honour to be part of what I like to think of the most awesome Marie Skłodowska Curie initial training network ever. Thank you Carsten for making LA^{3}NET happen. Thank you Rob, Magdalena and Alexandra for all the organisation, the training and all the wonderful experiences. Thanks go to all fellows from LA^{3}NET: Alexandra, Yelong, Thomas, Thomas, Irene, Matthieu, Andreas, Luca, Jakob, Kamil, Jose, Lara, Pengnan, Stanimir, Andrii, Cheng, Rui & Mateusz for being such an awesome group and widening my view of the world.

A PhD project is not something that one turns off when going home. What has kept me sane is all these friends who surround me that were there for me when I needed them support or a distraction.
Thanks to the Mysa group: Almut, Axel, Axel, Fabian, Melanie, Josefine, Raphael, Florian, Lotti, Andrea and Marco. All those evenings were the best, it is known.
Also many thanks to the cool people group: Ana, Martin, Jan, Manuel, Olga, Dmitry, Liya, Veit, Karla and Victor. Thank you for all the time we spend together.
There are moments where your life is about to be changed without you knowing it. This evening that I ran into this Canadian guy who insulted me and that friendly German guy was one of those. If this evening would not have happened my life would have been quite a lot more boring. Thank you Balkancrew for adopting this physicist. Thanks to Heiner, John, Nori, Tomáš, Pavla, Zuzu, Timea and Milan for all the good times.
Many thanks go to my family for all their support. I was lucky to have my brothers and their partners around in the last few years, to get through tough times together and to know that I will always have a home back home. Thank you Pier Herre, Jolanda, Ale & Nella. Also thanks to Otte Fien, Lieze Loor, Jip, Jidde Tijn, Doutze & Pepijn for being awesome nieces and nephews.
I also thank my soon to be family-in-law for accepting me so warmly into your family. You have made me feel at home right from the beginning. Thank you Emel teyze, Yücel amca and my baldiz; Pelin.
Finally and most of all I want to thank my soon to be wife, Rengin. Thank you for all your love, patience, support and understanding.

DECLARATIONS / ERKLÄRUNGEN

I herewith declare that I have produced this thesis without the prohibited assistance of third parties and without making use of aids other than those specified; notions taken over directly or indirectly from other sources have been identified as such. This paper has not previously been presented in identical or similar form to any other German or foreign examination board.
This dissertation has been prepared at the Helmholtz-Zentrum Dresden – Rossendorf at the Instiute for Radiation Physics under supervision of Dr. Arie Irman & Prof. Dr. Ulrich Schramm.
I hereby recognise the Doctoral regulations, Dresden University of Technology, Faculty of Mathematics and Natural Sciences dated 23rd February 2011, last amended 18th June 2014.

Hiermit versichere ich, dass ich die vorliegende Arbeit ohne unzulässige Hilfe Dritter und ohne Benutzung anderer als der angegebenen Hilfsmittel angefertigt habe; die aus fremden Quellen direkt oder indirekt übernommenen Gedanken sind als solche kenntlich gemacht. Die Arbeit wurde bisher weder im Inland noch im Ausland in gleicher oder ähnlicher Form einer anderen Prüfungsbehörde vorgelegt.
Die Dissertation wurde am Helmholtz-Zentrum Dresden – Rossendorf im Institut für Strahlenphysik angefertigt unter Betreuung von Dr. Arie Irman & Prof. Dr. Ulrich Schramm.
Der Promotionsordnung, Technische Universität Dresden, Fakultät Mathematik und Naturwissenschaften vom 23.02.2011 mit letzten Änderungen vom 18.06.2014 erkenne ich an.

Dresden, .03.2018

Jurjen Pieter Couperus

HZDR
HELMHOLTZ
ZENTRUM DRESDEN
ROSSENDORF

Bautzner Landstr. 400
01328 Dresden, Germany
Tel. +49 351 260-3005
Fax +49 351 260-13005
j.couperus@hzdr.de
http://www.hzdr.de